

Opinion

To Shell Model, or Not to Shell Model, That Is the Question

Andrew E. Stuchbery^{1,*}  and John L. Wood²

¹ Department of Nuclear Physics and Accelerator Applications, Research School of Physics, The Australian National University, Canberra, ACT 2600, Australia

² School of Physics, Georgia Institute of Technology, Atlanta, GA 30332, USA; john.wood@physics.gatech.edu

* Correspondence: andrew.stuchbery@anu.edu.au

Abstract: The present review takes steps from the domain of the shell model into open shell nuclei. The question posed in the title is to dramatize how far shell model approaches, i.e., many nucleons occupying independent-particle configurations and interacting through two-body forces (a configuration interaction problem) can provide a description of nuclei as one explores the structure observed where neither proton nor neutron numbers match closed shells. Features of doubly closed and singly closed shell nuclei and adjacent nuclei are sketched, together with the roles played by seniority, shape coexistence, triaxial shapes and particle–core coupling in organizing data. An illuminating step is taken here to provide a detailed study the reduced transition rates, $B(E2; 2_1^+ \rightarrow 0_1^+)$, in the singly closed shell nuclei with doubly closed shell plus or minus a pair of identical nucleons, and the confrontation between such data and state-of-the-art shell model calculations: this amounts to a review of the effective charge problem. The results raise many questions and point to the need for much further work. Some guidance on criteria for sharpening the division between the domain of the shell model and that of deformation-based descriptions of nuclei are provided. The paper is closed with a sketch of a promising direction in terms of the algebraic structure embodied in the symplectic shell model.

Keywords: nuclear structure; shell model; seniority; shape coexistence; effective charge; emergent structure



Citation: Stuchbery, A.E.; Wood, J.L. To Shell Model, or Not to Shell Model, That Is the Question. *Physics* **2022**, *4*, 697–773. <https://doi.org/10.3390/physics4030048>

Received: 30 November 2021

Accepted: 8 March 2022

Published: 29 June 2022

Publisher's Note: MDPI stays neutral with regard to jurisdictional claims in published maps and institutional affiliations.



Copyright: © 2022 by the authors. Licensee MDPI, Basel, Switzerland. This article is an open access article distributed under the terms and conditions of the Creative Commons Attribution (CC BY) license (<https://creativecommons.org/licenses/by/4.0/>).

1. Introduction

The shell model has served as the most fundamental view one possesses when looking at the structure of nuclei. With its inception, at the hands of Maria Goeppert-Mayer [1] and Hans Jensen and colleagues [2] in 1949, at “three-score years and ten”, it is not going to die. It is based on the premise of independent-particle motion in a spherical mean field with strong spin–orbit coupling. The quantum mechanical solution, at the level of independent-particle motion in a harmonic-oscillator potential, can be obtained using methods that all senior-year undergraduate students should be able to handle. It provides a far-reaching language for talking about nuclear structure. With the “gift” of the harmonic oscillator potential to the mathematics of quantum physics, the symmetries that emerge are without equal in the quantum domain. Thus, why question “shell model” in its verbal (i.e., operative) form?

The problem is correlations. Correlations are the antithesis of independent-particle motion in quantum many-body systems. The problem in nuclei is: Just how deeply do correlations influence what we are studying? A shell modeler must start by assuming a correlation-free basis: a complete set of states, which are many copies of single-particle states each labelled by a principal quantum number (N), an angular momentum quantum number (l), a directional component of angular momentum (m_l), and spin plus direction-of-spin quantum numbers (s, m_s). (Spin–orbit coupling favors a j -coupled basis, $|N, j, l, m_j\rangle$, where j and m_j are the total angular momentum and its projection.) However, pairing correlations immediately dominate singly closed-shell nuclei; and most nuclei are deformed

in their ground states while many that have spherical ground states exhibit low-energy deformed states. A simple extension of the shell model philosophy to a deformed mean field, the Nilsson model, augmented with adiabatic rotational degrees of freedom, provides an enormously powerful organizing principle for handling large amounts of data, in the guise of the unified or Bohr–Mottelson model. However, a very large number of nuclei do not separate into this simple adiabatic factorization. Such nuclei are often called “transitional nuclei”. Herein lies the biggest challenge that remains in order to achieve a unified view of nuclear structure. Transitional nuclei are “sandwiched” between the shell model [3] and the unified model [4], and correlations are dominant. How do we develop theories applicable to such nuclei? To shell model or not to shell model?

The use of the term “to shell model” here is in reference to the time-honoured theoretical approach to nuclear structure which uses a basis of spherical independent-particle states, truncated at a small number of shell model energy shells, and a residual two-body interaction. The shell model is therefore a configuration interaction problem. The question then is which correlations are important, and how can one ensure that the relevant correlations emerge in the calculations.

The shell model approach is straightforward for handling all nuclei: start by introducing two-body interactions. Indeed, at the level of pairing interactions, this leads to the quasispin and seniority concepts. Quasispin is a formulation that manifestly illustrates what is meant by correlations in a quantum mechanical many-body system. With a simple approximation (by use of quasispin coherent states) this leads to the Bardeen–Cooper–Schrieffer (BCS) theory of superconductivity (see Section 4.5.3 in [5]). In finite many-body systems, as applied to nuclei, the language only needs some simple constraints to accommodate shell structure. Seniority, and its implied quasispin structure, dominates excitation patterns in singly closed shell nuclei. However, seniority breaks down immediately, at low spin, when both protons and neutrons are active. This is again due to correlations, but these correlations are not yet well understood: this is the point where nuclear deformation emerges. This nexus is the focus of the present review.

The shell model provides the most fundamental language one possesses for discussion of nuclear structure. This conceptual basis is often called the “shell model”. Here, as defined, the term “shell model” is adopted in its more restricted usage as a computational model, where a Hamiltonian defined by residual interactions is diagonalized in a spherical independent-particle basis. Our view is that, with sufficient computing power, a suitable basis, and appropriate interactions, all structural details of nuclei would likely emerge. The issue, apart from the magnitude and complexity of the problem, is whether the structures in the output would be evident and intelligible. Here, the task of discussing the emergent structures in nuclei and the use of algebraic models to understand them is adopted in the context of the nuclear shell model. Therefore, the experimental data are broadly reviewed and the cases where simple models based on phenomenology and algebraic models give insights that would not be evident in a complex large-scale shell model approach are highlighted.

2. Nuclei with Closed Shells: An Experimental Perspective

Nuclei with closed shells, both singly and doubly closed, have been the base upon which the shell model has been built. However, such nuclei are neither manifestations of nor a sound basis for the shell model in its extreme independent-particle form. Such nuclei (i.e., closed shell) can usefully be classified into three types: doubly closed shell nuclei with equal numbers of protons (Z) and neutrons (N), i.e., $N = Z$; doubly closed shell nuclei with $N > Z$; and singly closed shell nuclei.

The distinction of doubly closed shell nuclei with $N = Z$ is that they exhibit shape coexistence at low energy, even at the level of the first excited states in ^{16}O and ^{40}Ca , as shown in Figure 1. In doubly even nuclei with $N > Z$, shown in Figure 2, shape coexistence has not yet been observed. The simple explanation is that, for $N = Z$, spatial overlap of the

proton and neutron configurations is maximal, and it is proton–neutron correlations that are deformation producing.

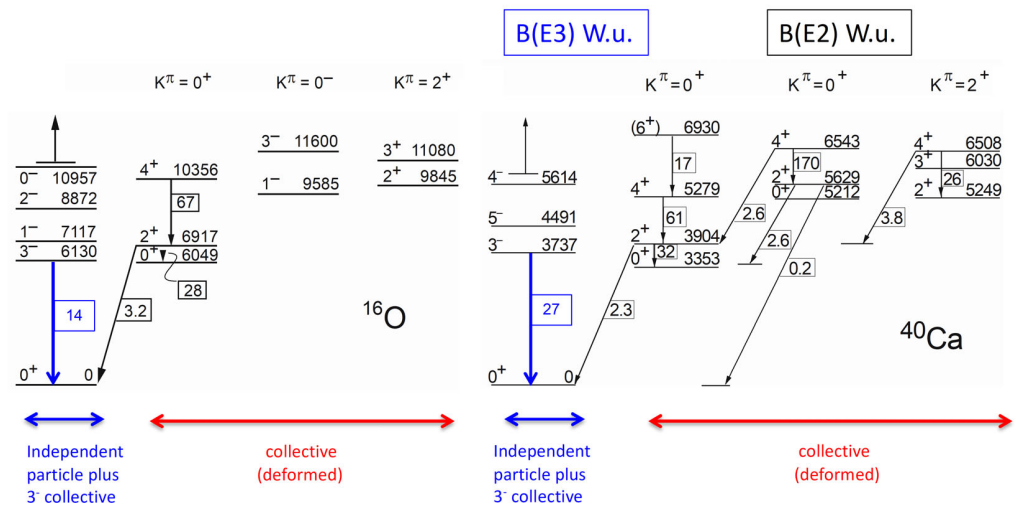


Figure 1. Excited states in the $N = Z$ doubly closed shell nuclei ^{16}O and ^{40}Ca . Collectivity associated with the 2_1^+ and 3_1^- states is shown. Collectivity involving deformation is supported by large electric-quadrupole transition rates, as indicated by the $B(E2)$ values in Weisskopf units (W.u.). Inferred K quantum numbers for collective bands are indicated. The horizontal bars with upward pointing arrows indicate excitation energies above which states are omitted. Adapted from [6].

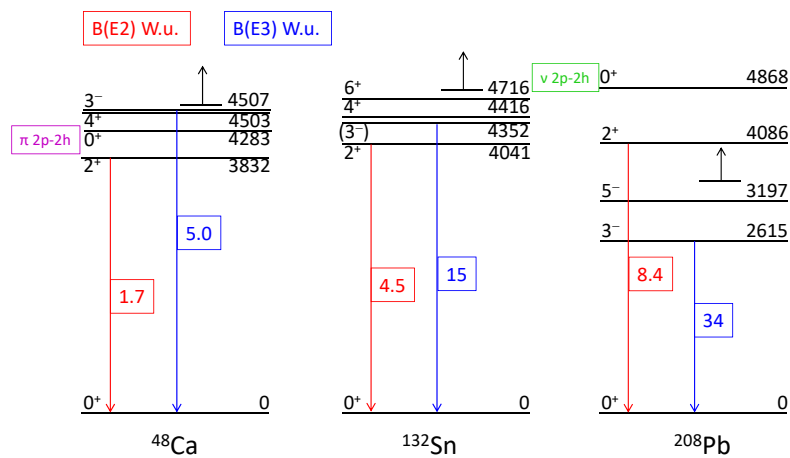


Figure 2. Excited states in the $N > Z$ doubly closed shell nuclei. Collectivity associated with the 2_1^+ and 3_1^- states is indicated by $B(E\lambda)$ values. The lowest known pair excitations are labelled. The horizontal bars with upward pointing arrows indicate excitation energies above which states are omitted. Electromagnetic decay strengths for ^{132}Sn are calculated from data appearing in [7]. Adapted from [8].

The distinction of singly closed shell nuclei is that they are dominated by the emergence of pairing correlations. Pairing correlations are concisely formulated using the concept of the seniority quantum number, v , i.e., the number of unpaired nucleons. This was first recognized by Maria Goeppert-Mayer [9,10]. The quantum mechanics of pairing correlations is concisely, even elegantly, described using quasispin, as introduced by Arthur Kerman [11]. The basic features of quasispin, as applied to a series of $(j = 7/2)^n$ configurations, where n denotes the occupation of the orbit, are shown in Figure 3; a view which complements that in Figure 3 is shown for a series of $(j = 9/2)^n$ configurations in Figure 4. The quasispin algebra is developed in detail in Chapter 6 of [6]. That Chapter includes a thorough treatment of the origins of the key ideas from Racah’s seniority [12–14] through

Flowers' handling of $j - j$ coupling [15], Helmers' unitary symplectic invariants [16], Lawson and Macfarlane's identification of the rank-1/2 quasispin $su(2)$ tensorial character of one-body annihilation and creation operators [17], to Kerman's simple formulation [11]. Furthermore, it can be noted that there is a profound duality structure residing in these algebras [18], which shows how algebraic structure provides insight into the complexity of many-body quantum systems. A pedagogical treatment of the quasispin algebra is presented in Chapter 4 in [5]. That Chapter illustrates how P.W. Anderson's idea [19] provided the first conceptual recognition of quasispin as the essential algebraic structure underlying many-fermion systems with Cooper pairs [20].

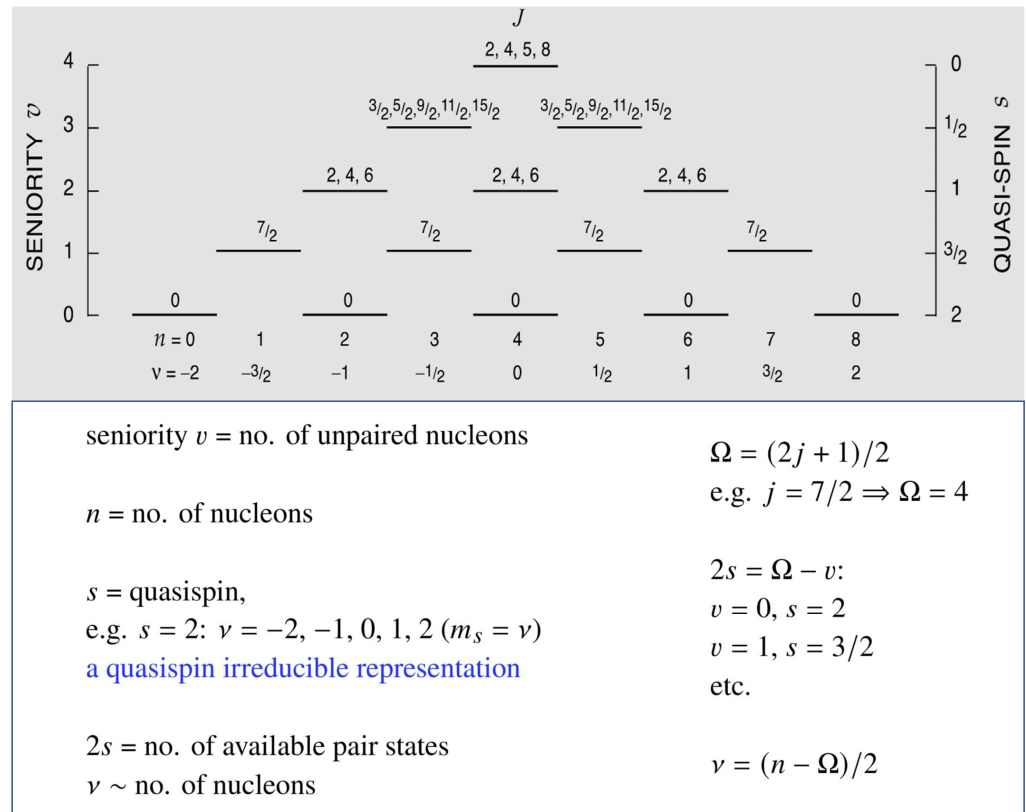


Figure 3. A schematic view of basic features possessed by a seniority-dominated $j = 7/2$ shell with a many-proton or many-neutron structure. The excitation patterns and associated spins are shown relative to the seniority zero, $v = 0$ states across the filling of the shell, where the filling is designated by the particle number, n . The quasispin quantum numbers, s and v are $su(2)$ quantum numbers and their relationship to shell model quantum numbers is shown in the box. Adapted from [6].

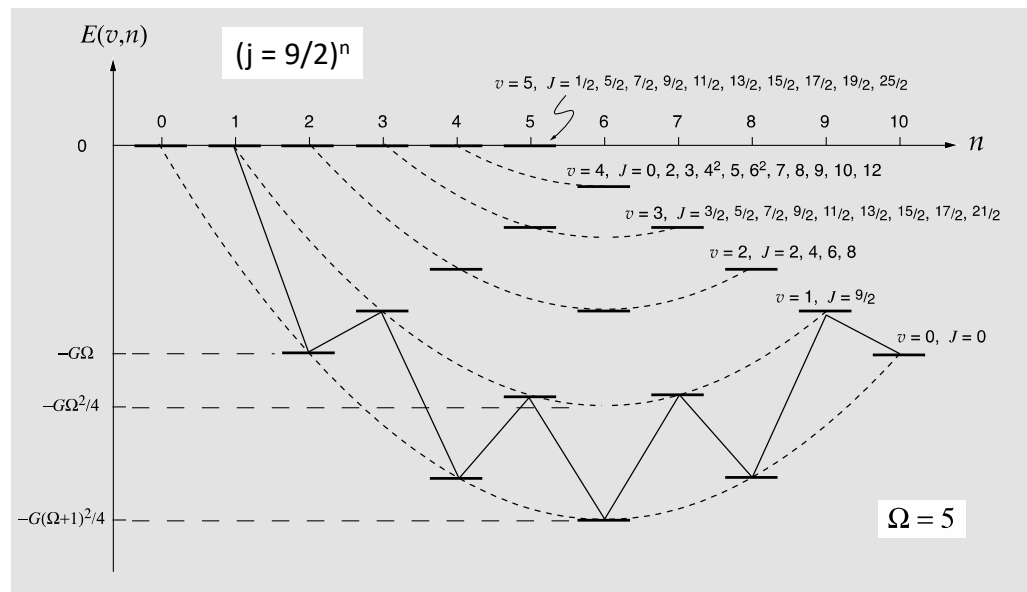


Figure 4. A schematic view of basic features of a seniority-dominated $j = 9/2$ shell. The excitation patterns and associated spins J are shown relative to the uncorrelated, $v = \max.$ states across the filling of the shell, where the filling is designated by the particle number, n . For other details, see Figure 3. Taken from [6].

Experimentally, the seniority coupling scheme is realized essentially exactly when the low-energy structure of singly closed shell nuclei is dominated by a high- j orbital. This is shown in Figure 5 for $j = 11/2$ neutron subshell filling in the Sn isotopes and in Figure 6 for $j = 11/2$ proton subshell filling in the $N = 82$ isotones. The patterns are almost indistinguishable. The domination of seniority extends into patterns of electric quadrupole, $E2$ transition probabilities: this is shown in Figure 7 for $j = 9/2$ configurations in even-Cd and even-Pd nuclei with $N = 50$ and $N = 82$. The pattern of $E2$ matrix elements in nuclei dominated by seniority coupling shows a smoothly changing character which is well described by the following relationship for the reduced transition strength [6]:

$$B(E2; svJ_i \rightarrow svJ_f) \propto \langle sv10|sv \rangle^2 = \frac{\nu^2}{s(s+1)} = \frac{(n - \Omega)^2}{4s(s+1)}, \tag{1}$$

where J_i and J_f are spins of initial and final states, s, ν are quasispin quantum numbers, details of which appear in Figure 3; $\langle sv10|sv \rangle$ is an $su(2)$ Clebsch–Gordan coefficient and $\Omega = (2j + 1)/2$, e.g., $\Omega = 6$ for $j = 11/2$. This Clebsch–Gordan coefficient emerges from the quasispin $su(2)$ algebra when applying the Wigner–Eckart theorem to the $E2$ operator: this operator is a rank-1 quasispin tensor. Details are beyond the present discussion and are given in [6]. (Note: ν (designated by the Greek letter nu) is distinct from the seniority quantum number, v (designated by the Latin letter vee).) This relationship is illustrated in Figures 8 and 9 for the $j = 11/2$ configurations in the even-mass Sn isotopes and $N = 82$ isotones, respectively. Indeed, these patterns are one of the best signatures of structure unique to singly closed shell nuclei. However, the clarity and interpretation of these structures are dictated by quantum mechanics that is beyond that of the independent-particle shell model in that correlations in the form of Cooper pairs have emerged. Pairing Hamiltonians can be derived as a simplification of the nucleon–nucleon residual interaction; however, the focus here is on the empirical simplicity of the seniority structures that persist toward mid-shell where the number of valence nucleons is large, in contrast with the connection between pairing correlations and the two-body residual interactions in a large-basis shell model calculation, which is not obvious. Stated in rhetorical terms: Could one ascertain the algebraic structure of Cooper pairs, in the guise of quasispin, and manifestly controlling structure in all singly closed shell nuclei, based on a shell model computational

program? Once the quasispin structure is recognized, its implications for the residual interactions required in the shell model can be explored so that the structure emerges from the calculations.

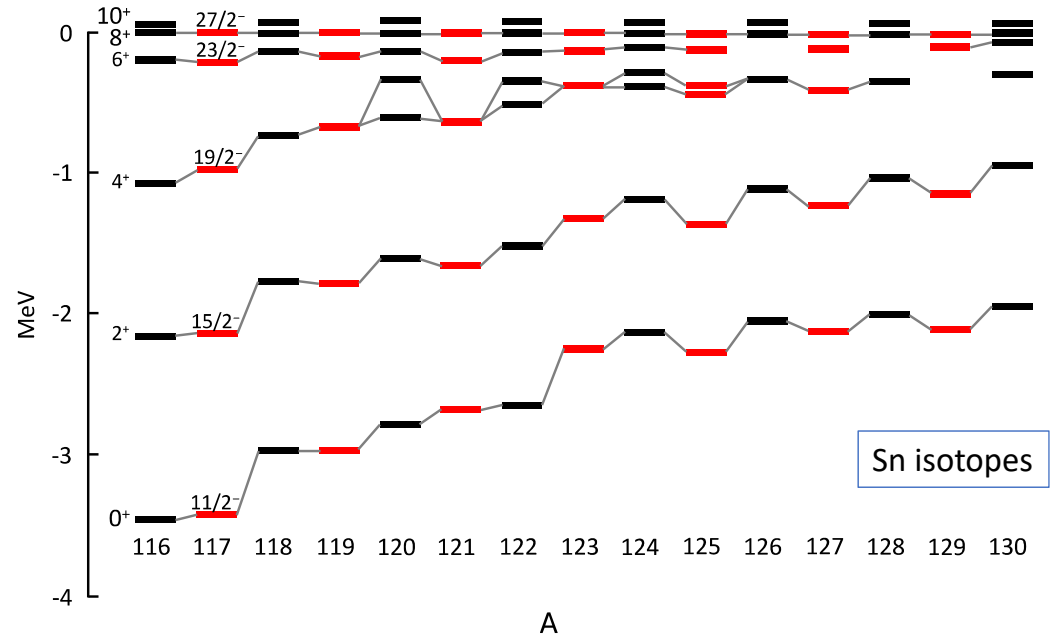


Figure 5. The seniority-dominated spectra versus the atomic mass number, A , in the neutron-rich tin isotopes, shown relative to the highest spin state in each multiplet (note the $J = 27/2$ state in the odd-mass isotopes is set at the same level as the $J = 8$ state in the even mass isotopes). These structures are dominated by neutrons filling the $1h_{11/2}$ orbital. Note: multiple $J = 4$ states are seen in $^{120,122,124}\text{Sn}$ and multiple $J = 19/2$ states are seen in ^{125}Sn . Reproduced from [8].

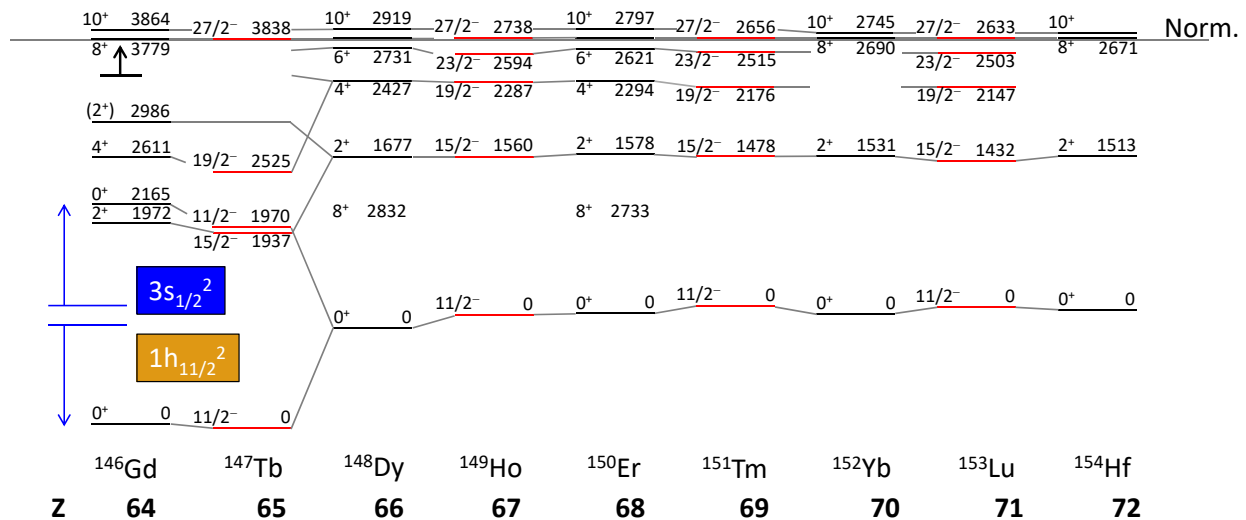


Figure 6. The seniority-dominated spectrum in the proton-rich $N = 82$ isotones, shown relative to the highest spin state in each multiplet (note the $J = 27/2$ state in the odd-mass isotones is set at the same level as the $J = 8$ state in the even-mass isotones). These structures are dominated by protons filling the $1h_{11/2}$ orbital. The structure of ^{146}Gd and ^{147}Tb involves two-state mixing, as depicted schematically. Reproduced from [8].

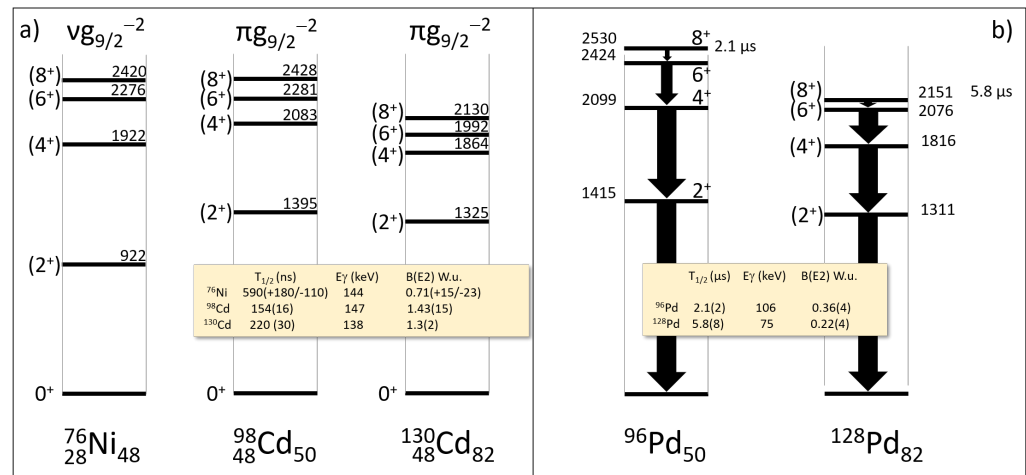


Figure 7. (a) Seniority isomers involving $j = 9/2$ structures. The inset shows the half lives of the states with spin 8, the corresponding $8^+ \rightarrow 6^+$ transition energies, and the deduced $B(E2)$ values for these transitions. The constancy of the $B(E2)$ values, independent of mass, is remarkable and shows the simple nature of seniority structures. The figure is adapted from one appearing in [21]. Data are from the Evaluated Nuclear Structure Data File (ENSDF) [22]. The 6^+ -state energy in ^{130}Cd , which is uncertain in ENSDF, is from [23]. (b) Seniority isomers involving the proton $(1g_{9/2})^{-4}$ configurations in the palladium isotopes at the $N = 50$ and $N = 82$ shell closures. The inset shows the deduced $B(E2)$ values. The ^{96}Pd scheme is adapted from one appearing in [24] and the ^{128}Pd scheme is from [25]. The tabulated half lives and $B(E2)$ values are taken from ENSDF. There are more recent published values [26,27], but the conclusions do not change.

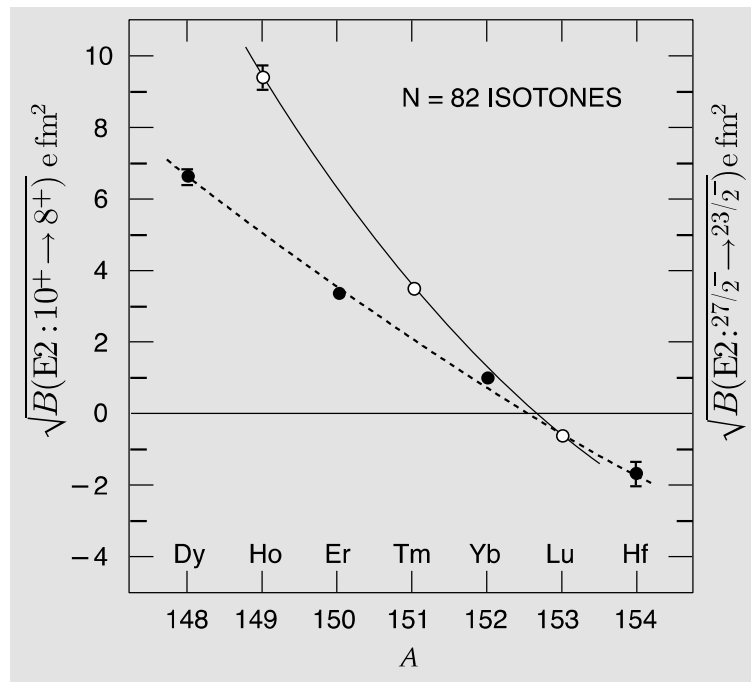


Figure 8. Illustration of Equation (1), expressed in square-root form, for the proton $1h_{11/2}$ configurations in the $N = 82$ isotones. The $B(E2)$ data shown are for the $10^+ \rightarrow 8^+$ transitions in the even-mass nuclei and for the $27/2^- \rightarrow 23/2^-$ transitions in the odd-mass nuclei, cf. Figure 6. The sign of the square root is allowed to change to match the matrix element changing from positive to negative as depicted. If the proton number is counted with reference to ^{146}Gd as $n = 0$: with $\Omega = 6$, according to Equation (1), the $B(E2)$ value should vanish at ^{152}Yb . Note that this is an effect emerging from the Wigner–Eckart theorem for $su(2)$, applied to reduction of the $E2$ matrix elements with respect to their quasispin tensor structure. Redrawn from [28].

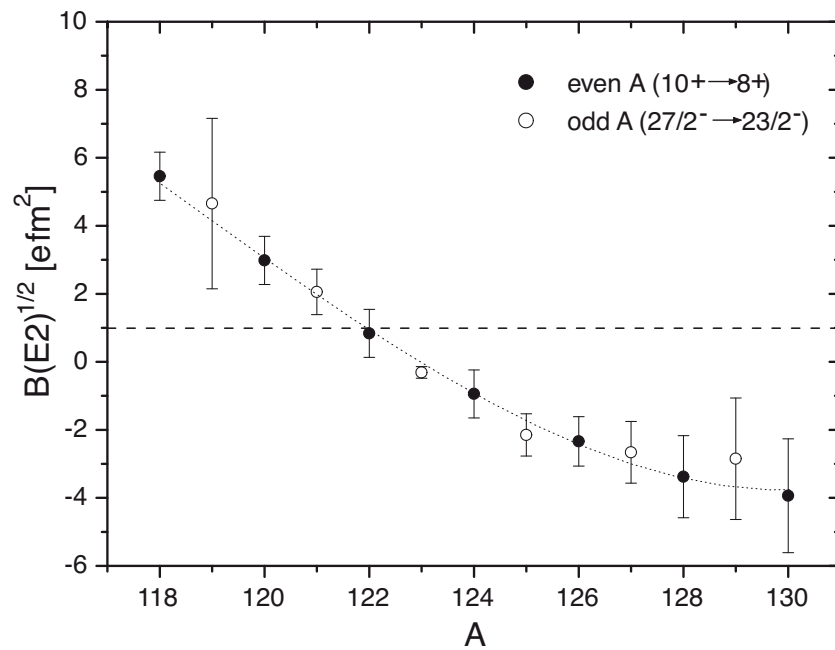


Figure 9. A pattern of $B(E2)$ values, similar to that shown in Figure 8, for the even-mass and odd-mass Sn isotopes. These data suggest that the half-filled shell, where the $B(E2)$ value goes to zero, is at $A \sim 122$, i.e., that the $1h_{11/2}$ orbital is not at the highest energy within the $50 < N < 82$ shell: this is consistent with ^{129}Sn (and likely ^{131}Sn) exhibiting a ground-state spin–parity of $3/2^+$. Note: there is a scale factor of 0.514 applied between the even and odd-mass values, which accommodates the $v = 2$ and $v = 3$ seniorities involved via the Clebsch–Gordan coefficient in Equation (1). Reprinted with permission from [29]. Copyright (2008) by the American Physical Society.

In the remainder of this Section, some observations are made with respect to the mathematical structure on which quasispin is based, in order to place this shell model view into perspective.

The arrival at the concept of quasispin as a degree of freedom in nuclei requires the recognition of mathematical structures that are not obvious. A brief sketch of the essential details is given here in words. Full details are given by Rowe and Wood [6] and, at an introductory level, by Heyde and Wood [5]. Specifically, the quasispin algebra is recognized by expressing the Hamiltonian and the interaction using second quantization. The mathematics emerge by taking bilinear combinations of the elements (one-body fermionic creation and annihilation operators) of a Jordan algebra (anticommutator brackets of the creation and annihilation operators). These bilinear combinations obey a Lie algebra (commutator brackets). This is impossible to see until one works out the Lie bracket values of the bilinear combinations, which is done by expanding them using anticommutator bracket relations so as to express everything in terms of Jordan algebra elements in “normal order”; see Equation (4.93) in Ref. [5]. Normal order means annihilation operators all to the right and creation operators all to the left. Furthermore, the Lie bracket algebra for a Jordan algebra element (single creation or annihilation operator) with quasispin algebra elements (bilinear combinations of creation and annihilation operators) reveals that the creation and annihilation operators are rank-1/2 quasispin tensors. This is also impossible to see until one works out the Lie bracket values. Indeed, rank-1/2 tensors are unknown in spin-angular momentum theory; see p. 423 in Ref. [6] for additional details.

Spectroscopy of low-spin and medium-spin states is beginning to provide a comprehensive (near-complete) view of excited states in doubly even nuclei at and near closed shells. Consequently, seniority coupling has been shown to apply in nuclei where the structure is dominated by two medium-spin j shells. This is illustrated in Figures 10 and 11 for the $N = 82$ isotones with $Z < 64$. The $v = 2$ structures in ^{134}Te , ^{136}Xe , ^{138}Ba , and ^{140}Ce are labelled in Figure 10: these include the $1g_{7/2}$ structures, with $J = 2, 4,$ and $6,$ and

the $1g_{7/2}-2d_{5/2}$ structures, with $J = 1, 2, 3, 4, 5,$ and 6 . In ^{136}Xe only, as expected, $v = 4$ structures are observed with the allowed spins, $J = 2, 4, 5,$ and 8 , cf. Figure 3. The comprehensive view of ^{136}Xe is the result of an $(n, n'\gamma)$ study [30]. Note that this seniority-based organization of data is essentially complete; for example, there is no excited $7/2^+$ state observed, as might be expected from a $1g_{7/2} \otimes 2_1^+$ coupling—such a coupling is forbidden by the Pauli exclusion principle if the 2_1^+ states are seniority-dominated structures. The $B(E2; 2_1^+ \rightarrow 0_1^+) = B_{20}$ values and the magnetic moments, $\mu(2_1^+)$, are shown for reference and discussed further in Figure 12 as the g factors, where $g(2_1^+) = \mu(2_1^+)/2$.

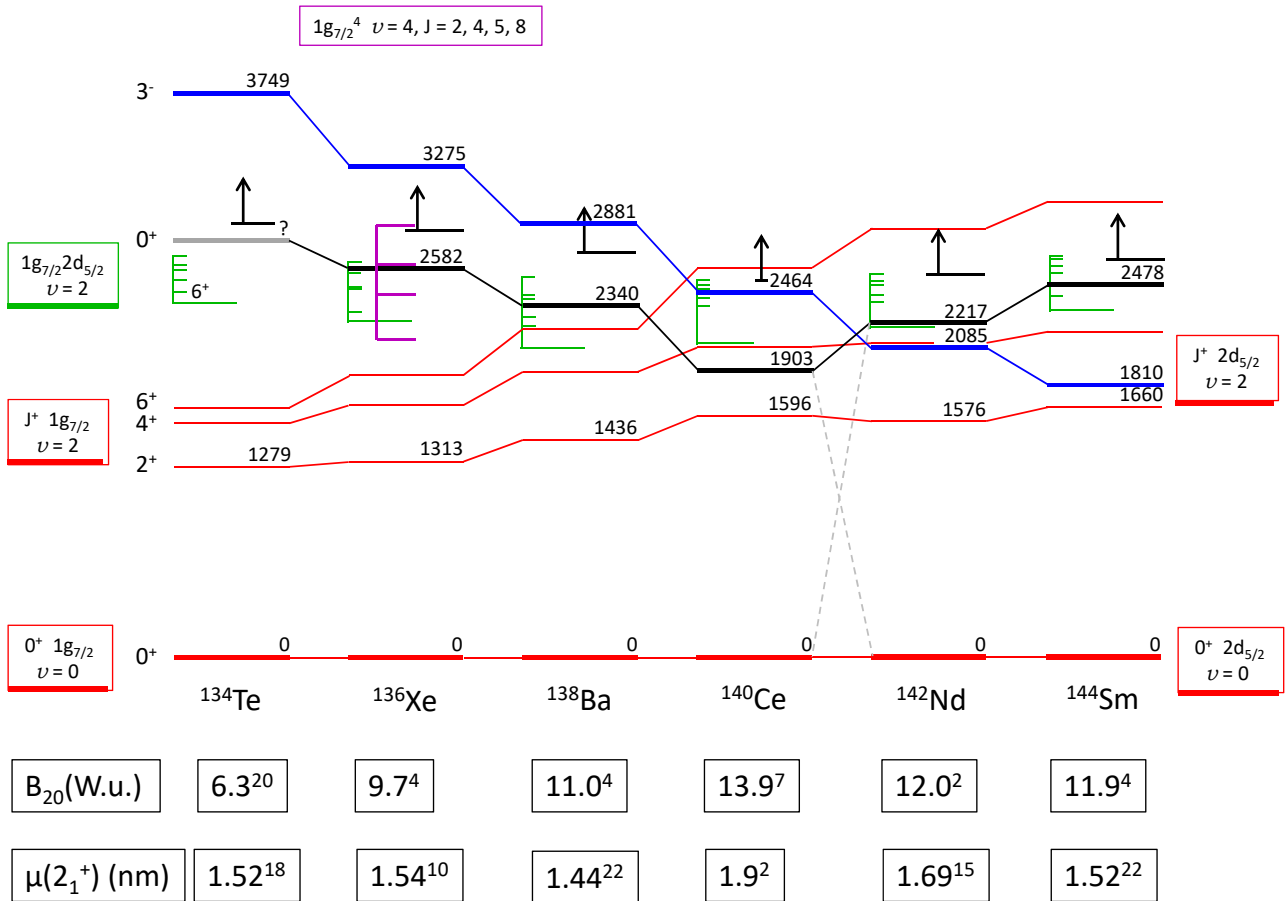


Figure 10. A view of the systematics of the even-mass $N = 82$ isotones with $50 < Z < 64$. The low-energy structure of these isotones is dominated by occupancy of the $\pi 1g_{7/2}$ and $\pi 2d_{5/2}$ shell model configurations: the Fermi surface progressing from the $\pi 1g_{7/2}$ to the $\pi 2d_{5/2}$ orbit is schematically indicated by dashed lines between ^{140}Ce and ^{142}Nd . The seniority structures are identified. The 3^- states are shown for reference. Horizontal bars with vertical arrows indicate excitations above which states are omitted from the figure.

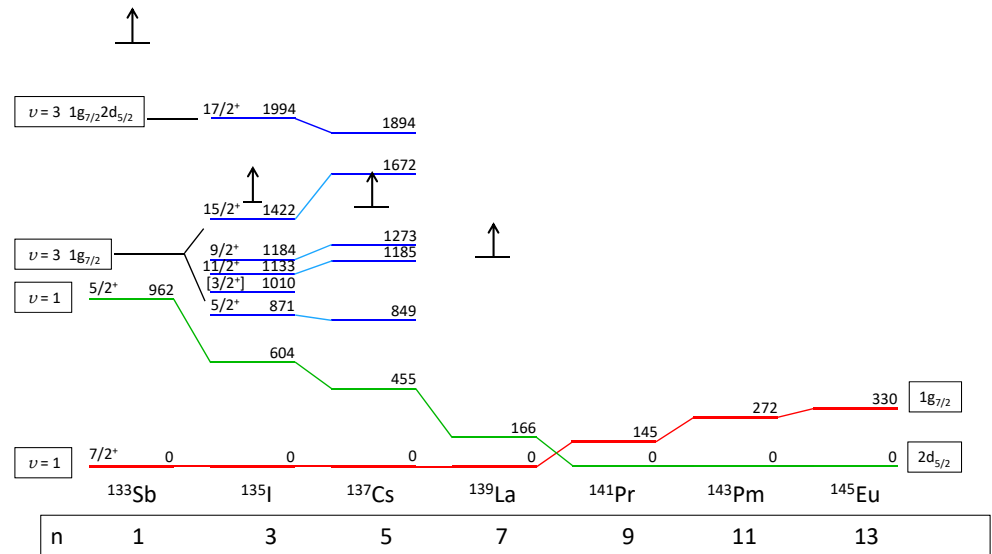


Figure 11. A view of the systematics of the odd-mass $N = 82$ isotones with $50 < Z < 64$. The low-energy structure of these isotones, as noted in Figure 10, is dominated by occupancy of the $1g_{7/2}$ and $2d_{5/2}$ shell model configurations: here, the completion of the filling of the $1g_{7/2}$ orbital at $Z = 58$ (^{140}Ce) is manifest in the change in ground-state spins between ^{139}La and ^{141}Pr . In ^{135}I and ^{137}Cs only, as expected, $v = 3$ structures are observed with the allowed spins, $J = 3/2, 5/2, 9/2, 11/2$, and $15/2$, cf. Figure 3. Note: the spin of 1010 keV state in ^{135}I is not known but is consistent with $3/2^+$. A state with spin-parity $3/2^+$ is predicted at about 1 MeV excitation energy in ^{137}Cs . Horizontal bars with vertical arrows indicate excitations above which states are omitted from the figure. Additional data for ^{141}Pr , ^{143}Pm , and ^{145}Eu are not shown because they are not part of the present focus. Taken from [8].

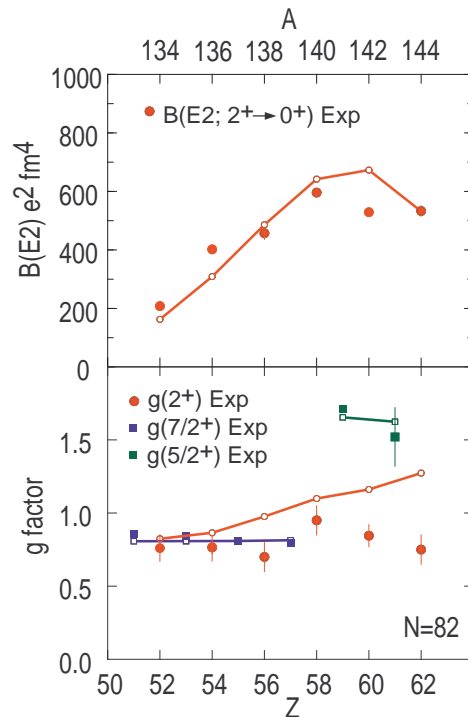


Figure 12. Shell model calculations of $B(E2)$ and g factors in the $N = 82$ isotones with $50 < Z < 64$. Reproduced from [31], with the permission of AIP Publishing.

The seniority structure of the $N = 82$ isotones and its breakdown is an issue for future detailed study. However, shell model calculations affirm the dominant seniority structures. The case of ^{136}Xe has been studied comprehensively [30,32]. Table 1 shows experimental $B(E2)$ values between low-excitation states in ^{136}Xe in comparison to the $(1g_{7/2}2d_{5/2})$ seniority model, as well as several shell model calculations that include all orbits in the $50 \leq Z \leq 82$ major shell but use alternative interactions. The $B(E2)$ data indeed demonstrate the pattern predicted by the seniority scheme. It should be noted that ^{136}Xe represents the mid-shell for the $\pi 1g_{7/2}$ orbit, for which several $E2$ transitions are forbidden. In such cases, the observed transition strengths result from small components of the wavefunction, which can lead to considerable variations in the shell model predictions, despite the calculations agreeing on the dominant structure of the states. It was noted in [32] that the large-basis shell model calculations support the dominant configurations assigned in the $(1g_{7/2}2d_{5/2})$ seniority model up to the 4_2^+ state at 2.1 MeV excitation, although there is considerable configuration mixing. The $(1g_{7/2}2d_{5/2})$ model accounts for all states up to about 2.8 MeV, with the exception of the 0_2^+ state (more on the 0_2^+ state below in this Section). However, above the 2.1-MeV 4_2^+ state, where the level of density increases, the correspondence between the two-level and full basis is less clear.

The 0_2^+ states are consistent with a multi-pair structure distributed over the $1g_{7/2}$ and $2d_{5/2}$ orbitals. For example, the $jj55$ model with $sn100$ interactions [33] has dominant configurations of $\pi(2d_{5/2})^2$ (76%) [^{134}Te], $\pi(1g_{7/2})^2(2d_{5/2})^2$ (45%) [^{136}Xe], and $\pi(1g_{7/2})^6$ (51%) [^{138}Ba], for the 0_2^+ states.

Table 1. Electric quadrupole transition rates in ^{136}Xe . The seniority model in the $(1g_{7/2}2d_{5/2})$ space is described in [30] and in the text. The shell model calculations from [30,32,34] use alternative interactions in the model space $1g_{7/2}, 2d_{5/2}, 3s_{1/2}, 2d_{3/2}, 1h_{11/2}$, which covers the $50 \leq Z \leq 82$ major shell.

Transition	$B(E2)$ ($e^2\text{fm}^4$)				
	Exp. [30,35]	Seniority	Ref. [34]	N82K [30]	jj55 [32]
$2_1^+ \rightarrow 0_1^+$	415(12)	415 ^(a)	357	400	398
$4_1^+ \rightarrow 2_1^+$	53.2(7)	0	63.6	86	48
$6_1^+ \rightarrow 4_1^+$	0.55(2)	0	0.088	0.12	4.8
$2_2^+ \rightarrow 0_1^+$	23(3)	0	—	12	0.7 ^(b)
$2_3^+ \rightarrow 0_1^+$	38(3)	22.2	—	12	48 ^(b)
$2_2^+ \rightarrow 2_1^+$	299(71)	419	—	103	308 ^(b)
$2_3^+ \rightarrow 2_1^+$	21 ⁺⁵⁸ ₋₂₁	0.63	—	117	8 ^(b)

^(a) The seniority model uses proton effective charge $e_p = 1.81$, set to reproduce the experimental $B(E2; 2_1^+ \rightarrow 0_1^+)$.

^(b) The calculated 2_2^+ state is identified with the experimental 2_3^+ state and vice versa.

Figure 12 shows the experimental g factors of the 2^+ states and the $B(E2; 2_1^+ \rightarrow 0_1^+)$ values of the even-even $N = 82$ isotones with $50 < Z < 64$, and compares them with large-basis shell model calculations. In addition, the ground-state g factors of the interleaving odd- A isotones are shown, which indicate that the Fermi surface moves from the $1g_{7/2}$ orbit into the $2d_{5/2}$ orbit at $Z = 59$. The $B(E2)$ trend is quite well described, but the $g(2_1^+)$ trend is not well described, particularly when the Fermi surface moves into the $2d_{5/2}$ orbit. In contrast, the odd- A isotopes are well described. Focusing on the range $51 \leq Z \leq 57$, the g factor data in Figure 12, for both odd and even- A isotones, are near constant and thus consistent with a simple $\pi 1g_{7/2}^n$ structure in both the ground states (odd- Z) and 2_1^+ states (even- Z). The lowered experimental $g(2_1^+)$ values for ^{140}Ce , ^{142}Nd and ^{144}Sm have been attributed to increasing contributions from $\nu(1h_{11/2}^{-1}2f_{7/2})$ excitations [36]. Nevertheless, the basic seniority structure appears to persist in these nuclei.

The complete pattern of excitations in odd-mass, singly closed shell nuclei is somewhat more complex than for even-mass singly closed shell nuclei. This is shown for $j = 11/2$ in

the tin isotopes in Figure 13. Note that the states expected for seniority $\nu = 3$ range over 14 spin values for $j = 11/2$, viz. $2J = 3, 5, 7, 9, 9, 11, 13, 15, 15, 17, 19, 21, 23$, and 27 (see, e.g., [37]). The experimental view is incomplete, but there is sufficient detail to conclude that the seniority scheme provides a reliable basis for understanding the low-energy excitations in these isotopes. This perspective is supported by a more global view of odd-mass nuclei shown in Figure 14, wherein patterns for seniority-three multiplets in selected nuclides and selected spin couplings are visible for $j = 7/2, 9/2$, and $11/2$. This global behavior appears not to have been recognized. We conjecture that there may be a geometric interpretation of this pattern, similar to the geometrical interpretation of two-body interactions for a pair of identical nucleons in a moderate to high j orbit, as introduced by Schiffer and True [38]. An angle between the two spins can be defined, which gives a measure of the overlap of the two orbits for different resultant spins; see discussions in Refs. [3,8].

One can conclude that seniority likely provides a complete description of the lowest-energy excited states in singly closed shell nuclei—with one proviso: singly closed shell nuclei exhibit low-energy deformed structures that “coexist” with the low-excitation seniority-dominated structures.

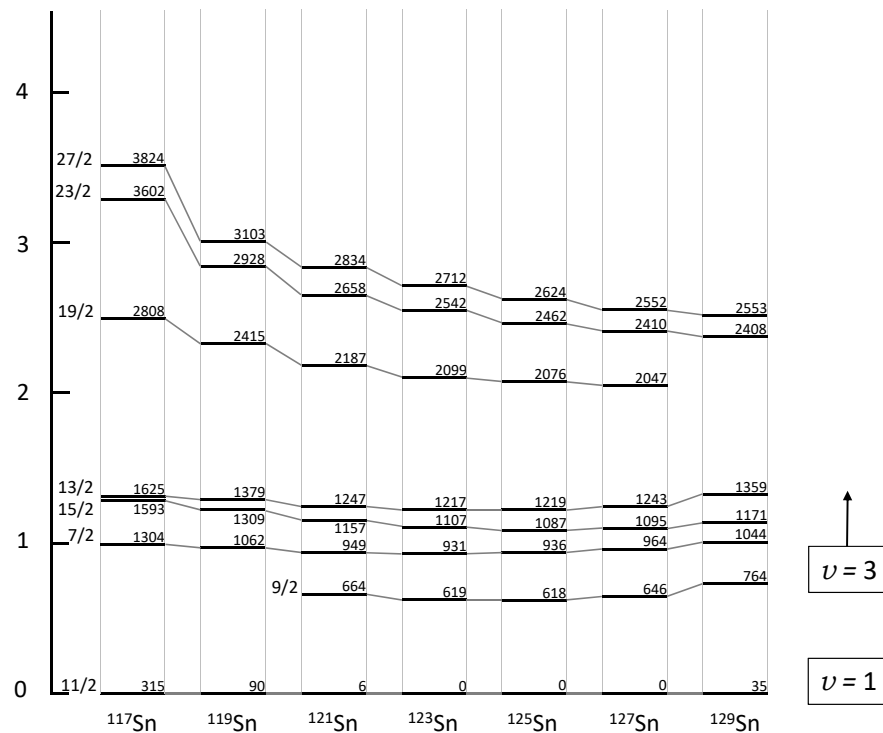


Figure 13. A view of the systematics of the seniority-three $\nu h_{11/2}^n$ states in the neutron-rich odd-mass tin isotopes. There are some states missing, according to seniority-dominated coupling; the full set contains: $2J = 3, 5, 7, 9, 9, 11, 13, 15, 15, 17, 19, 21, 23$, and 27 (see, e.g., [37]). Because of ambiguities in some parity assignments, other potential candidate states are omitted. Note there are “second” $19/2^-$ states observed in $^{123,125,127}\text{Sn}$.

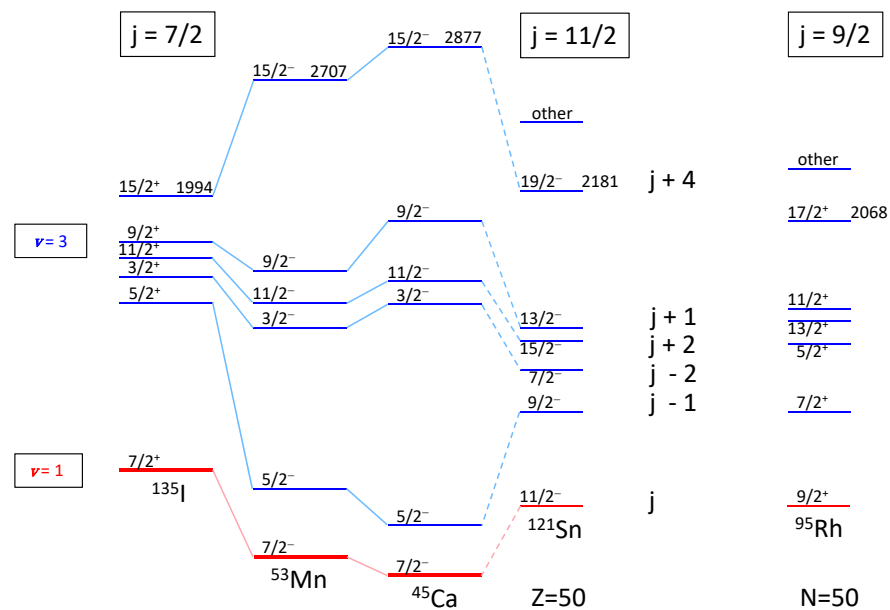


Figure 14. A global view of seniority-three multiplets in selected nuclides and selected spin couplings, for $j = 7/2, 9/2,$ and $11/2$. Energies are omitted to avoid cluttering the figure; energies are also relative, per isotope. To our knowledge, this universal behaviour has not been recognized. Note that the $j = 7/2$ multiplets (with the proviso made for ^{135}I in Figure 11) are complete; the $j = 9/2$ and $11/2$ multiplets contain more states than shown here, cf. Figures 4 and 13.

The manifestation of shape coexistence in singly closed shell nuclei was recognized already forty years ago [39] and was reviewed thirty years ago [40]. It is well established for $Z = 20, 50,$ and 82 and for $N = 20$ and 28 ; there are hints to its presence for $Z = 8$ and $28,$ and for $N = 8, 50,$ and 82 . Details can be found in the most recent review [41], together with some details in the earlier review [40]. The emerging view is that shape coexistence likely occurs in all nuclei; including that spherical states occur in nuclei with deformed ground states [42]. A concise perspective of the occurrence of deformation in nuclei as compared to atoms can be encapsulated in: “The difference between atoms and nuclei is that atoms are a manifestation of many-fermion quantum mechanics with one type of fermion, which repel, whereas nuclei involve two types of nucleon, which attract. By deforming, the system can lower its energy via relaxing the constraints of the Pauli exclusion principle in such a manner that more spatially symmetric configurations become accessible, which leads to a lowering of the energy of the system”. (It can be noted that the emerging view of baryons may signal correlated, even deformed structures, especially the recent realization [43] that the proton contains more (virtual) anti-down quarks than anti-up quarks: this is simply a manifestation of correlations that involve “particle–hole” excitations, i.e., quark–antiquark pairs, and the Pauli principle.)

3. Hints of Correlations, beyond Pairing and Seniority, at Closed Shells

The dominance of seniority, with intruding shape coexistence, in singly closed shell nuclei is not quite “the whole story”. The following analysis of effective charges implied by the observed $B(E2; 2_1^+ \rightarrow 0_1^+)$ in even-even nuclei adjacent to doubly closed shells demonstrates what can be encapsulated in the term “the effective charge problem”.

Electric multipole transition rates in the shell model are usually evaluated using harmonic oscillator wavefunctions. For a single-particle transition $j_\beta \rightarrow j_\alpha,$ the reduced matrix element $\langle j_\alpha || T(E2) || j_\beta \rangle$ can be evaluated from

$$\langle j_\alpha || T(E\lambda) || j_\beta \rangle = \frac{e}{\sqrt{4\pi}} (-1)^{j_\beta + \lambda - \frac{1}{2}} \frac{1 + (-1)^{l_\alpha + l_\beta + \lambda}}{2} \hat{\lambda} \hat{j}_\alpha \hat{j}_\beta \begin{pmatrix} j_\alpha & j_\beta & \lambda \\ \frac{1}{2} & -\frac{1}{2} & 0 \end{pmatrix} b^\lambda \tilde{R}_{\alpha\beta}^{(\lambda)}, \quad (2)$$

where $\hat{j} \equiv \sqrt{(2j+1)}$ and $\tilde{R}_{\alpha\beta}^{(\lambda)}$ is the dimensionless radial integral that can be evaluated in closed form with harmonic oscillator wavefunctions. The oscillator length b is defined as

$$b = \sqrt{\frac{\hbar}{m_N \omega}}, \tag{3}$$

where \hbar is the reduced Planck constant, m_N is the nucleon mass, and $\hbar\omega$ can be evaluated as a function of the mass number A as

$$\hbar\omega = (45A^{-1/3} - 25A^{-2/3}) \text{ MeV}, \tag{4}$$

which has been found to give satisfactory agreement with observed charge radii. In general,

$$B(E\lambda; J_i \rightarrow J_f) = |\langle J_f || T(E\lambda) || J_i \rangle|^2 / (2J_i + 1). \tag{5}$$

For transitions between the states of the pure j^2 configuration, the $B(E2)$ values are related to the single-particle matrix element $\langle j || T(E2) || j \rangle$, by

$$B(E2; J_i \rightarrow J_i - 2) = 4(2J_i - 3) \left\{ \begin{matrix} j & J_i - 2 & j \\ J_i & j & 2 \end{matrix} \right\}^2 |\langle j || T(E2) || j \rangle|^2. \tag{6}$$

It is instructive to begin with the textbook cases of ^{17}O and ^{18}O , which can be considered as adding one and two neutrons, respectively, to a ^{16}O core. Identifying the first-excited state to ground, $1/2_1^+ \rightarrow 5/2_1^+$, transition in ^{17}O as due to the neutron transition from the $2s_{1/2}$ to $1d_{5/2}$ orbits, the experimental value of $B(E2) = 2.39(3)$ W.u. (Weisskopf units) requires an effective neutron charge of $e_n = 0.534(3)e$. This value is close to $e_n = 0.5e$, which is the default often adopted for shell model calculations. However, turning to ^{18}O , and identifying the $2_1^+ \rightarrow 0_1^+$ transition with $\nu(d_{5/2})_{2+}^2 \rightarrow \nu(d_{5/2})_{0+}^2$, requires $e_n = 1.054(14)e$ to explain the observed transition strength of $3.32(9)$ W.u. One might hope that this discrepancy between ^{17}O and ^{18}O would be resolved by a shell model calculation in the full sd model space with one of the “universal” sd interactions, but it is not. Such shell model calculations describe ^{17}O well. The same calculations, however, fall short of explaining the $B(E2 : 2_1^+ \rightarrow 0_1^+)$ in ^{18}O by a factor of nearly 3. It is worth noting that the experimental $B(E2)$ for ^{18}O is based on about 20 independent measurements by four independent techniques, all in reasonable agreement. The conclusion must be that the effective charge handles ^{17}O , but fails for ^{18}O due to additional correlations.

Table 2 shows shell model calculations for the reduced transition rate, $B(E2; 2_1^+ \rightarrow 0_1^+)$, in doubly magic nuclides plus or minus two like nucleons. The shell model calculations were performed with NUSHELLX [44] and generally use a contemporary set of interactions for the relevant basis space, and either the recommended effective charges for the selected basis space, or the default $e_p = 1.5e$ and $e_n = 0.5e$, for protons and neutrons, respectively. The effective charges required to bring the shell model calculations into agreement with experiment are shown. For those nuclides adjacent to ^{48}Ca and ^{56}Ni , calculations were run in a basis that treats these nuclei as doubly magic, as well as in the full fp shell, which allows for excitations from the $1f_{7/2}$ shell across the $N, Z = 28$ shell gap into the $2p_{3/2}$, $1f_{5/2}$, and $1p_{1/2}$ orbits. These calculations account for the neutron core excitation in ^{48}Ca , including the $\nu(2p - 2h) 0^+$ state at 5.46 MeV, but cannot describe the $\pi(2p - 2h) 0^+$ state at 4.28 MeV; see Figure 2, and cf. Figure 60.

Table 2. Effective charges, e_p and e_n , in units of the elementary charge e , for $B(E2; 2_1^+ \rightarrow 0_1^+)$ in doubly magic nuclides plus or minus two like nucleons. The experimental values are from the Evaluated Nuclear Structure Data File (ENSDF) [22], with the following exceptions: ^{46}Ar [45], $^{130,134}\text{Sn}$ [46,47], ^{134}Te [48], ^{210}Po [49].

Nuclide	Basis ^a	Interaction	B(E2) (W.u.)		e_p	e_n
			Experiment	Shell Model ^b		
¹⁶ O core:						
¹⁴ C	p	pewt [50,51]	1.8 ± 0.3	5.42	0.86 ± 0.07	–
¹⁸ O	sd	usdb [52]	3.32 ± 0.09	1.16 ^c	–	0.76 ± 0.01
¹⁸ Ne	sd	usdb [52]	17.7 ± 1.8	10.64 ^c	1.75 ± 0.09	–
⁴⁰ Ca core:						
³⁸ Ar	sd	usdb [52]	3.4 ± 0.16	3.36 ^c	1.37 ± 0.03	–
³⁸ Ca	sd	usdb [52]	2.5 ± 0.6	0.37 ^c	–	1.17 ± 0.14
⁴² Ca	f7	f7cdpn [53]	9.5 ± 0.4	0.64	–	1.92 ± 0.04
	fp	gx1a [54,55]	9.5 ± 0.4	0.77	–	1.76 ± 0.04
⁴² Ti	f7	f7cdpn [53]	16 ± 4	5.80	2.49 ± 0.31	–
	fp	gx1a [54,55]	16 ± 4	6.94	2.28 ± 0.28	–
⁴⁸ Ca core:						
⁴⁶ Ar	sdpf	sdpfmu [56]	4.4 ± 0.4	7.77 ^d	–	–
⁴⁶ Ca	f7	f7cdpn [53]	3.63 ± 0.3	0.60	–	1.23 ± 0.05
	fp	gx1a [54,55]	3.63 ± 0.3	0.94	–	0.98 ± 0.04
⁵⁰ Ca	ho	ho [57]	0.68 ± 0.02	0.83	–	0.45 ± 0.01
	fp	gx1a [54,55]	0.68 ± 0.02	0.84	–	0.45 ± 0.01
⁵⁰ Ti	ho	ho [57]	5.46 ± 0.19	5.05	1.56 ± 0.03	–
⁵⁰ Ti	fp	gx1a [54,55]	5.46 ± 0.19	9.19	–	–
⁵⁶ Ni core:						
⁵⁴ Fe	f7	f7cdpn [53]	11.1 ± 0.3	4.76	2.29 ± 0.03	–
	fp	gx1a [54,55]	11.1 ± 0.3	13.08	–	–
⁵⁴ Ni	f7	f7cdpn [53]	10 ± 2	0.53	–	2.17 ± 0.22
	fp	gx1a [54,55]	10 ± 2	6.69	–	–
⁵⁸ Ni	ho	ho [57]	10.0 ± 0.4	0.83	–	1.73 ± 0.03
	fp	gx1a [54,55]	10.0 ± 0.4	9.28	–	–
¹³² Sn core:						
¹³⁰ Sn	jj55	sn100 [33]	1.18 ± 0.25	0.76	–	0.62 ± 0.06
¹³⁴ Sn	jj56	jj56cdb [33]	1.42 ± 0.25	0.94	–	0.62 ± 0.05
¹³⁴ Te	jj55	sn100 [33]	5.12 ± 0.21	4.00	1.70 ± 0.03	–
²⁰⁸ Pb core:						
²⁰⁶ Pb	jj56	khhe [58]	2.8 ± 0.09	0.79	–	0.94 ± 0.02
²¹⁰ Pb	jj67	khpe [58]	1.4 ± 0.4	0.55	–	0.80 ± 0.11
²¹⁰ Po	jj67	khpe [58]	1.83 ± 0.28 ^e	3.51	1.08 ± 0.08	–

^a Model basis spaces:

- p: π & ν ($1p_{3/2}, 1p_{1/2}$)
- sd: π & ν ($1d_{5/2}, 2s_{1/2}, 1d_{3/2}$)
- f7: π & ν ($1f_{7/2}$)
- fp: π & ν ($1f_{7/2}, 2p_{3/2}, 1f_{5/2}, 2p_{1/2}$)
- sdpf: π ($1d_{5/2}, 1d_{3/2}, 2s_{1/2}$); ν ($1f_{7/2}, 2p_{3/2}, 1f_{5/2}, 2p_{1/2}$)
- ho: π ($1h_{7/2}$); ν ($2p_{3/2}, 1f_{5/2}, 2p_{1/2}$)
- jj55: π & ν ($1g_{7/2}, 2d_{5/2}, 2d_{3/2}, 3s_{1/2}, 1h_{11/2}$)
- jj56: π ($1g_{7/2}, 2d_{5/2}, 2d_{3/2}, 3s_{1/2}, 1h_{11/2}$); ν ($1h_{9/2}, 2f_{7/2}, 2f_{5/2}, 3p_{3/2}, 3p_{1/2}, 1i_{13/2}$)
- jj67: π ($1h_{9/2}, 2f_{7/2}, 2f_{5/2}, 3p_{3/2}, 3p_{1/2}, 1i_{13/2}$); ν ($1i_{11/2}, 2g_{9/2}, 2g_{7/2}, 3d_{5/2}, 3d_{3/2}, 4s_{1/2}, 1j_{15/2}$)

^b The default charges are $e_p = 1.5$ and $e_n = 0.5$, unless otherwise indicated.

^c For usdb the recommended values $e_p = 1.36$, $e_n = 0.45$ were used.

^d For sdpfmu the recommended values $e_p = 1.35$, $e_n = 0.35$ were used.

^e This experimental value has been questioned; see text.

There is no overall pattern in the effective charges shown in Table 2. Most of the shell model $B(E2)$ values are within a factor of 2 to 3 of the experiment; however, those for the calcium isotopes, ³⁸Ca and ⁴²Ca, are underestimated by an order of magnitude. The

experimental $B(E2)$ value for ^{46}Ar is almost a factor of two smaller than theory. While a lifetime measurement [59] gave a $B(E2)$ value consistent with theory, the weight of evidence from independent Coulomb excitation measurements [45,60,61] makes the adopted value in Table 2 firm and in tension with theory.

Good agreement in the fp-shell calculation is obtained for ^{50}Ca and ^{54}Fe . As noted above, in these cases, ^{48}Ca and ^{56}Ni are not doubly magic cores but part of the fp model space. It is puzzling that the calculation for ^{50}Ti in the same model space is twice the experiment, but the restricted $f_{7/2}$ model space agrees with experiment.

Moving to heavier nuclei, the effective charges in the ^{132}Sn region are near the default values [62], although most recent calculations adopt $e_p \approx 1.7e$ and $e_n \approx 0.8e$ [32,34,63,64]. The measured $B(E2)$ for ^{130}Sn [46,47] is lower than theory and the experimental systematics (see [65]); the experiment should be repeated.

In the ^{208}Pb region, e_n approaches $+e$. The experimental result for ^{210}Po is problematic. As shown below in this Section, an analysis of higher-excited states in ^{210}Po corresponding nominally to the $\pi 1h_{9/2}^2$ configuration implies $e_p \approx 1.5e$. The experimental $B(E2)$ in Table 2 for ^{210}Po is deduced from a recent lifetime measurement by the Doppler shift attenuation method following the $^{208}\text{Pb}(^{12}\text{C}, ^{10}\text{Be})^{210}\text{Po}$ reaction, which gave $\tau = 2.6 \pm 0.4$ ps [49]. This new result is certainly an improvement on the previous measurement which used (d,d') above the Coulomb barrier to excite a ^{210}Po target [66]. However, it is difficult to measure such a short lifetime below the longer-lived 4^+ , 6^+ and 8^+ states that tend to also be populated in heavy ion reactions; Kocheva et al. [49] recommend additional experiments. Coulomb excitation of the radioactive beam (e.g., at ISOLDE where ^{210}Po activity remains in used ion sources) would be a possibility, avoiding the problem of feeding from the longer-lived higher excited states.

In several cases in Table 2, a j^2 approximation is (at least at face value) a reasonable starting point. For the case of ^{14}C , it is not: holes in ^{16}O nominally occupy the $1p_{1/2}$ orbit which must couple with $1p_{3/2}$ to form a 2^+ state. In other cases, like ^{130}Sn , the $2d_{3/2}$, $3s_{1/2}$, and $1h_{11/2}$ single-particle orbits are so close in energy that a single- j^2 approximation cannot be applicable.

In some respects, the comparison of effective charges from the $2_1^+ \rightarrow 0_1^+$ transitions alone may be considered selective and not altogether fair. However, as discussed in this Section, it fits our purpose, which is to examine the emergence of collectivity in nuclei. To explore further the successes and limitations of the shell model approach, comparisons of $E2$ strengths and g factors are now made for a selection of the semimagic nuclides in Table 2 that can be approximated as a single- j^2 configuration adjacent to a doubly magic core. Later in this section and again in Section 8, we argue that the properties of 2_1^+ states, especially their electromagnetic properties, play an important part in developing an understanding of the emergence of collectivity in nuclei.

Table 3 shows the effective charges required to explain $B(E2)$ values between low-excitation states associated with nominal j^2 configurations in doubly magic nuclides plus or minus two like nucleons. For most cases, only protons or neutrons are active in the basis space. For ^{50}Ti and ^{54}Fe , calculations were performed in the fp model space which allows neutron excitations across $N = 28$; thus, both protons and neutrons contribute to the transition rate. In these cases, the proton effective charge required by experiment was evaluated assuming that $e_n = 0.5e$. The uncertainty given is due to the uncertainty in the experimental $B(E2)$ alone. Concerning the uncertainty in the assumed value of e_n , it can be noted that $e_p + e_n$ is near constant for ^{50}Ti , so a decrease in e_n by say $0.1e$ leads to an increase in e_p of approximately 0.1. For ^{54}Fe , the value of e_p is less sensitive to the assumed value of e_n .

As expected, the effective charge is generally reduced when the basis space is enlarged; the j^2 model is obviously an oversimplification. However, it is a better approximation for the nuclei adjacent to the $N > Z$ doubly magic ^{132}Sn and ^{208}Pb . One reason is that, for nuclei adjacent to $N = Z$ doubly closed shells, intruder configurations are present at

low energy and these place the active nucleons in a much larger Hilbert space than can be handled by the shell model.

From Table 3, one can conclude that the effective charge required to describe the $B(E2; 2_1^+ \rightarrow 0_1^+)$ transition is often greater than that required to explain the transitions between the higher spins in the j^2 multiplet (i.e., the $E2$ decays of the states with $J^\pi = 4^+, 6^+, \dots (2j)^+$), particularly for the j^2 model. One can also see that the effective charges exceed the bare nucleon values, even in the large basis shell model calculations. The effective proton charges are reduced significantly for ^{50}Ti and ^{54}Fe when the basis space is expanded to include the whole fp shell. The proton charge deduced for ^{50}Ti even approaches unity, but this assumes that $e_n = 0.5e$.

Table 3. Effective charges for nominal j^2 configurations in selected doubly magic nuclides plus or minus two like nucleons. The effective charges are evaluated assuming a pure j^2 configuration and for the mixed configurations of the (large basis) shell model (SM) calculations in Table 2. The experimental transition rates, $B(E2)_{\text{exp}}$, are from ENSDF [22] and from the references in Table 2.

Nuclide	Config.	Transition	$B(E2)_{\text{exp}}$ (W.u.)	e^{eff}	
				j^2	SM
Protons:					
^{18}Ne	$\pi 1d_{5/2}^2$	$2_1^+ \rightarrow 0_1^+$	17.7 ± 1.8	2.43 ± 0.12	1.75 ± 0.09
		$4_1^+ \rightarrow 2_1^+$	8.9 ± 1.2	2.08 ± 0.14	1.34 ± 0.09
^{42}Ti	$\pi 1f_{7/2}^2$	$2_1^+ \rightarrow 0_1^+$	16 ± 4	2.5 ± 0.3	2.28 ± 0.28
		$6_1^+ \rightarrow 4_1^+$	3.2 ± 0.2	1.65 ± 0.05	0.95 ± 0.03
^{50}Ti	$\pi 1f_{7/2}^2$	$2_1^+ \rightarrow 0_1^+$	5.46 ± 0.19	1.56 ± 0.03	1.06 ± 0.03^a
		$4_1^+ \rightarrow 2_1^+$	5.5 ± 1.5	1.57 ± 0.21	1.1 ± 0.2^a
		$6_1^+ \rightarrow 4_1^+$	3.14 ± 0.13	1.76 ± 0.04	1.24 ± 0.03^a
^{54}Fe	$\pi 1f_{7/2}^{-2}$	$2_1^+ \rightarrow 0_1^+$	11.1 ± 0.3	2.29 ± 0.03	1.36 ± 0.02^a
		$4_1^+ \rightarrow 2_1^+$	6.3 ± 1.3	1.73 ± 0.18	1.60 ± 0.18^a
		$6_1^+ \rightarrow 4_1^+$	3.24 ± 0.06	1.84 ± 0.02	1.36 ± 0.01^a
^{134}Te	$\pi 1g_{7/2}^2$	$2_1^+ \rightarrow 0_1^+$	5.12 ± 0.21	1.80 ± 0.04	1.70 ± 0.03
		$4_1^+ \rightarrow 2_1^+$	4.3 ± 0.4	1.65 ± 0.08	1.58 ± 0.07
		$6_1^+ \rightarrow 4_1^+$	2.05 ± 0.04	1.69 ± 0.02	1.54 ± 0.02
^{210}Po	$\pi 1h_{9/2}^2$	$2_1^+ \rightarrow 0_1^+$	1.83 ± 0.28^b	1.07 ± 0.08	1.08 ± 0.08
		$4_1^+ \rightarrow 2_1^+$	4.46 ± 0.18	1.56 ± 0.03	1.50 ± 0.03
		$6_1^+ \rightarrow 4_1^+$	3.05 ± 0.09	1.55 ± 0.02	1.50 ± 0.02
		$8_1^+ \rightarrow 6_1^+$	1.12 ± 0.04	1.48 ± 0.03	1.44 ± 0.03
Neutrons:					
^{18}O	$\nu 1d_{5/2}^2$	$2_1^+ \rightarrow 0_1^+$	3.32 ± 0.09	1.054 ± 0.014	0.76 ± 0.01
		$4_1^+ \rightarrow 2_1^+$	1.19 ± 0.06	0.76 ± 0.02	0.51 ± 0.01
^{42}Ca	$\nu 1f_{7/2}^2$	$2_1^+ \rightarrow 0_1^+$	9.5 ± 0.4	1.92 ± 0.04	1.76 ± 0.04
		$4_1^+ \rightarrow 2_1^+$	8.3 ± 1.2	1.80 ± 0.13	1.6 ± 0.1
		$6_1^+ \rightarrow 4_1^+$	0.777 ± 0.022	0.82 ± 0.01	0.47 ± 0.01
^{134}Sn	$\nu 2f_{7/2}^2$	$2_1^+ \rightarrow 0_1^+$	1.42 ± 0.25	0.80 ± 0.07	0.62 ± 0.05
		$6_1^+ \rightarrow 4_1^+$	0.89 ± 0.17	0.94 ± 0.09	0.52 ± 0.05
^{210}Pb	$\nu 2g_{9/2}^2$	$2_1^+ \rightarrow 0_1^+$	1.4 ± 0.4	0.81 ± 0.12	0.80 ± 0.11
		$4_1^+ \rightarrow 2_1^+$	4.8 ± 0.9	1.40 ± 0.13	1.28 ± 0.12
		$6_1^+ \rightarrow 4_1^+$	2.1 ± 0.8	1.11 ± 0.21	1.0 ± 0.2
		$8_1^+ \rightarrow 6_1^+$	0.7 ± 0.3	1.02 ± 0.22	0.90 ± 0.19

^a Evaluated in the fp basis with gx1a interactions and $e_n = 0.5e$. See text for details. ^b This experimental value has been questioned; see text.

There are broadly two scenarios to explain the effective charge. First, and universally applicable, is the coupling of the valence nucleons to collective excitations of the core, including the giant resonances, in such fashion that the concept of an effective charge as a renormalization procedure has some operational justification. Second, and specific to particular cases, is the coupling between the valence nucleons and low-excitation configurations outside the shell model basis. This later scenario means that the shell model configuration is wrong in a more fundamental way.

An examination of the magnetic moments, or rather the g factors ($g = \mu/J$), can distinguish between these scenarios. To this end, Table 4 shows an evaluation of the g factors for those nominal j^2 configuration cases in Table 3 for which there are experimental data. It is useful to make use of the fact that $g(j^n) = g(j)$; that is, the g factor of any number of nucleons in a single-particle orbit is equal to the g factor of the single-particle orbit, independent of the number of nucleons (n) and the resultant spin.

The empirical g factor of the j^2 configuration was evaluated as the average of the g factors of the ground-states of the neighbouring nuclei with $A \pm 1$ and odd- Z or odd- N , as appropriate. The shell model calculations in the sd and fp spaces use the default effective $M1$ operator for those basis spaces. For the $jj55$ space, the $M1$ operator is as in Refs. [48,64,65,67,68]. For ^{210}Pb and ^{210}Po ($jj67$), the effective g_s was set to 70% of the free nucleon value and g_l adjusted to reproduce the ground state g factors of ^{209}Pb ($\nu 2g_{9/2}$) and ^{209}Po ($\pi 1h_{9/2}$). The values so obtained conform to expectations ($g_l(\pi) \approx 1.1$ and $g_l(\nu) \lesssim 0$). It is important to note that the renormalization of the $M1$ operator is due to processes quite distinct from those that give rise to the effective charge, namely meson exchange currents, and core polarization. Here, the core polarization involves particle-hole excitations between spin-orbit partners, which couple strongly to the $M1$ operator. It thus differs in a fundamental way from the core polarization associated with the $E2$ effective charge.

It is convenient to discuss the results in Table 4 beginning with the heavier nuclei, ^{210}Pb and ^{210}Po . For these nuclei adjacent to ^{208}Pb , there is good agreement between the experimental g factors of the 6_1^+ and 8_1^+ states, and both the empirical j^2 estimate and the shell model. These can be considered text book examples. It is unfortunate that there are no data for the 2_1^+ and 4_1^+ states, which, as the following discussion in this Section suggests, might show additional collectivity.

Turning to ^{134}Te , the $E2$ and g factor data for the $\pi(1g_{7/2})^2$ multiplet are complete, and there is reasonable agreement with both the j^2 model and the shell model calculations. A detailed analysis has been given in Ref. [48], wherein it is shown that there is additional quadrupole collectivity in the 2_1^+ state of ^{134}Te that is not accounted for by large-basis shell model calculations that assume an inert ^{132}Sn core. It was demonstrated that coupling the valence $\pi g_{7/2}^2$ configuration to a core vibration with the properties of the first-excited state in ^{132}Sn can readily account for the observed $2_1^+ \rightarrow 0_1^+$ transition strength in ^{134}Te , and that the wavefunctions of the 2_1^+ , 4_1^+ and 6_1^+ states of ^{134}Te nevertheless remain dominated by the $\pi g_{7/2}^2$ configuration. It can be concluded that ^{132}Sn is a relatively inert shell-model core. The caveat, however, is that the shell model calculations still require relatively large effective charges.

In the fp shell, ^{50}Ti shows quite good agreement with both the j^2 model and the shell model. For ^{54}Fe , the experimental g factors show better agreement with the large-basis shell model than the j^2 model. The shell model calculations in the fp basis with the $gx1a$ interactions do a reasonable job of describing the different behaviour of the g factors in ^{50}Ti and ^{54}Fe .

The isotopes with two neutrons outside the $N = Z$ cores ^{16}O and ^{40}Ca show similar behaviour: $g(2_1^+)$ is reduced significantly in magnitude compared to both the j^2 model and the shell model calculation, whereas the higher excited states, 4^+ in ^{18}O , and 6^+ in ^{42}Ca , have g factors in agreement with both the j^2 model and the larger-basis shell model. In

these isotopes, both the $E2$ transition strengths and the g factors indicate that the 2^+ state must contain collective admixtures. Writing the 2_1^+ wavefunction in the form

$$|2_1^+\rangle = \alpha|\text{SM}\rangle + \sqrt{1 - \alpha^2}|\text{coll}\rangle, \tag{7}$$

where SM denotes the part from the shell model basis space and “coll” denotes the collective part (from multiparticle-multihole excitations), implies that

$$g(2_1^+) = \alpha^2 g_{\text{SM}} + (1 - \alpha^2)g_{\text{coll}}. \tag{8}$$

Assuming that the collective g factor is $g_{\text{coll}} \approx Z/A \approx 0.5$, and taking the shell model g factor from Table 4 implies that there is a collective contribution of $\alpha^2 = 20 \pm 2\%$ in the first excited state of ^{18}O , and a huge $59 \pm 5\%$ collective contribution in the first-excited state of ^{42}Ca . This mixing in ^{42}Ca is in excellent agreement with a 50% collective contribution deduced from Coulomb excitation data and one-neutron transfer reaction data (see Figures 41 and 42 for full details). To explain the observed g factor in ^{42}Ca , Ref. [69] requires that the basis space be expanded to include the sd as well as fp orbits for both protons and neutrons. This strongly collective structure of the 2_1^+ state is in stark contrast with the near pure $\nu(f_{7/2})^2$ structure of the 6_1^+ state.

Table 4. g factors for nominal j^2 configurations in doubly magic nuclides plus or minus two like nucleons. Data are from [70] (with a correction for ^{54}Fe $g(2_1^+)$ from [71]).

Nuclide	Config.	J_i^π	g (exp)	g (emp j^2)	g (SM)
^{18}O	$\nu 1d_{5/2}^2$	2_1^+	-0.285 ± 0.015	-0.685	-0.476
		4_1^+	-0.63 ± 0.10	-0.685	-0.603
^{42}Ca	$\nu 1f_{7/2}^2$	2_1^+	0.04 ± 0.06	-0.416	-0.615
		6_1^+	-0.415 ± 0.015	-0.416	-0.538
^{50}Ti	$\pi 1f_{7/2}^2$	2_1^+	1.45 ± 0.08	1.538	1.235
		6_1^+	1.55 ± 0.17	1.538	1.379
^{54}Fe	$\pi 1f_{7/2}^{-2}$	2_1^+	0.95 ± 0.11	1.407	1.091
		6_1^+	1.37 ± 0.03	1.407	1.354
^{134}Te	$\pi 1g_{7/2}^2$	2_1^+	0.76 ± 0.09	0.833	0.837
		4_1^+	0.75 ± 0.50	0.833	0.833
		6_1^+	0.847 ± 0.025	0.833	0.842
^{210}Pb	$\nu 2g_{9/2}^2$	6_1^+	-0.312 ± 0.015	-0.320	-0.304^a
		8_1^+	-0.312 ± 0.007	-0.320	-0.307^a
^{210}Po	$\pi 1h_{9/2}^2$	6_1^+	0.913 ± 0.008	0.913	0.912^b
		8_1^+	0.919 ± 0.006	0.913	0.911^b

^a $g_s(\nu) = 0.7g_s^{\text{free}}(\nu) = -2.678$ and $g_l(\nu) = -0.033$ set to reproduce the ground-state moment of ^{209}Pb .
^b $g_s(\pi) = 0.7g_s^{\text{free}}(\pi) = 3.910$ and $g_l(\pi) = 1.16$ set to reproduce the g.s. moment of ^{209}Bi .

To sum up, for the nuclei with $N = Z$ cores, the 2_1^+ structure is apparently affected by mixing with low-excitation deformed multiparticle-multihole states, whereas the higher-spin states are closer to the naïve j^2 structure. For $N > Z$ cores, the low-spin states are better approximated by the empirical j^2 model and quite well described by the shell model. However, in all cases, a substantial effective charge is required to explain the $E2$ strength, even when the g factor suggests a relatively pure shell model configuration.

Although a first assessment of the effective charges required to explain the $B(E2; 2_1^+ \rightarrow 0_1^+)$ data adjacent to closed shells may appear to show no pattern, some features can be identified: (i) shape coexistence and mixing must be taken into account when the doubly magic core has $N = Z$, (ii) there are always non-zero corrections to the nucleonic charges. Defining δe_p and δe_n , where $e_p^{\text{eff}} = (1 + \delta e_p)e$ and $e_n^{\text{eff}} = \delta e_n e$, the common assumption that $\delta e_p \approx \delta e_n \approx 0.5$ is seen to be valid in many cases. However, δe_n appears to increase in heavier nuclei.

The above data and discussion shows that, for $E2$ transition strengths, the bare electric charges, $e_p = +1e$ and $e_n = 0$, do not work for configurations confined to a valence shell. A correction to the effective charges $\delta e_{p(n)} \gtrsim 0.5$ is usually required, even when the low-lying core excitations are taken into account. Certainly, the use of effective charges has provided a means for exploring nuclear structure using the shell model applied to nuclei that do not have closed shells. However, such practice buries important aspects of the origin of quadrupole collectivity in nuclei; one cannot learn the whole story about the origin of nuclear collectivity using such theories. We suggest that the path forward is two-fold: first, to develop models that obviate the need for effective charges, and second, where the use of effective charges is unavoidable, to formulate appropriate strategies to understand and manage their use.

There are “standard” approaches to evaluate effective charge—often conceptually based on the particle-vibration model of Bohr and Mottelson for nuclei with a single valence nucleon. The vibration can be described microscopically by particle–hole excitations in a Random Phase Approximation (RPA)-type approach [72–76]. There is then some choice of—and sensitivity to—the interaction used in the RPA calculation [76]. This procedure, based on single particle–hole excitations, will not account for the effects of mixing between the valence configurations and low-excitation multiparticle-multihole configurations, which will particularly affect the $E2$ effective charge. The procedure to generalize from one valence nucleon to many is less often discussed. The effective charge must vary to some extent with the number of valence nucleons, but, in practice, it is usually held constant.

Some further comments on the path forward are made in Section 10.

A wider view of what one means by the shell model as an independent-particle model is provided by quasi-elastic electron scattering knockout of protons from closed shell nuclei. A summary view is provided in Figure 15. Quasielastic electron-scattering knockout of protons is a probe of independent-particle behaviour in nuclei that is distinct from the more familiar one-nucleon transfer reaction spectroscopy such as $(d, {}^3\text{He})$. First, the interaction is purely electromagnetic; second, entrance and exit channel effects are limited to the outgoing (high-momentum) proton. Thus, confidence can be placed in the extracted spectroscopic factors for $(e, e'p)$ reactions and the revelation that the single-particle view is “incomplete”. The important insight is that one is never dealing with independent particles in a quantum many-body system such as the atomic nucleus: correlations are ubiquitous. Indeed, there are severe warnings of this in the theoretical literature, e.g., [77,78]. These correlations go much deeper than pairing correlations. The subject of nucleon correlations in nuclei is broad. Reference to them in the narrative here is minimal because our focus is on systematics of low-energy phenomenology. For the interested reader, a useful entry point is Ref. [79]. For recent access to the topic, a useful source is Ref. [80].

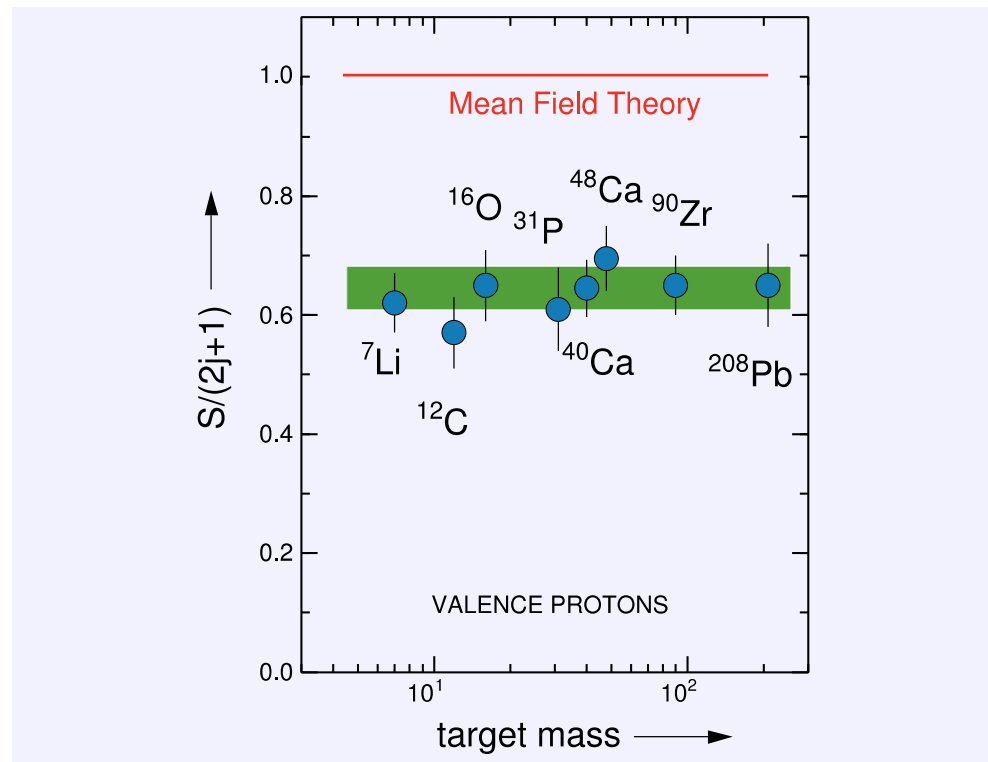


Figure 15. Spectroscopic strengths from quasielastic electron scattering knockout of valence protons, $A(e, e'p)$. Adapted from [81] (taken from [82]). The conclusion is, relative to a mean-field view, that never more than 70% of independent-particle strength is manifested in valence nucleon structure, even at doubly closed shells, i.e., other degrees of freedom are contributing to these structures.

The dilemma presented by the data in Figure 15 is a direct confrontation of the shell model approach to nuclear structure, so it can be viewed as a restatement of the question that is used for the title of this review. The data raise two questions: (1) Where has the single-particle strength gone? (2) What has replaced the single-particle strength? We do not attempt to answer these questions. Note that we are in good (bad?) company with the Standard Model of particles and fields. The Standard Model has a plethora of parameters, and nobody knows where they come from. There is one difference in our favour: we believe that protons and neutrons underlie the low-energy degrees of freedom in nuclei, but to employ their bare parameters requires much larger model spaces. Let us note the subtle point regarding correlations: it is primarily the number of configurations involved, not the number of particles, that is relevant. Shell model computations are only tractable in (relatively) small Hilbert spaces: the accumulating evidence is that these spaces are too small. There is an exponential growth in matrix dimensions as the shell model space is increased. However, “symmetry guided” approaches are beginning to circumvent this limitation [83]. A few details are given in Section 10.

It is relevant to note here that the missing strength in $(e, e'p)$ knockout and the effective charge problem must be related at a fundamental level because the $T(E\lambda)$ matrix elements for mass A can be expanded in terms of one-body spectroscopic factors connecting A and $A - 1$. Whether the general missing strength in transfer reactions [84] is associated with short-range [85] or long-range [86] correlations is crucial for the question of emerging collectivity. Moreover, the role of this missing strength in the emergence of quadrupole collectivity in nuclei could possibly be illuminated by examining how the effective charges for higher multipolarities, particularly $E4$ and $E6$, compared to those for $E2$ transitions. The negative polarization charge required for the $E6$ transition in ^{53}Fe remains a puzzle; see, e.g., [74,76]. Experimental verification of this sole example of an $E6$ transition is clearly important.

A useful tool that has been used to explore independent-particle degrees of freedom in nuclei has been one-nucleon transfer reactions. However, the so-called spectroscopic strengths extracted from such data must be treated with great caution. This was recognized long ago by Baranger [87], and even earlier by Macfarlane and French [88]. These issues have received renewed attention; see, e.g., [89,90] and references therein for a discussion of the problem. The key issue is: Which nuclei provide the best view of independent-particle degrees of freedom? The approach of looking at how degrees of freedom, which manifestly are not independent-particle degrees of freedom, “intrude” into nuclei where independent-particle degrees of freedom have the best chance of dominating (and are widely assumed to do so [91]) is explored here.

By now, it is recognized that structures, even highly deformed structures, “intrude” into the low-energy excitations of spherical nuclei [41]. However, there are subtleties in the mechanism by which such intruder states appear at low excitation energy. An example is shown in Figure 16 for low-energy excited states in $^{47,49}\text{Ca}$. The naïve interpretation of the low energies of the $3/2^-$ state in ^{47}Ca and the $7/2^-$ state in ^{49}Ca would be that the $N = 28$ shell gap has broken down; but, with an understanding of the manifestation of pairing correlations, the reality is that the $N = 28$ shell gap is strongly present. The persistence of the shell gap can be seen on the right side of Figure 16 where the difference between the observed excitation energies of the first-excited states in ^{47}Ca and ^{49}Ca (which correspond to excitation of a neutron across $N = 28$) and the shell gap energy of ≈ 5.1 MeV is very close to the pairing energy determined from the odd-even staggering in the neutron separation energy, S_n . However, one reads about “collapse of shells” and “dissolving of shells”. This would be true if there were no correlations present; but correlations *are* present.

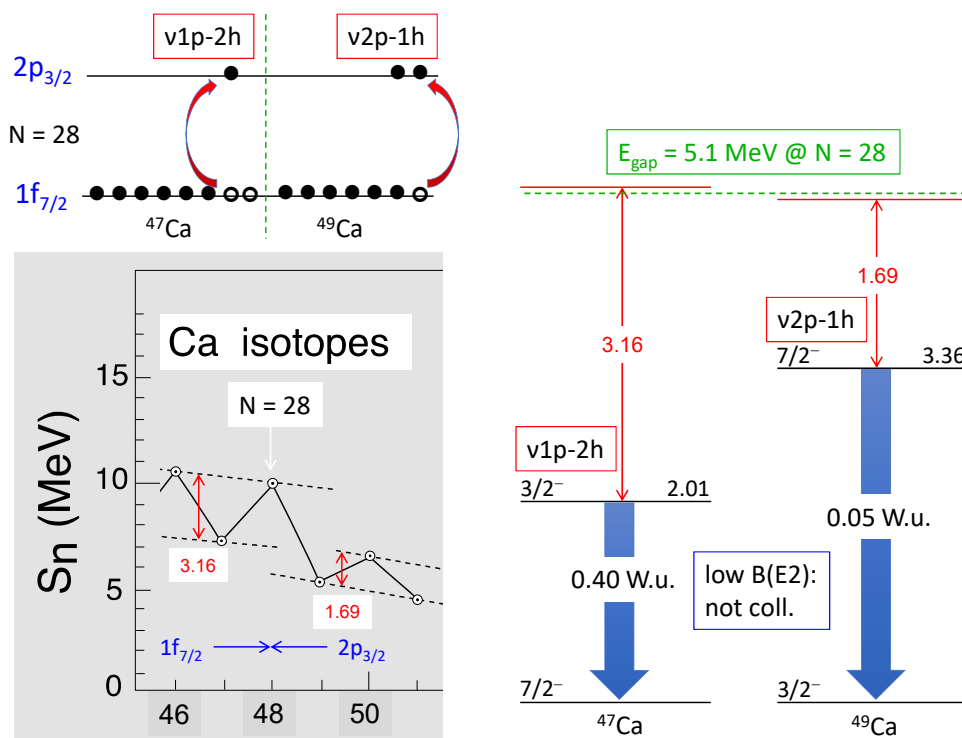


Figure 16. Intruder states in $^{47,49}\text{Ca}$. The low energy of the $3/2^-$ state in ^{47}Ca and the $7/2^-$ state in ^{49}Ca result from pairing correlations. The low $B(E2)$ values associated with these states indicate little or no collective core excitation is involved. The left-hand side of the figure illustrates how a simple estimate of the pairing correlation energy can be made. This analysis shows that the energy gap for $N = 28$ at $Z = 20$ is 5.1 MeV, in line with a well-defined shell gap. The data are taken from ENSDF [22], AME2020 [92], and [90]. Reproduced from [8].

A classic example of intruder states that illustrate the role of deformation is shown in Figure 17 for the odd-mass thallium isotopes. The first hints of these deformed intruder states were recognized long ago [93]; the thallium isotopes were a prime motivational origin of the first review of shape coexistence [94]. The spectroscopic evidence resides in the hindrances of the isomeric transitions and in the band structures associated with the isomer ($9/2^-$ states). The key excitation is a proton across $Z = 82$ to leave a hole pair below $Z = 82$; this hole pair correlates with the valence neutron pairs. These correlations result in near-identical “parabolas” in Bi and Pb isotopes, scaled by the number of proton pairs (see Figure 17 in [41]) and the parabolas exhibit a near collinearity when plotted versus neutron number. The $9/2^-$ intruder structure is the oblate Nilsson $9/2^-$ [505] configuration. There are extensive band structures which are well-described by the Meyer-ter-Vehn model [95,96]. The cores are $A-1$ Hg; the parameters are the same as for odd-Hg $1i_{13/2}$ bands and odd-Au $1h_{11/2}$ bands (viz. $\beta = 0.15$, $\gamma = 37^\circ$). However, these details raise serious questions about using simple shell model configurations when interpreting excited states even in nuclei with one nucleon coupled to a singly closed shell.

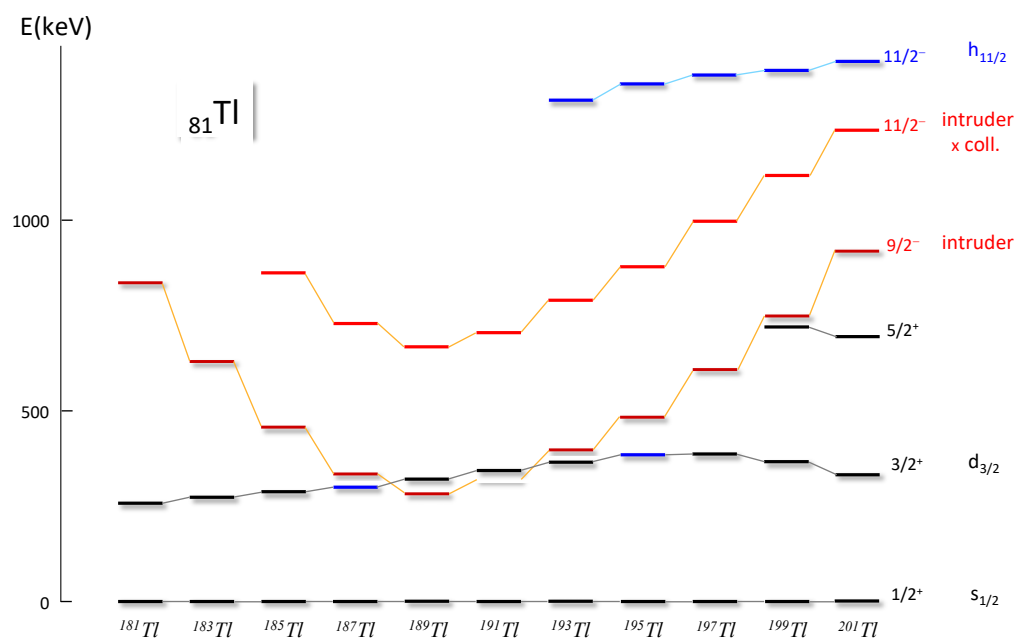


Figure 17. The lowest-energy intruder states in the odd-mass thallium isotopes. A naïve interpretation (from a spherical shell model perspective) would lead to the conclusion that because a $9/2^-$ state is below an $11/2^-$ state in excitation energy, spin–orbit coupling has “broken down” or “collapsed”. In reality, the $9/2^-$ states shown are dominated by proton $1p - 2h$ excitations and are deformed structures: the first collective excitation on these $9/2^-$ states is shown. [41]. Further details are given in the text. Reproduced from [8].

4. Nuclei with Open Shells; Emergence of Collectivity

Nuclear structure is dominated by open-shell nuclei. With excitation of nucleons across shell gaps, and the resulting correlations, “open-shell” configurations intrude to low energy, even to the ground state, in some closed-shell nuclei. Thus, one must understand open-shell nuclei from a microscopic perspective. There are excellent limiting cases for nuclear behavior in open-shell nuclei: these are the strongly deformed nuclei, but a detailed microscopic understanding is lacking. Some perspectives on the current situation are presented here. This is the main focal point of this paper.

The key criterion for this exploration is to identify signatures of shell model structure in open-shell nuclei. Doubly even nuclei obscure shell model structure because of the correlations of pairs of nucleons. Odd-mass nuclei manifestly provide a view, via the unpaired nucleon. However, correlations are still an issue because there can be mixing

of the configurations with different j values within a given shell. However, spin-orbit coupling provides a way forward: each shell has a unique-parity orbital and configurations involving this orbital will be the least mixed of any structures observed.

The power of the systematics of unique-parity states is illustrated in Figures 18 and 19. These figures show the systematics of the positive-parity states in the odd-mass yttrium isotopes across two shells, Figure 18, and of the negative-parity states in the odd-mass $N = 63$ isotones across two shells, Figure 19. Noting that the “parent” j configurations are $1g_{9/2}$ and $1h_{11/2}$, i.e., they differ by one unit of spin, the patterns are similar to the point that they are close to identical. (We recognize that, in the yttrium isotopes, there is a “delayed” onset of collectivity in $^{91,93,95,97}\text{Y}$, an issue which does not concern us here). These patterns suggest that there is an underlying coupling scheme that is defined by just a few simple basic features. Since multi- j shell structures (as manifested in, e.g., the negative-parity states in the $28 < Z < 50$ shell, involving the configurations $1f_{5/2}$, $2p_{3/2}$, and $2p_{1/2}$) are dominated by mixing of these configurations, the unique-parity states may provide a basic guide, via recognized single- j shell dominated patterns, for a mixed j -shell description across all open-shell odd-mass nuclear structure. Thus, we point to patterns that are independent of specific open shells; and to the implication that “shell-specific” interactions may be unnecessarily complex and intricate.

At present, the best description of experimental data for odd-mass nuclei in regions where deformation is not large is: “incomplete”. However, a small number of such nuclei have been sufficiently well studied that they can provide guidance to likely a more complete view of the structure of unique-parity states. The best experimental example of the structure we draw attention to is shown in Figure 20, i.e., the nucleus ^{125}Xe . This is a pattern of organization related to the studies of a single- j particle coupled to a rigid triaxial rotor, by Juergen Meyer-ter-Vehn [95,96]; indeed, he suggested such a pattern in ^{187}Ir , long before detailed spectroscopic information was available: an up-to-date view of ^{187}Ir is shown in Figures 21 and 22, and these strongly support the view. Further note that a very similar pattern appeared in a weak coupling description [97].

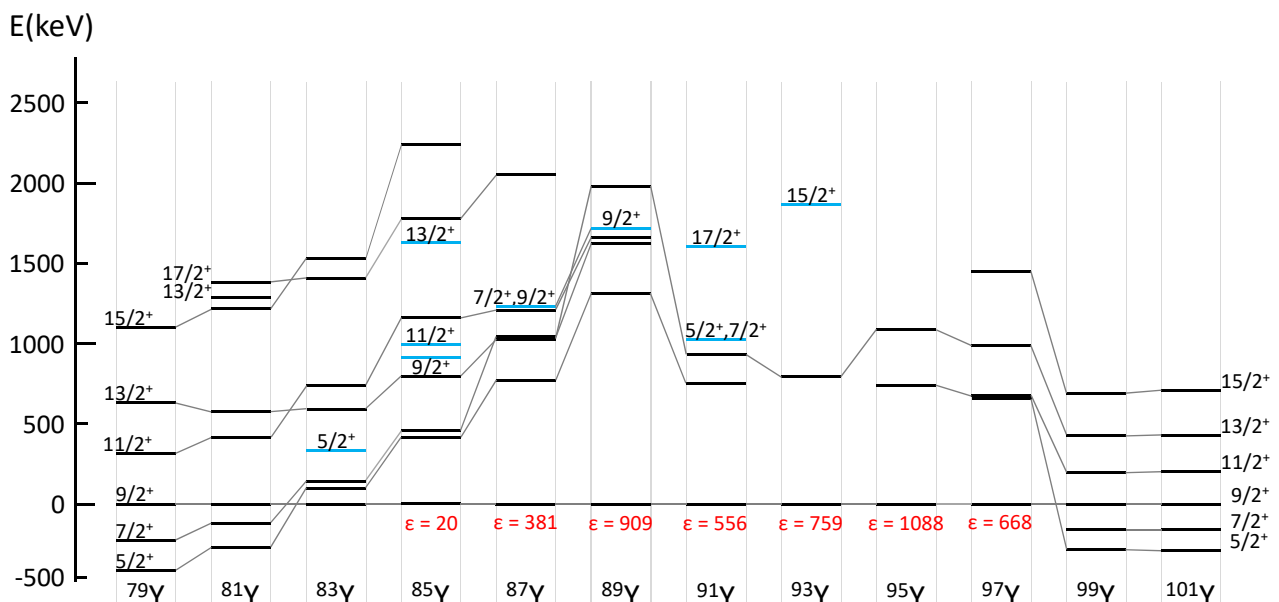


Figure 18. Systematics of the positive-parity states across the yttrium isotopes. These states are the unique-parity states for protons in the $28 < Z < 50$ open shell. Note the emergence of near-identical excitation patterns at the extreme mass numbers (these are the Nilsson configurations $\Omega^\pi [Nn_z \Lambda] = 5/2^+ [422]$, which differ only in rotational energy parameters).

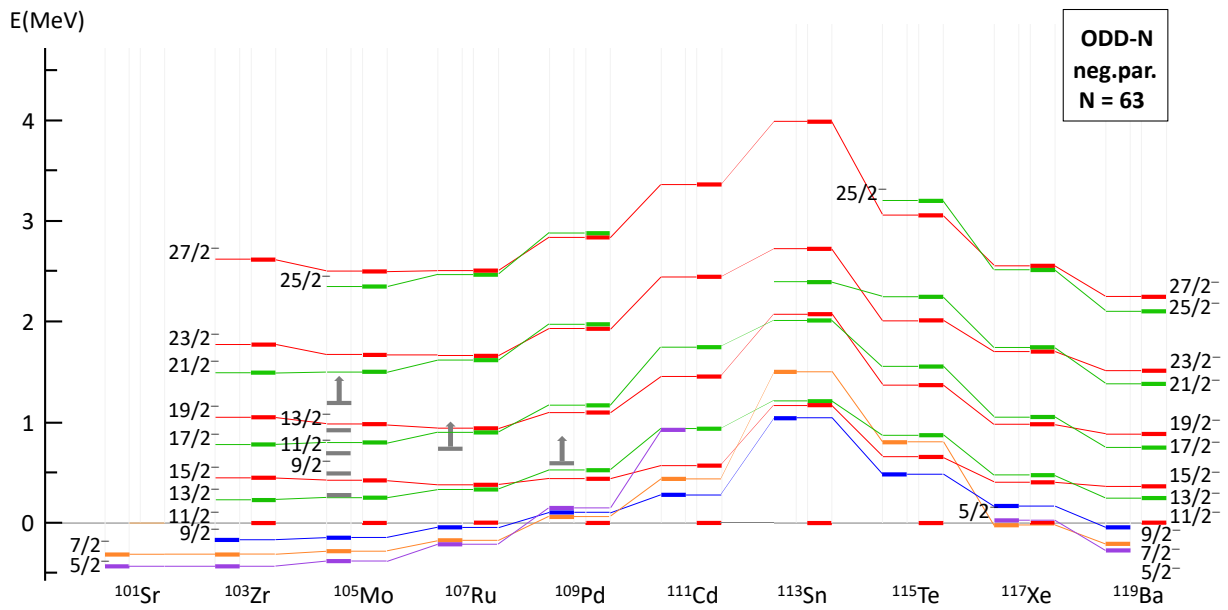


Figure 19. Systematics of negative-parity states across the $N = 63$ isotones. These states are the unique-parity states for neutrons in the $50 < N < 82$ open shell. Note the emergence of near-identical excitation patterns at the extreme mass numbers (these are the Nilsson configurations $\Omega^\pi [Nn_z \Lambda] = 5/2^- [532]$, which differ only in rotational energy parameters and, slightly, in “staggering” or signature splitting).

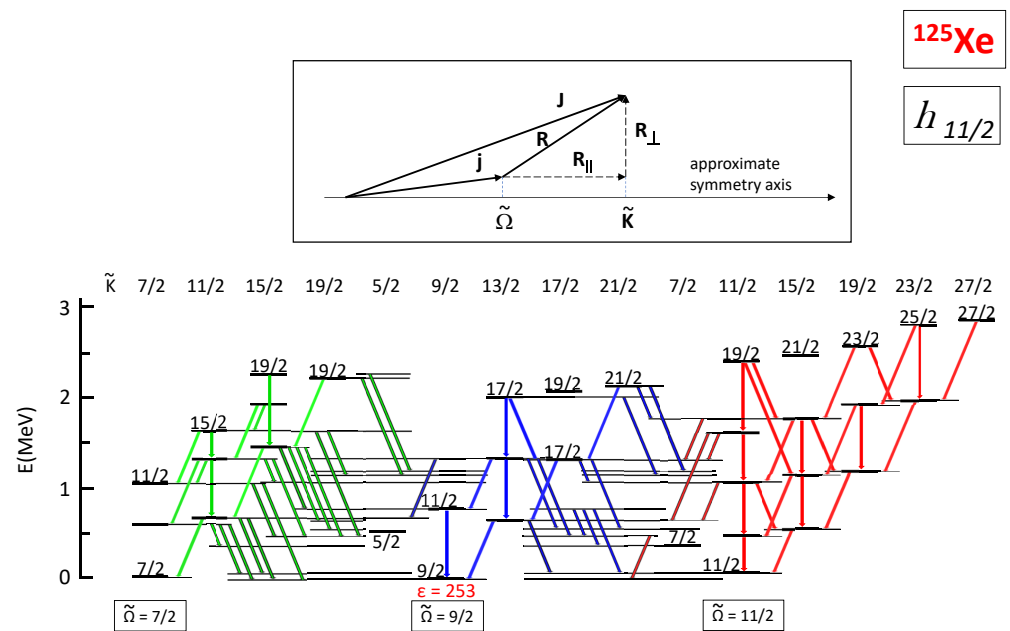


Figure 20. Organization of the unique-parity states in ^{125}Xe , associated with $j = 11/2$ into a “hyperband” pattern due to Meyer-ter-Vehn [95,96]. The inset shows the quantum numbers used to define this pattern [98]. The data are taken from [99], but the pattern was not recognized there. Note that “vertical” $\Delta I = 2$ (i.e., $E2$) transitions are almost totally absent from the observed data. See the text for more details.

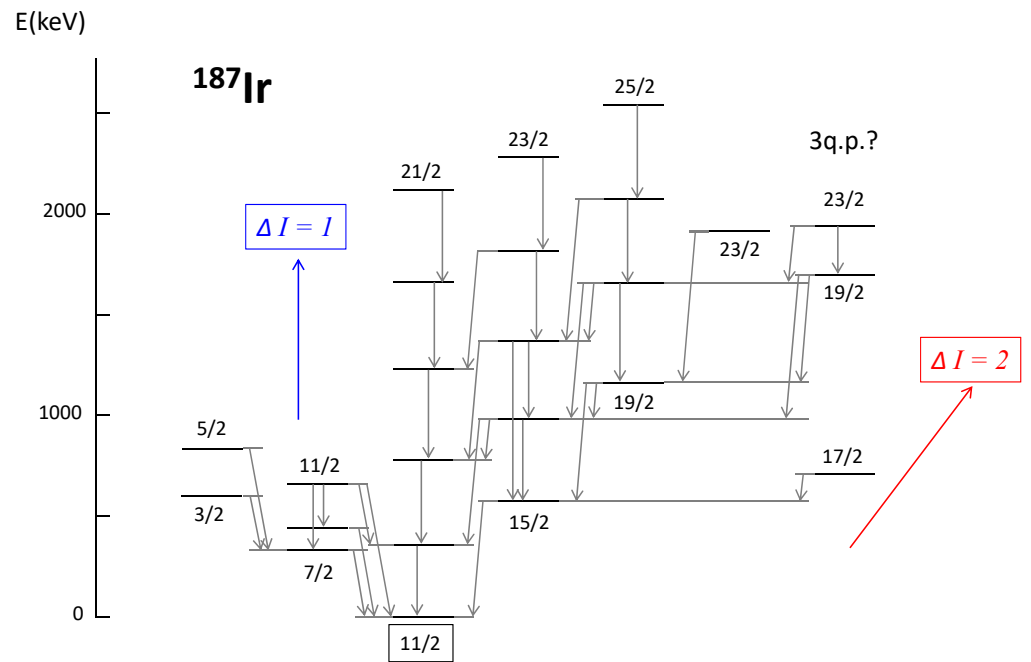


Figure 21. Organization of the unique-parity states in ^{187}Ir associated with $j = 11/2$ into a “hyper-band” pattern due to Meyer-ter-Vehn [95,96]. The data are taken from [100], but the pattern was not recognized there. The states to the right may be associated with three-quasiparticle (3 q.p.) excitations.

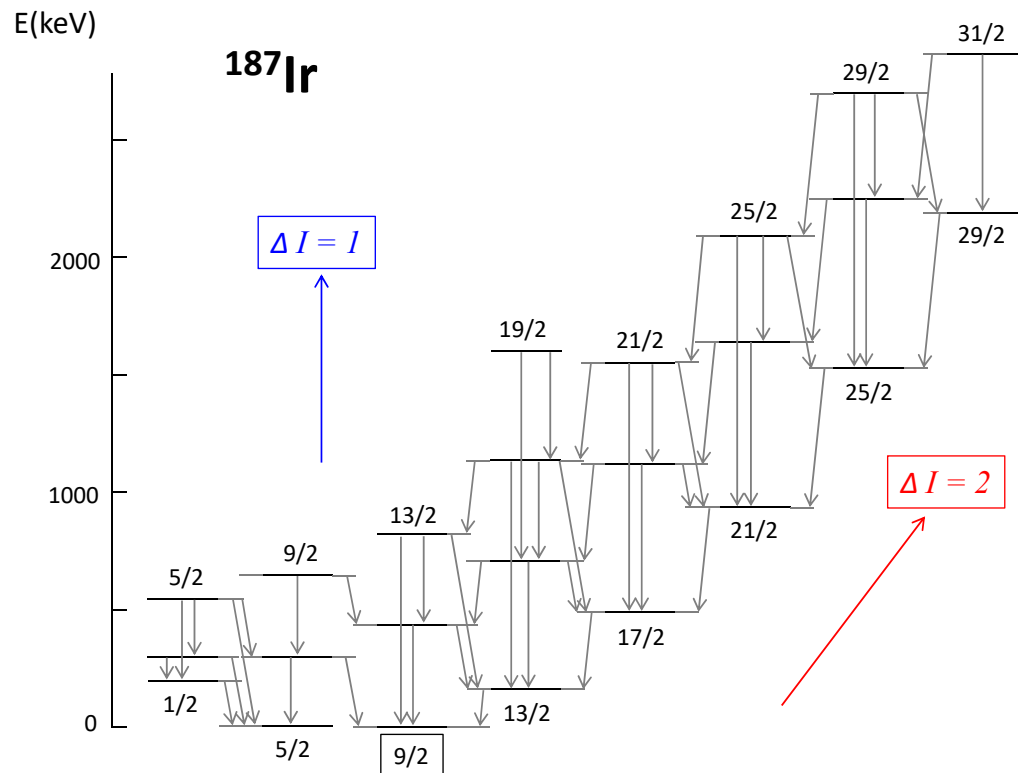


Figure 22. Organization of the unique-parity states in ^{187}Ir associated with $j = 9/2$ intruder configuration into a “hyper-band” pattern due to Meyer-ter-Vehn [95,96]. The data are taken from [100], but the pattern was not recognized there.

The pattern shown in Figure 20 is an organization of experimental data to reflect the dominance of so-called “rotational-aligned” coupling, which occurs in odd-mass nuclei that are not strongly deformed. The leading rotationally aligned set of states is highlighted

in red and extends from the lowest $I = 11/2$ state, diagonally upwards to the right. The spin $11/2$ originates from the $1h_{11/2}$ spherical shell model state, which dominates all low-energy negative-parity states in ^{125}Xe . The lowest tier of states in this set has the spin sequence $11/2, 15/2, 19/2, 23/2, 27/2, \dots$; the tier just above has the spin sequence $13/2, 17/2, 21/2, 25/2, \dots$. However, as shown, this basic pattern is “repeated”, within the set of states highlighted in red, with tiers possessing spin sequences $15/2, 19/2, 23/2, \dots, 17/2, 21/2, \dots$. Furthermore, with sets of states, highlighted in blue and green, the red pattern is repeated built on states of $I = 9/2$ and $7/2$, respectively. The tiers of $\Delta I = 2$ spin sequences, beyond the first two, result from axial asymmetry and the coupling of the $j = 11/2$ particle to an axially asymmetric rotor. The repeated sets of states, coded with different colours, identified as $I = 9/2$ and $I = 7/2$, arise from alignment of the $j = 11/2$ particle in the deformed quadrupole field of ^{125}Xe (such as occurs in the Nilsson model) and rotations about the unfavored axis of the triaxial rotor. These multiple tiers have been considered in some nuclei, by some authors, as candidates for so-called “wobbling”: such wobbling, however, requires strong $E2$ transitions between tiers of states, i.e., decays appearing as vertical arrows; in ^{125}Xe , these transitions appear to be dominated by $M1$ transitions, which might be termed “magnetic” rotation; for further details, see Refs. [95,96]. There is controversy regarding $E2$ admixtures in $\Delta I = 1$ transitions; see the general remarks in [101].

A perusal of the literature over recent decades suggests that the view of Meyer-ter-Vehn has been “forgotten”. The question that arises from consideration of Figures 18–20 (and Figures 21 and 22) is: How small a deformation is meaningful in weakly deformed nuclei? We consider this question but do not reach a final answer. An important outcome of the Meyer-ter-Vehn model [95,96] has been a multi- j version of the model, which is usually described as the particle-triaxial-rotor model (PTRM) [102]. Indeed, it was applied to a description of ^{125}Xe [103,104] before the more recent detailed data set [99]. Thus, the focus here is on a deeper look at the basics of these models, especially near their weak deformation limit.

A major factor in particle-rotor models, both axially symmetric and axially asymmetric, when the deformation is not large, is so-called “Coriolis” or “rotational” alignment. A milestone paper that pointed to this effect was by Frank Stephens and coworkers [105], based on observations in the odd-mass lanthanum isotopes; an up-to-date view of their perspective is shown in Figure 23. An up-to-date view of all known negative-parity states in the odd-mass lanthanum isotopes is shown in Figure 24. Except for ^{133}La , the low-spin couplings are not yet observed. The coupling to low spin is addressed shortly in this Section. The pattern in Figure 23 is referred to as “rotation-aligned” coupling. A simple explanation is given in Figure 25. The essential mechanism is the competition between “rotation alignment” and “deformation alignment”, where deformation alignment is embodied in the basic quantum mechanics of the Nilsson model. The quantum mechanics of rotation alignment is described by the $I \cdot j$ term of the particle-rotor model: Figure 25 is a semi-classical view of this term. A naïve view of the weak-coupling limit of this term is that it dominates the coupling, and the total spin, I and j become collinear. This already appears to happen in the odd-mass lanthanum isotopes for the $I = j + 2$ states, but this does not address the question for the other possible couplings of j (to the even-even core) to yield a resultant total spin I .

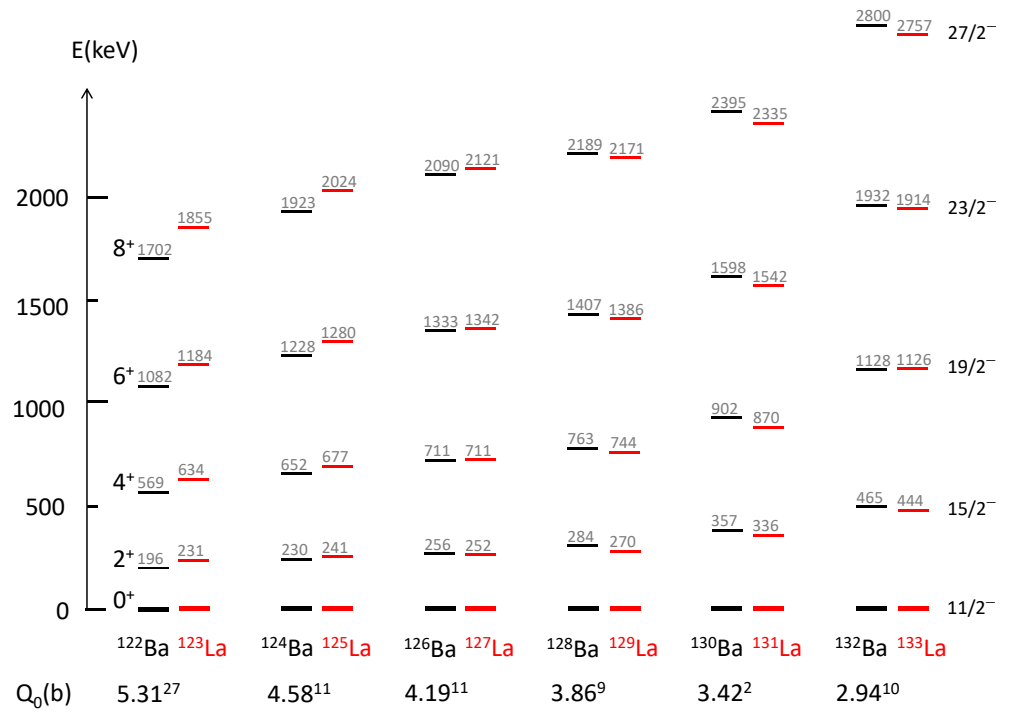


Figure 23. Energy pattern of the high-spin unique-parity states in the odd-mass lanthanum isotopes, compared to the ground-state bands of the $(A - 1)$ even-mass barium isotopes. This figure is an up-to-date view of one first proposed by Stephens et al. [105], where the term “rotation-aligned coupling scheme” was introduced.

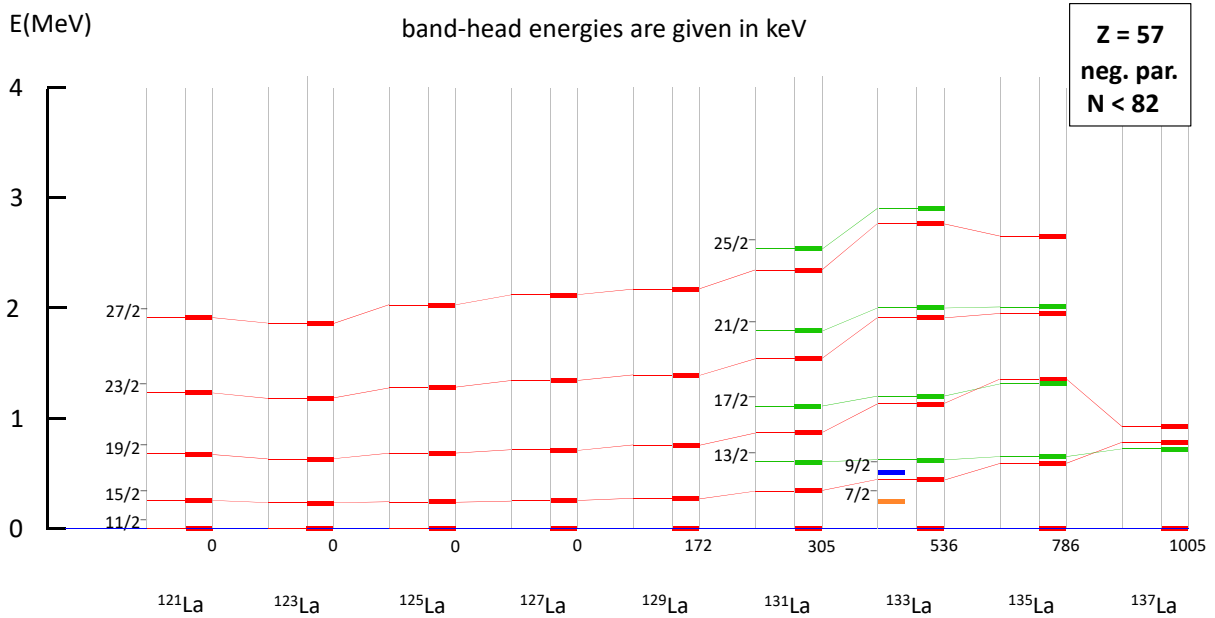


Figure 24. Systematics of unique-parity states in the odd-mass lanthanum isotopes for $N \leq 82$. Note the sparse information on low-spin states. The data are taken from ENSDF [22].

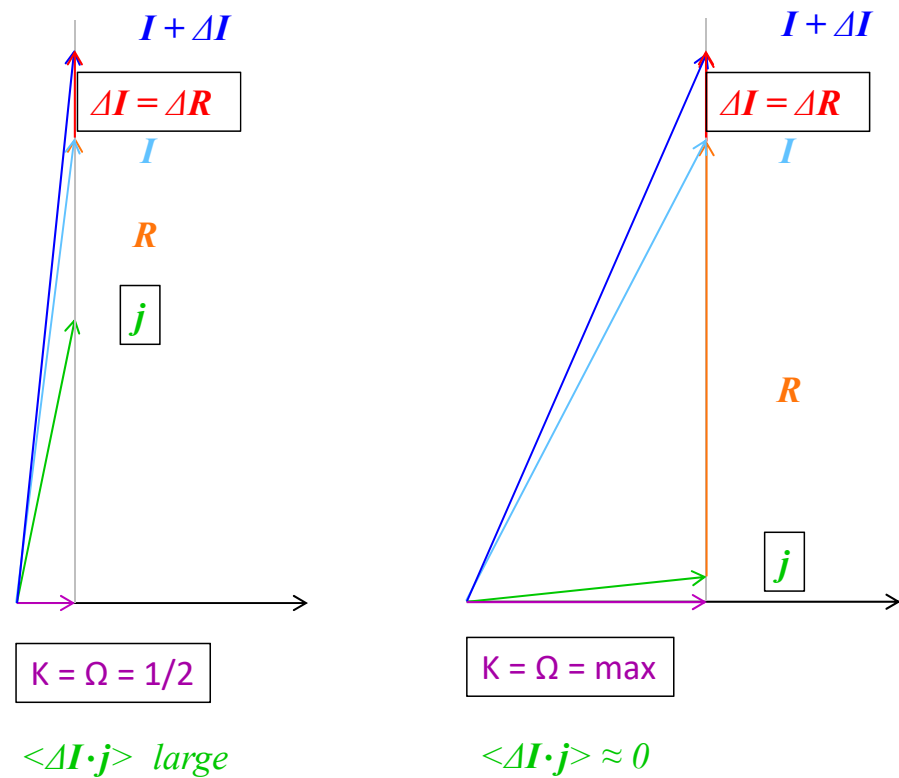


Figure 25. Semi-classical view of the rotation-alignment or Coriolis term in the particle-rotor model. The two coupling schemes depict the two extremes of the Nilsson model for a single- j state in a spheroidally deformed mean-field, labelled by $\Omega = 1/2$ and $\Omega = \max$. For the particle-rotor coupling, $I = R + j$ and very different alignments of I and j are possible. Recognizing that, e.g., Figure 23 focuses on energy differences, one sees from these diagrams that differences in I , i.e., ΔI , a vector quantity, result in very different values for $\Delta I \cdot j$ and hence for expectation values of this quantity. Reproduced from [8].

Coupling of j to an even-even core to yield low-spin states with unique parity is sparsely characterized in weakly deformed nuclei, as already noted. An extreme “weak coupling” example is shown in Figure 26. By weak coupling, one means that a set of states, resulting from coupling an odd-nucleon of spin j to the core 2_1^+ excitation, $j \otimes 2_1^+$, with spins $|j - 2| \leq J \leq |j + 2|$, appears as a closely spaced multiplet, at an excitation centred on the 2_1^+ energy of the even-even core, connected by unfragmented $E2$ strength to the spin- j ground state, is observed. This simple view is approximately realized in Figure 26: Coulomb excitation strongly populates five states with $J = 5/2, 7/2, 9/2, 11/2$, and $13/2$; it also weakly populates a $5/2^+$ state at 941 keV and a $9/2^+$ state at 1461 keV. These two states are due to a shape coexisting or intruder band (a Nilsson $1/2^+$ [431] decoupled rotational band) details of which are not important to the present focus. It is sufficient to note that the weakly coupled multiplet is identifiable, with the provision that the spin $5/2$ and $9/2$ members of the multiplet are manifested with some configuration mixing due to near degeneracies with intruder band configurations. This would suggest that the weak coupling limit is a familiar pattern, and the quest is nearly complete, pending filling in some minor details. However, a recent result [64] shows that the situation is far from being the weak-coupling limit: this is illustrated in Figure 27. Even though the energies appear to approximate the weak-coupling pattern, significant collective $E2$ strength has been “acquired” by the addition of a single extra-core proton. More specifically, the odd- A nucleus ^{129}Sb shows additional collectivity in Coulomb excitation from the ground state, above that of the ^{128}Sn core. A shell model description with effective charges of $e_p = 1.7e$ and $e_n = 0.8e$ set from the $B(E2; 0_1^+ \rightarrow 2_1^+)$ values of the semimagic neighbours ^{130}Te for protons and ^{128}Sn for neutrons, goes some way towards describing this additional collectivity. This simple

particle–core coupling situation therefore gives evidence of emerging collectivity over and above that implied by the significant effective charges associated with the individual proton and neutron contributions.

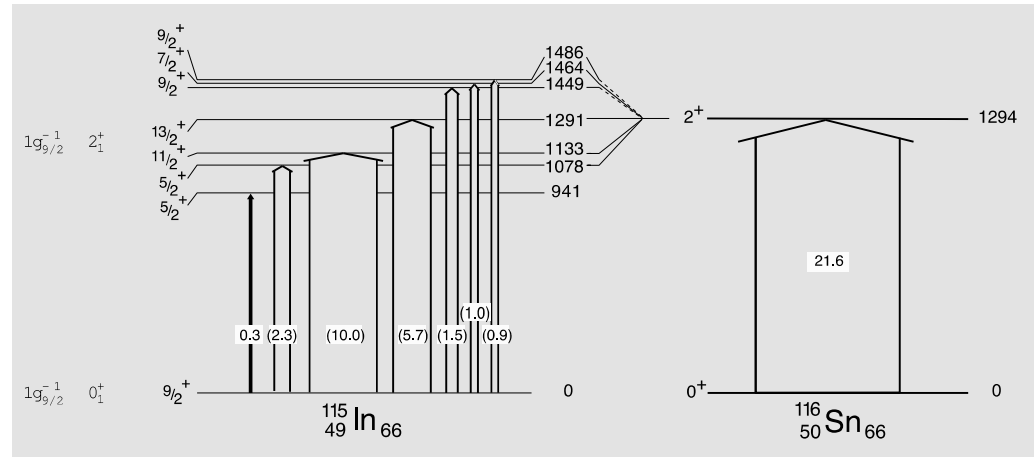


Figure 26. Example of near-weak coupling in ^{115}In , observed by Coulomb excitation and shown in comparison to Coulomb excitation for the neighbouring even-even “core” nucleus, ^{116}Sn . These states are due to the proton coupling $1g_{9/2}^{-1} \otimes 2_1^+$. There is some fragmentation of strength for specific spin-parities: this results from mixing with intruder states. The states at 941 keV, $5/2^+$ and 1449 keV, $9/2^+$ are members of a decoupled rotational band built on the $1/2^+$ [431] Nilsson configuration [106]. This configuration has $1g_{7/2}^{-1}$ parentage and results in a rotational band with decoupling parameter, $a \simeq -2$, which puts the $3/2^+$ state below the $1/2^+$ state. Note that the negative parity states are not shown; the lowest negative parity states in the odd-In isotopes are shown in Figure 28. The numbers in parentheses are $B(E2)$ values for the excitation process, in units of $e^2\text{fm}^4 \times 10^2$ ($100 e^2\text{fm}^4 = 60 \text{ W.u.}$ for $A = 115$.) The data are taken from [107]. Reproduced from [6].

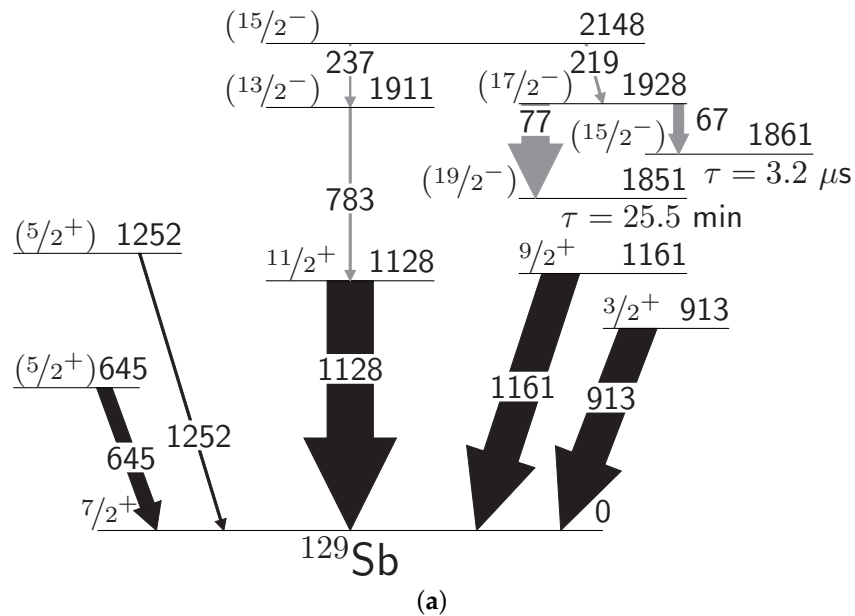


Figure 27. Cont.

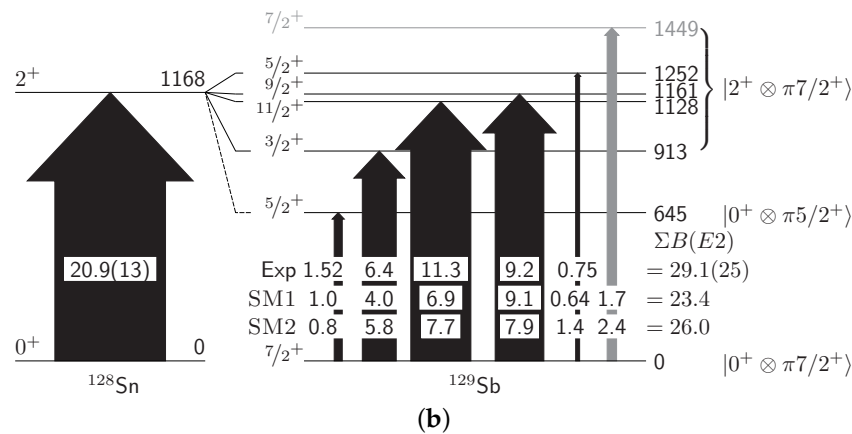


Figure 27. (a) Partial level scheme for ^{129}Sb . Grey transitions result from excitation of the 1851-keV isomer present in the beam. (b): Fragmentation of the $E2$ strength in W.u. over the $2^+ \otimes \pi 7/2^+$ multiplet members and candidate $\pi d_{5/2}$ state of ^{129}Sb and enhancement of total strength as compared to the ^{128}Sn core. The grey colored transition was not experimentally observed. The figure is reproduced from [64]. See also Ref. [64] for details of the large-basis shell model calculations SM1 and SM2, which employ the same basis space but alternative contemporary residual interactions.

The status of particle–core coupling presented above, and in additional calculations by Gray et al. [108], suggests that there is not a good understanding with respect to the $Z = 50$ closed shell and the odd-mass In and Sb isotopes. The issue extends across the entire mass surface due to a severe lack of critical data. The systematics of the low-lying states in the odd mass In and Sb isotopes are shown in Figures 28 and 29, respectively. The pattern of the In isotopes suggests that, for the negative-parity states, there may be important collective effects which would explain the energy minimum at mid shell. Weak deformation is supported by laser hyperfine spectroscopy studies [109] and is shown in Figure 30. Note that two views of deformation for the In isotopes are presented in Figure 30: a direct view via spectroscopic quadrupole moments—the lower sequence of data points centred on $\beta \sim 0.1$, and an indirect view via isotope shifts—the upper sequence of data points. The latter view can be inferred to contain a dynamical contribution, but this aspect lies beyond the present discussion. The observed pattern for the Sb isotopes suggests a “crossing” of the $2d_{5/2}$ and $1g_{7/2}$ configurations. However, at present, the question of the collectivity associated with low-lying states in the odd-Sb isotopes suggests caution is needed in making the interpretation of the lowest $5/2^+$ and $7/2^+$ states as resulting from pure shell model configurations.

Skyrme Hartree–Fock calculations with the SKX interaction [110] correctly track the nominal $2d_{5/2}$ vs. $1g_{7/2}$ level ordering in the Sb isotopes, but the location of the $3s_{1/2}$ orbit does not track with the behaviour of the observed $J = 1/2^+$ state with its shift in energy across the observed $7/2^+$ state. In the indium isotopes, the single-particle levels in the potential generated by SKX are more separated in energy and roughly track with the observed levels of the relevant spin–parity. It appears that the indium levels remain quite regular because the parent orbits are well separated in energy in the mean field and the observed states are less affected by residual interactions; however, one sees clear evidence from the quadrupole moments in Figure 30 that deformation develops at mid-shell. In contrast, the Sb isotopes have the $2d_{5/2}$ and $1g_{7/2}$ single-particle states quite close in the mean field calculation. Thus, the observed level ordering can be sensitive not only to changes in the mean field, but also to residual interactions and deformation effects.

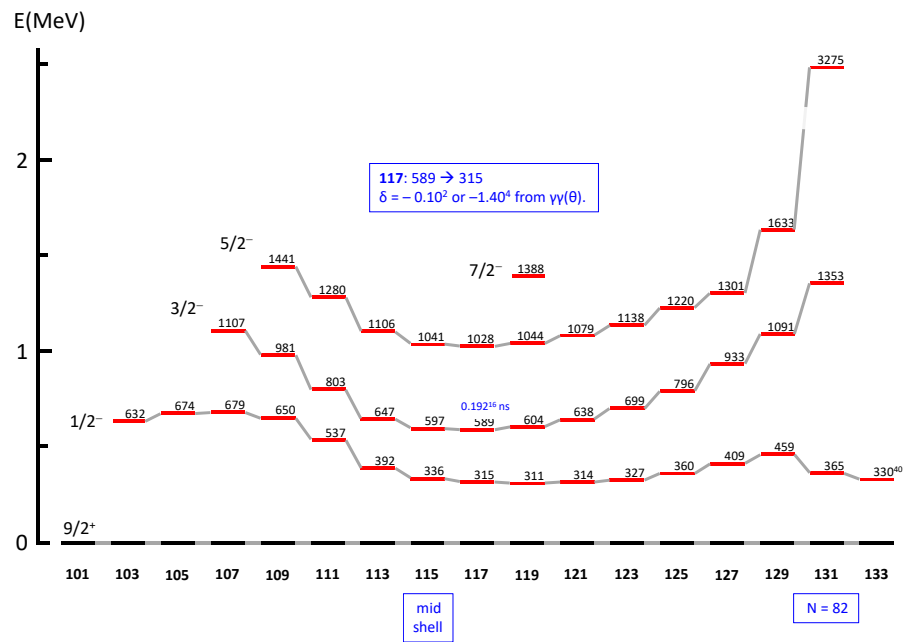


Figure 28. Systematics of the negative-parity states in the odd-mass indium isotopes relative to the $9/2^+$ ground states. Naïvely, these states could be interpreted as the shell model single proton-hole configurations $2p_{1/2}$, $2p_{3/2}$, and $1f_{5/2}$; but $E2$ transition strengths would be desirable before such an interpretation is made. The “parabolic” energy trend suggests interactions with neutrons across the shell with a characteristic energy minimum near the mid-shell point ($N = 66$), as indicated. Note the severe deficiency of data for electromagnetic decay strengths: there is one half life, for the 589 keV state in ^{117}In , and the $E2/M1$ mixing ratio for the decay of this state is ambiguous. Data for ^{107}In are from [111] and for ^{131}In are from [112]; other data are taken from ENSDF [22].

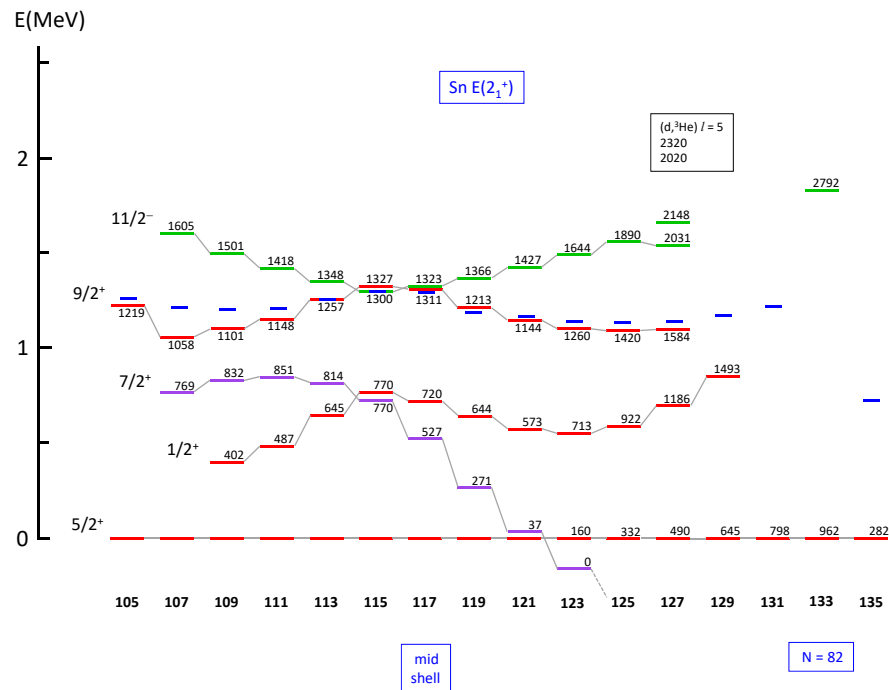


Figure 29. Systematics of selected states in the odd-mass antimony isotopes. The short blue lines show the energies of the 2_1^+ states in the even-even ^{A-1}Sn isotopes with respect to which weak coupling in the ^ASb isotopes can be assessed. The ground states of $^{125-135}\text{Sb}$ are not shown; they all have spin-parity $7/2^+$.

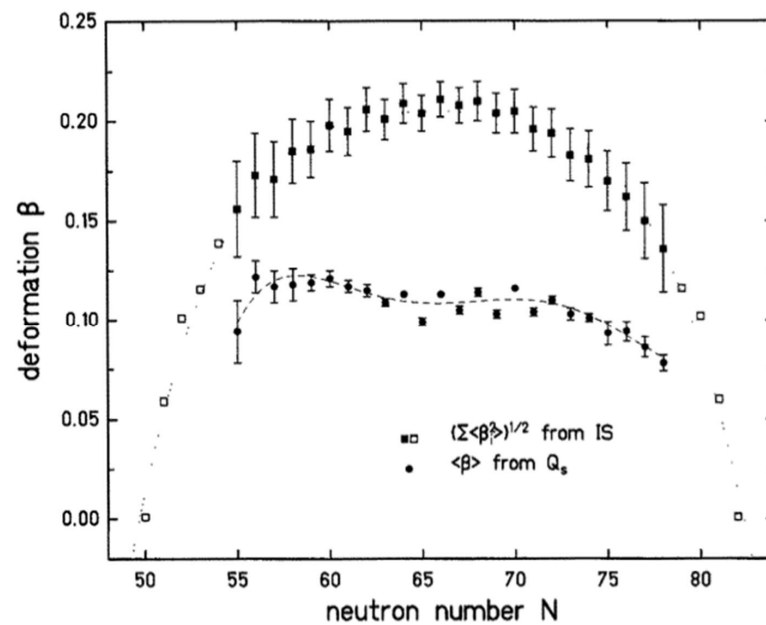


Figure 30. Deformations of the odd-In isotopes deduced from spectroscopic quadrupole moments and isotope shifts following laser hyperfine spectroscopy [109]. Reprinted from [109], Copyright (1987), with permission from Elsevier.

Mass regions where the issue of emergent collectivity needs detailed spectroscopic study are addressed in Section 5 through Section 9. In particular, Sections 5 and 6 focus on the Ni and Ca isotopes, respectively.

Let us emphasize that there is a substantial body of evidence for the role of triaxial shapes in nuclei that are of moderate deformation. This is supported by the observation of “too many low-energy states for axial symmetry” in unique-parity excitations, such as shown in Figures 20–22. It is also supported by the application of the Kumar–Cline sum rules [113,114] to shell model electromagnetic strengths, as summarized for calculations of the Bohr-model deformation parameters derived from the shape invariants for the tellurium isotopes in Figure 31. These features do not imply that $^{128-134}\text{Te}$ can be modeled as weakly deformed triaxial rotors in their low-lying states up to spin 6^+ . Scrutiny of the wave functions and predicted g factors, for example, indicates that the structures of the lowest few states are very different, despite their apparently similar shape parameters. These excitations are not rotations of a single intrinsic structure as is supposed in the triaxial rotor model. Although the magnetic moments indicate that the Te isotopes near the $N = 82$ shell closure cannot be accurately modelled as weakly deformed triaxial rotors, a triaxial rotor description may prove appropriate as the number of neutron holes increases. The fact that the excited-state shapes in Figure 31 are all triaxial with $\gamma \approx 30^\circ$ may suggest that the pathway of emerging collectivity in this region progresses from near-spherical nuclei near ^{132}Sn , to weakly-deformed triaxial rotors as an intermediate step, before finally reaching more strongly deformed prolate rotors near mid-shell. Further data and calculations across an extended range of Te and Xe isotopes would help to assess this conjecture.

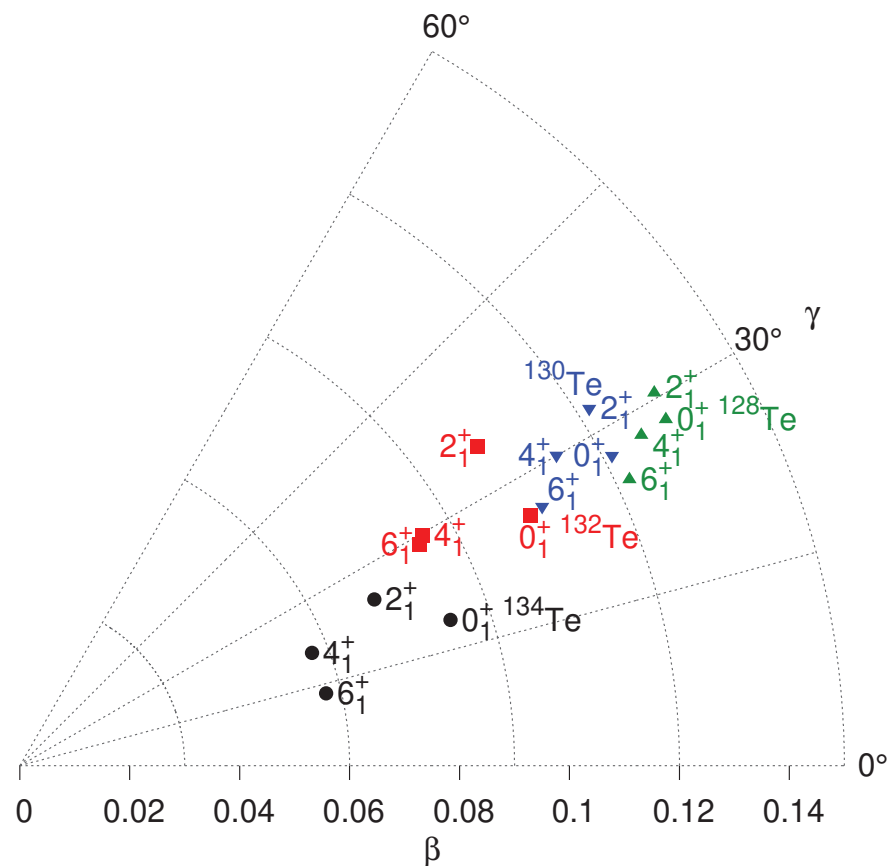


Figure 31. Average Bohr-model deformation parameters for yrast states in $^{128,130,132,134}\text{Te}$, assuming an ellipsoidal deformed nucleus and determined from shell-model calculations using the Kumar–Cline sum rules. For clarity, the fluctuations are not plotted. They are similar in magnitude for all cases, and by happenstance, the “softness” or fluctuation associated with each point is comparable to the scatter in the plotted points. Reproduced from [115].

5. Emergent Collectivity in the Nickel Isotopes

Currently, there is a high interest in neutron-rich nuclei. This is because of unprecedented access to completely new mass regions, and soon to come facilities that may “reach” even further. In particular, the neutron-rich Ni isotopes and the adjacent open-shell isotopes have received much attention. The systematic features of the low-energy excited states in the even-mass Ni isotopes are shown in Figures 32 and 33. A naïve interpretation of $^{58-66}\text{Ni}$ (Figure 32) is that they are vibrational; however, the error of using only energies to make structural interpretations of weakly deformed nuclei has now been substantially demonstrated [116]. The structure of $^{58-66}\text{Ni}$ is addressed in detail in this Section, with attention to seniority and shape coexistence. An unequivocal interpretation of $^{70-76}\text{Ni}$ (Figure 33) is that these isotopes are dominated by seniority coupling. However, this is an incomplete view, as details in Figure 33 imply; the structure of $^{70-76}\text{Ni}$ is also addressed in detail in this Section.

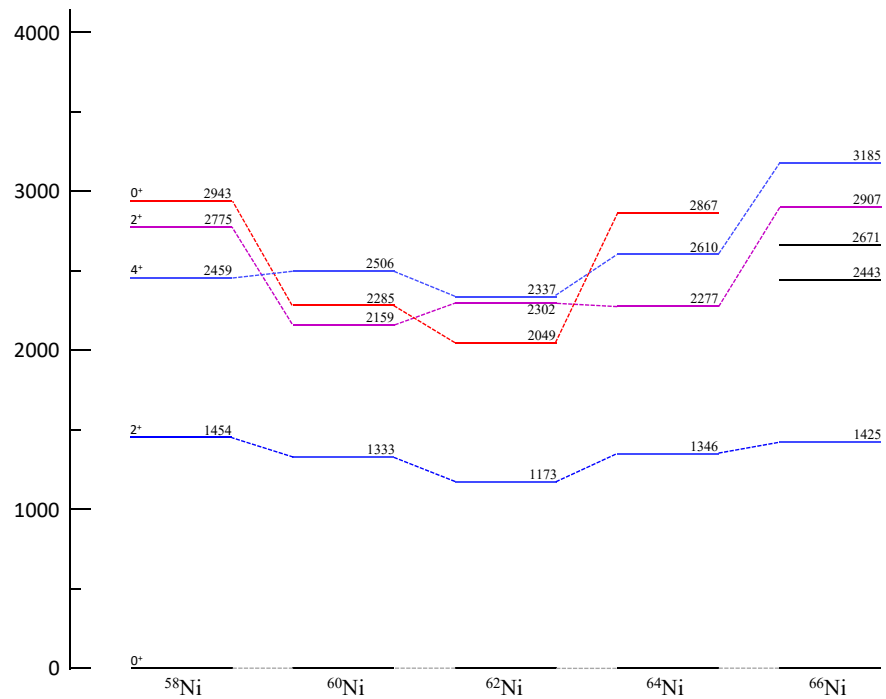


Figure 32. Systematics of the states with spin 0, 2, 4 and positive parity in $^{58-66}\text{Ni}$. The states in ^{66}Ni at 2443 and 2671 keV are assigned spin-parity 0^+ and are taken from [117]; other data are taken from ENSDF [22].

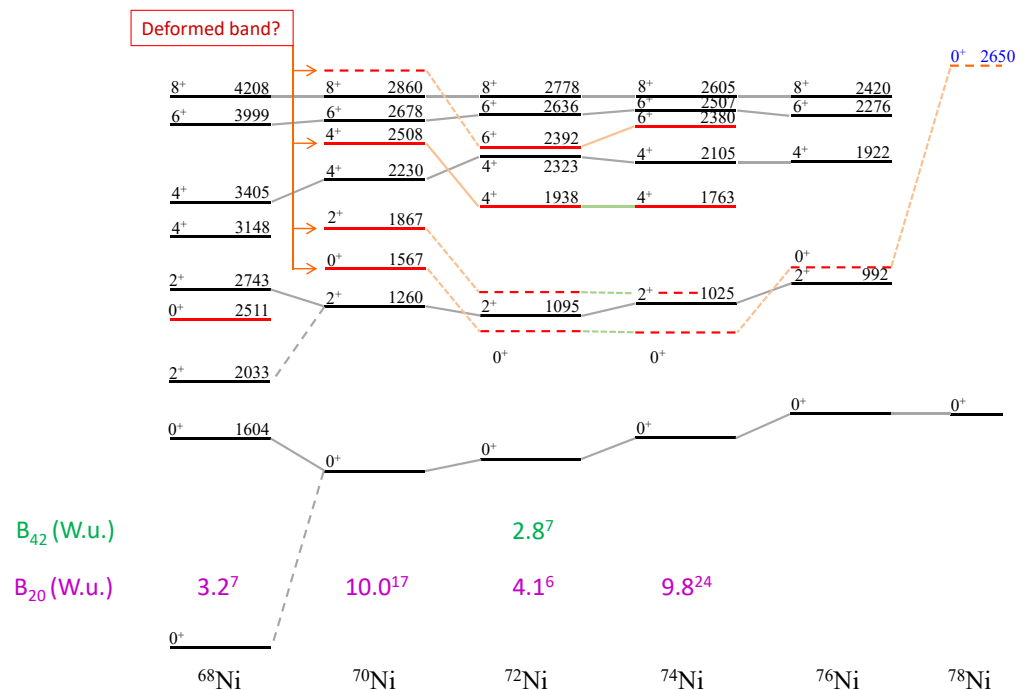


Figure 33. Systematics of the lowest positive-parity excited states in $^{68-78}\text{Ni}$. Data are taken from: [118,119] (^{68}Ni); [120–122] (^{70}Ni); [123] (^{72}Ni); [124] (^{74}Ni); [125] (^{76}Ni). The $B(E2)$ data are from ENSDF [22] for $^{68,70}\text{Ni}$, from [126] for ^{72}Ni and from [127] for ^{74}Ni . The dashed red lines are a conjecture regarding the possibility of deformed intruder bands based on the interpretation of 2^+_2 and 4^+_2 states being members of such bands, and would be consistent with the interpretation of such a structure in ^{70}Ni , suggested by Chiara et al. [122]; they are interpreted as seniority-four states by Morales et al. [124].

Recently, a study of conversion electrons following (p, p') excitation of $^{58,60,62}\text{Ni}$ was made by Evitts et al. [128,129]. A notable result was the observation of strong $E0$ decay branches from second-excited 2^+ states to the first-excited 2^+ states. The details for ^{62}Ni are shown in Figure 34. Previously, strong $E0$ decays had been established for a series of excited 0^+ states in $^{58,60,62}\text{Ni}$ [130]. However, an unresolved puzzle was that, whereas this strength was associated with proton-pair excitations in $^{58,60}\text{Ni}$, this was not the situation in ^{62}Ni . The paper of Evitts et al. [128,129] points to a possible resolution: Figure 34 suggests that the 0^+_2 state at 2049 keV is the head of a strongly deformed band and the 2302-keV 2^+ state is the first-excited band member. The proton pair-excitation at 3524 keV is shown. Our interpretation of the 2049 keV 0^+ state in ^{62}Ni is a “4p-4h” excitation of the ^{56}Ni core. Such a structure would not be populated in $(^3\text{He}, n)$, $(^{16}\text{O}, ^{14}\text{C})$, $(^6\text{Li}, d)$ or $(^{16}\text{O}, ^{12}\text{C})$ reactions, which were the spectroscopic probes used to identify the proton-pair excitations in $^{58,60,62}\text{Ni}$ [131–134].

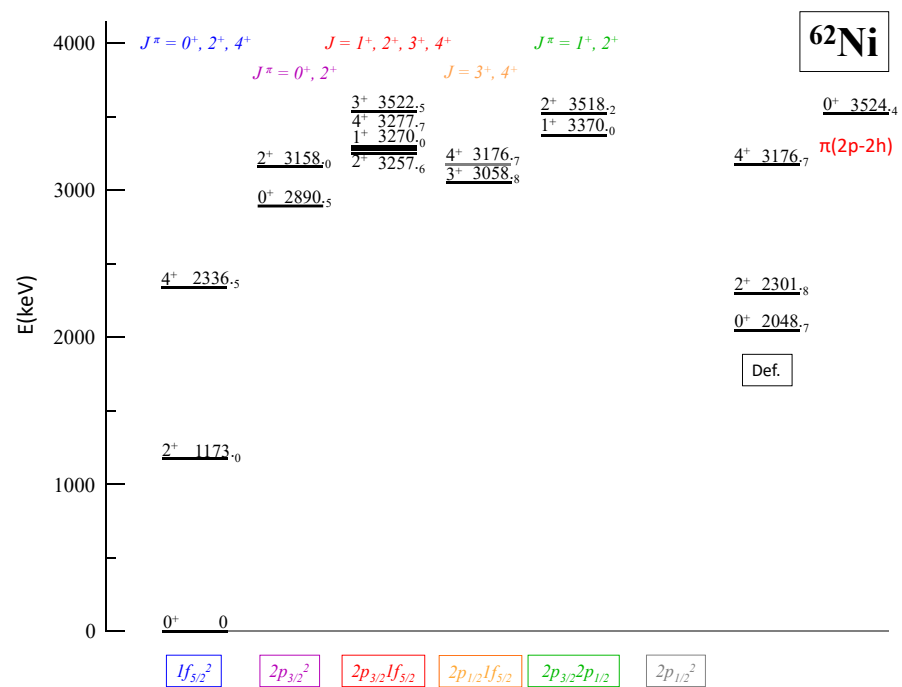


Figure 34. Organization of the lowest excited states in ^{62}Ni into seniority-dominated structures and a new strongly deformed band. At present, this view must be considered a conjecture. The proposed seniority-two structures are labelled by the shell model configurations with their associated spins and parities. The deformed band is discussed in the text. The 0^+ state at 3524 keV is assigned as a proton-pair excitation based on two-proton [134] and α [132] transfer reaction spectroscopic studies.

The seniority-dominated structure of $^{70,72,74,76}\text{Ni}$ has an unusual complication. While it is simple in ^{76}Ni , as established by direct observation of a cascade of four gamma rays from an isomer with half-life 590 ns [125], this isomerism has disappeared in the lighter even-mass nickel isotopes. The situation is now resolved at the level of the multiple decay branches from the candidate spin-parity 8^+ states characteristic of a $(j = 9/2)^2$ seniority, $v = 2$ multiplet; but an open question is the nature of the low-lying states that facilitate these “fast” decays. Two possibilities exist: the “extra” states are seniority four, $v = 4$ states or, the “extra” states are members of coexisting deformed bands. It is possible for $v = 4$ states to appear lower in energy than $v = 2$ states in the manner manifested in $^{72,74}\text{Ni}$ [124]. It is also plausible that shape coexistence is occurring at low energy in these nuclei. In favor of the latter interpretation is that shape coexistence has been suggested to occur at low energy in ^{70}Ni [121,122]. Furthermore, a near identical structure in the $N = 50$ isotones involving the proton $1g_{9/2}$ subshell exhibits robust seniority isomerism

with no involvement of $v = 4$ states producing fast decays (see, e.g., [135], although one has to note seniority breakdown at low spin inferred from lifetime measurements [136]).

6. Collectivity in the Calcium Isotopes

The calcium isotopes hold a unique position in the study of nuclear structure. With $Z = 20$ and a reach to either side of $N = 20$ and 28, they should be a perfect illustration of closed-shell behaviour in nuclei, except that they are not. Figures 1 and 2 open the focus of this contribution, with a perspective on ^{40}Ca as an $N = Z$ doubly closed-shell nucleus and on ^{48}Ca as an $N > Z$ doubly closed-shell nucleus: ^{48}Ca conforms to expectations; ^{40}Ca does not. Indeed, recently, the time-honored view that closed shells only occur at 2, 8, 20, 28, 50, 82, 126 has been questioned due to unusual systematic features in $^{52,54}\text{Ca}$: this is of high interest with respect to forthcoming prospects for new facilities which will provide access to very neutron-rich nuclei, and the calcium isotopes in particular. (The current “reach” into the neutron-rich calcium isotopes is two events in 39 h of beam time, assigned to ^{60}Ca [137]).

A highly attractive feature of the calcium isotopes between $N = 20$ and 28 is that they should be dominated by a single j shell, the $1f_{7/2}$ shell. Figure 35 shows data that support this view. The $j = 7/2$ seniority $v = 2$ states ($J = 2, 4, 6$) are highlighted in red; the $j = 7/2$ seniority $v = 4$ states ($J = 2, 4, 5, 8$) in ^{44}Ca are highlighted in orange. Note that the $J = 4, v = 4$ configuration mixes with the $J = 4, v = 2$ configuration. Further note that the $J = 5$ state has not been observed. Figure 35 also shows that other states appear at low energy in $^{42,44,46}\text{Ca}$: these are discussed with reference to the following, Figures 36–40 and Table 5.

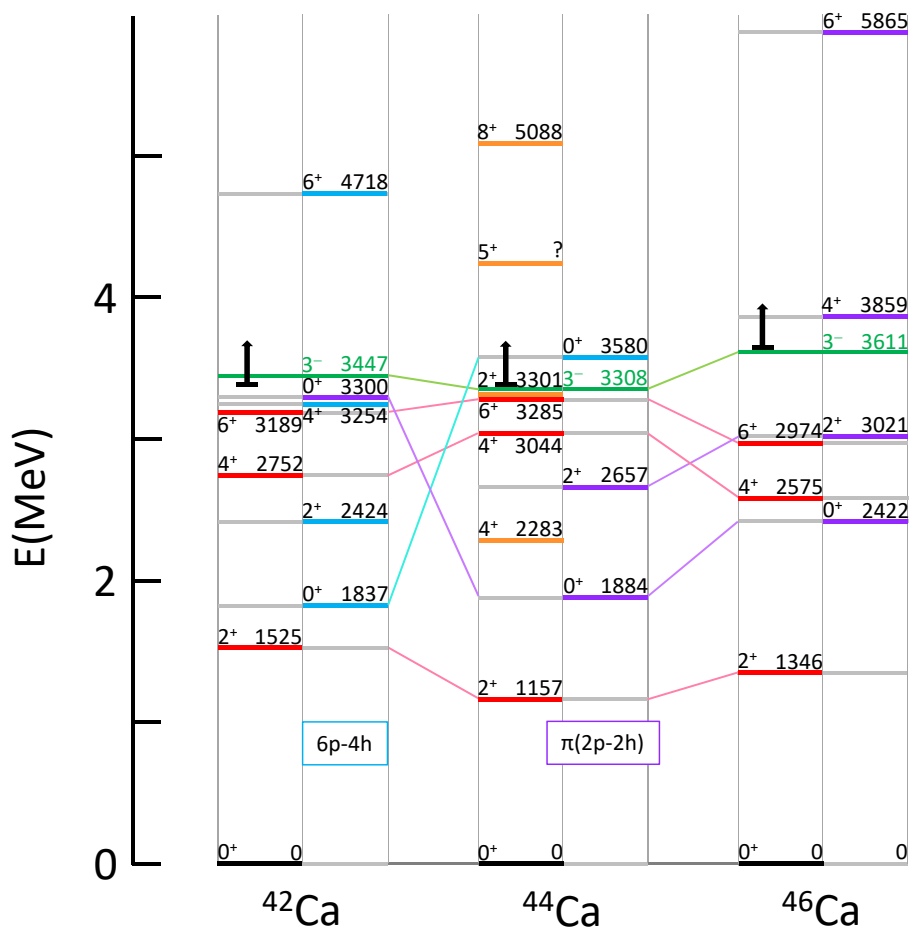


Figure 35. Seniority and shape coexistence view of $^{42-46}\text{Ca}$. Data for ^{46}Ca include recent results of Pore et al. [138] and Ash et al. [139]. The deformed band in ^{42}Ca (shown in blue) is observed up to

spin 12 [140]. The deformed bands in ^{44}Ca and ^{46}Ca are indicated in purple. The seniority-two states are indicated in red (but see details below in this caption); the seniority-four states, unique to ^{44}Ca , are indicated in orange (but, again, see details below in this caption). The distinction between the deformed bands is based on multi-nucleon transfer reactions: see Table 5. The seniority-2 and seniority-4 structures in ^{44}Ca , the 4^+ states at 2.28 and 3.04 MeV, and the 2^+ states at 1.16, 2.66 and (probably) 3.30 MeV are mixed; see [141]. For the seniority structures associated with the $\nu 1f_{7/2}$ configuration, see Figure 3. Note that, while there is a high-spin study of ^{44}Ca (Lach et al. [142]), the deformed band has not been characterized. For a complementary perspective of the calcium isotopes, see also details in Figures 36 and 41. The 3^- states, which are not part of the present discussion, are shown in green. Horizontal bars with vertical arrows indicate excitation energies above which states are omitted.

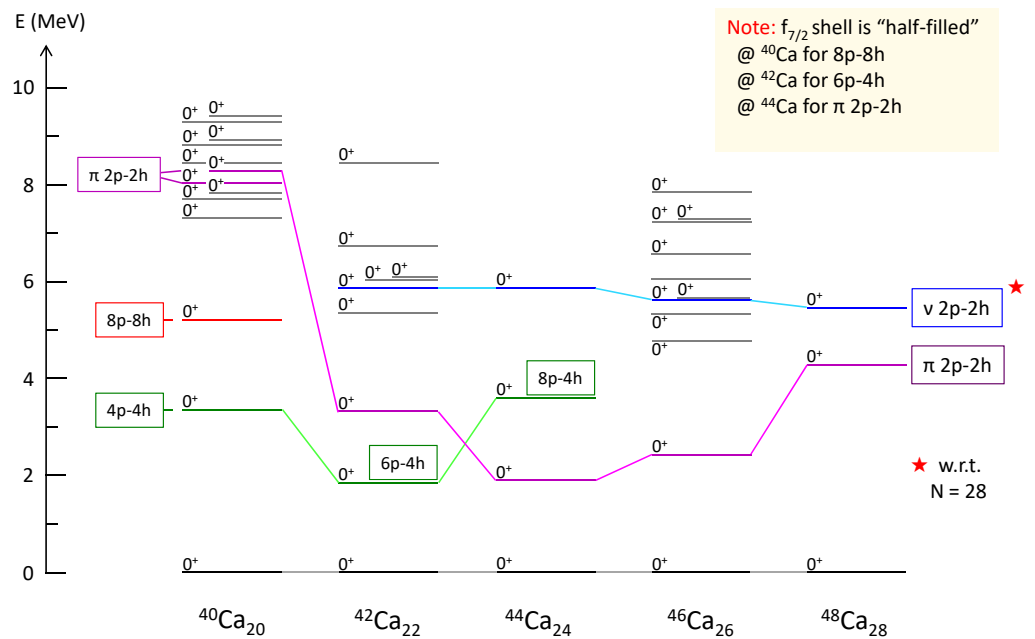


Figure 36. Excited 0^+ states in $^{40-48}\text{Ca}$. All known 0^+ states up to 10 MeV are shown. Assignments to particle-hole configurations are indicated where known and further details are given in Figure 35 and 37, and Table 5. Note the inset box which indicates when the $\nu 1f_{7/2}$ shell is half filled. Further note that the $\nu 2p - 2h$ configurations are with respect to $N = 28$, and are identified by the neutron-pair-addition reaction (t,p).

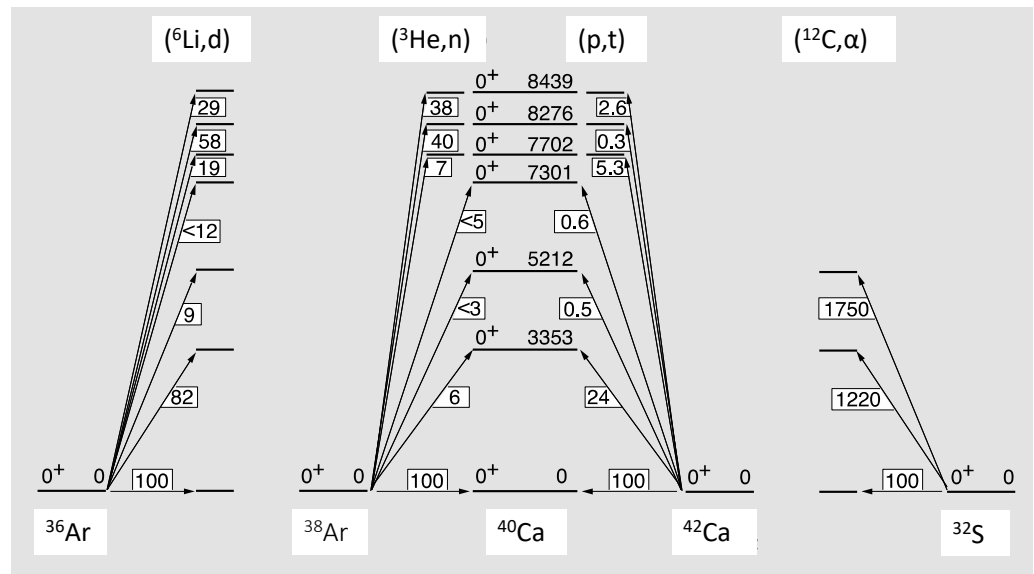


Figure 37. Excited 0^+ states in ^{40}Ca viewed from the perspective of multiparticle transfer reactions. The first excited 0^+ state at 3353 keV is usually labelled as “4p-4h” on the basis of its strong population in the $^{36}\text{Ar}(^6\text{Li}, d)$ reaction, but note the strong population of 0^+ states, particularly around 8.3 MeV. The second excited 0^+ state at 5212 keV is usually labelled as “8p-8h” on the basis of its strong population in the $^{32}\text{S}(^{12}\text{C}, \alpha)$ reaction (the population of the 3353 keV state could involve partial filling of the hole states in ^{32}S , and does not necessarily imply an 8p-8h admixture to the 3353 keV state). Figure 1 depicts the deformed and superdeformed bands built on the 3353 and 5212 keV states, respectively. Proton-pair configurations appear to dominate 0^+ states around 8 MeV, as supported by the $^{38}\text{Ar}(^3\text{He}, n)^{40}\text{Ca}$ reaction. Based on the $^{42}\text{Ca}(p, t)^{40}\text{Ca}$ reaction, neutron-pair configurations do not dominate below 8.5 MeV. This leaves the 7301 keV excited 0^+ state as the leading structure of interest for an interpretation: possibly it is a “6p-6h” state (cf. Figure 40). Taken from [6].

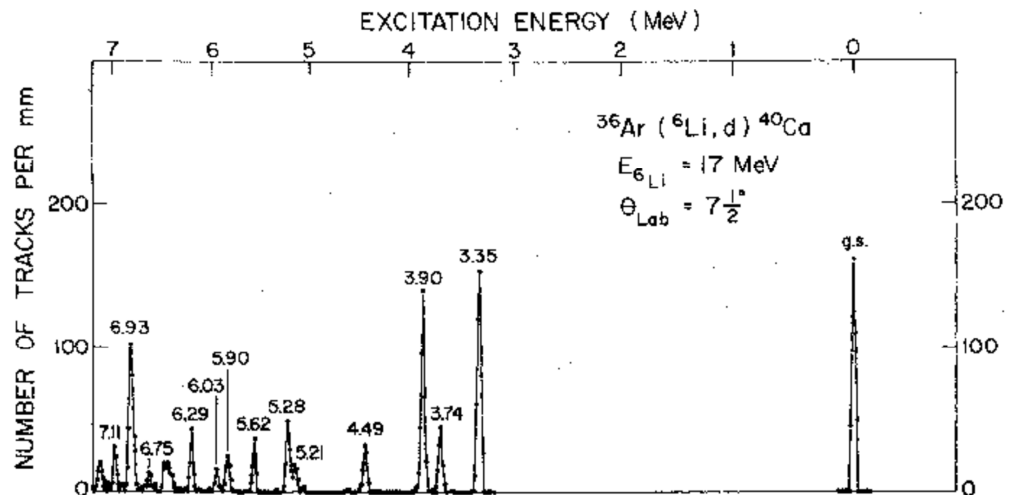


Figure 38. Spectrum of deuterons following the reaction $(^6\text{Li}, d)$ on a ^{36}Ar target. The most strongly populated excited states are members of the deformed band with $E_x (J^\pi)$: 3353 (0^+), 3904 (2^+), 5279 (4^+), 6930 (6^+), cf. Figure 1. Note that the peaks at 5.28 and 6.93 MeV are multiplets. Reprinted with permission from [143]. Copyright (1979) by the American Physical Society.

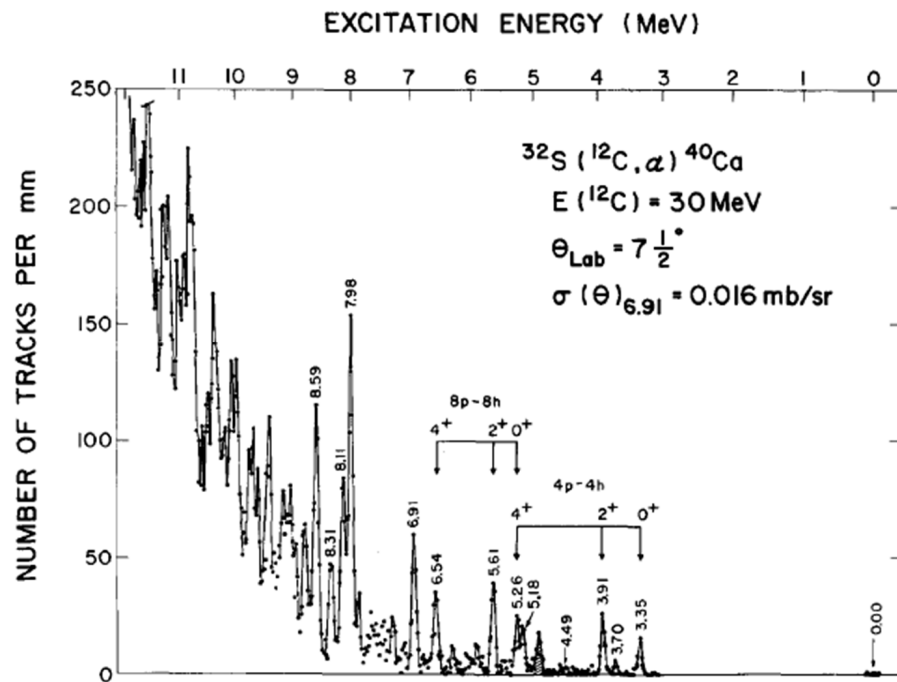


Figure 39. Spectrum of alphas following the reaction $(^{12}\text{C}, \alpha)$ on a ^{32}S target. States in both the 4p-4h and the 8p-8h deformed bands are populated. The population of the 4p-4h band may involve a partial filling of the “eight holes” in the target. Reprinted from [144], Copyright (1972), with permission from Elsevier.

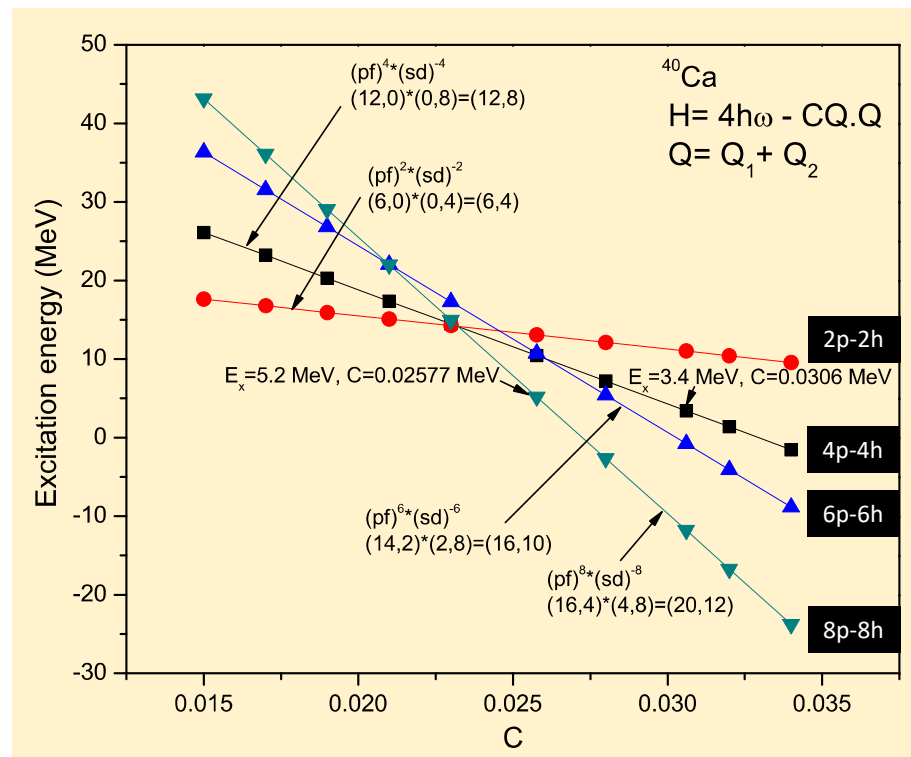


Figure 40. Estimate of the multiparticle-multihole basis state energies for ^{40}Ca using a schematic $su(3)_{\text{particle}} \otimes su(3)_{\text{hole}}$ model with a $Q \cdot Q$ interaction of strength C , where $Q = Q_1 + Q_2$ and Q_1 and Q_2 act on the $N_p (\lambda_1, \mu_1)$ and $N_h (\lambda_2, \mu_2)$, pf and sd irreps, respectively. The figure is from a collaboration between one of us (JLW) and the late David Rowe.

Table 5. Tabulation of multi-nucleon transfer reaction spectroscopic data that provide (limited) information on the multiparticle-multihole structures of excited 0^+ states in $^{42,44,46}\text{Ca}$. The terms “strong” and “weak” refer to strengths of population of states in these transfer reactions. Note that the inference of “particle” and “hole” structure depends on the transfer nucleons and the target configuration with respect to closed shells.

	0_1^+	0_2^+	0_3^+	0_4^+	0_5^+	0_6^+	reference
^{42}Ca							
E_x (MeV):	0.00	1.84 ^a	3.30 ^b	5.35	5.86 ^c	6.02	
$^{40}\text{Ca}(t,p)^{42}\text{Ca}$					strong		[145]
$^{40}\text{Ar}(^3\text{He},n)^{42}\text{Ca}$		weak					[146]
$^{38}\text{Ar}(^6\text{Li},d)^{42}\text{Ca}$			strong				[147]
^{44}Ca							
E_x (MeV):	0.00	1.88 ^b	3.58 ^a	5.86 ^c			
$^{48}\text{Ti}(d,^6\text{Li})^{44}\text{Ca}$			strong				[148]
$^{46}\text{Ti}(^{14}\text{C},^{16}\text{O})^{44}\text{Ca}$		strong					[149]
$^{42}\text{Ca}(t,p)^{44}\text{Ca}$				strong			[145]
^{46}Ca							
E_x (MeV):	0.00	2.42 ^b	4.76	5.32	5.60 ^c	5.63 ^c	
$^{48}\text{Ti}(^{14}\text{C},^{16}\text{O})^{46}\text{Ca}$		strong					[149]
$^{44}\text{Ca}(t,p)^{46}\text{Ca}$					strong	strong	[145]

^a $4p - 4h \otimes v1f_{7/2}$, ^b $\pi(2p - 2h)$, ^c $v(2p - 2h)$.

Figure 36 shows the problem of the simple $1f_{7/2}$ shell-based view of $^{42,44,46}\text{Ca}$: there are “too many 0^+ states” at low energy in the even-mass calcium isotopes. A single-shell-seniority view does not possess any excited 0^+ states; but the second excited state in $^{42,44,46}\text{Ca}$ is a 0^+ state. Furthermore, the first-excited 0^+ states in $^{42,44,46}\text{Ca}$ are not configurations due to a common origin. The evidence for this is presented in the following paragraphs.

The key to the structure of the calcium isotopes with $N = 20 - 28$ is manifested in multi-nucleon transfer reaction spectroscopy for ^{40}Ca , summarized in Figure 37. The details are complex and counterintuitive. Indeed, the evidence “has to be seen to be believed”; Figures 38 and 39 show the evidence. It is important to recognize the role of the target nuclei in that they define “hole” structures with respect to which the transferred multi-nucleon “clusters” are “added”. Added nucleons can completely fill the holes (ground-state population), or partially fill the holes, or not fill the holes at all. There is a dominance of transfer to states that involve the target holes remaining completely unfilled, i.e., a $4p-4h$ configuration in the $(^6\text{Li},d)$ reaction and an $8p-8h$ configuration in the $(^{12}\text{C},\alpha)$ reaction. Note that the $(^6\text{Li},d)$ reaction does not populate the states of the “ $8p-8h$ ” band strongly, but band mixing is suggested. Further note that the $(^{12}\text{C},\alpha)$ reaction can populate the states of the “ $4p-4h$ ” band by “partially filling” the holes.

A partial guide to the multiparticle-multihole structure of $^{42,44,46}\text{Ca}$ is presented in Table 5. This view is only partial because of a lack of stable isotope targets. The view leaves open many questions, but overriding all questions is the clear view that the shell model, as a simple model view, catastrophically breaks down in these isotopes. A guide to a likely interpretation is provided by the schematic-model view presented in Figure 40. This treats particle “clusters” and hole “clusters” as distinct entities that interact. This is tractable using an $su(3)$ algebra with a quadrupole–quadrupole, $Q \cdot Q$ interaction (see [150,151] for details). This schematic view suggests a viable “coupling scheme”, which serves much like the Nilsson scheme serves in nuclei with deformed ground states, but here serving to handle multiparticle-multihole excitations at low energy in the calcium isotopes.

Figure 40 reveals the enormous energy shifts associated with interactions that produce nuclear deformation. In Figure 1, $B(E2)$ values in association with the deformed bands in ^{40}Ca are given: if the $B(E2; 4^+ \rightarrow 2^+)$ strength of 170 W.u. (in the 8p-8h band) is scaled to $A = 172$ ($A^{4/3}$ dependence), it has a strength of 1200 W.u., cf. the $4^+ \rightarrow 2^+$ transition in the ground-state band of ^{172}Yb , where the strength is 300 W.u. Note that the structural interpretations of the deformed bands in ^{40}Ca are not model based; they are mandated by the transfer reaction data shown in Figures 38 and 39. Most importantly, Figure 40 and specifically the interaction strength of the quadrupole-quadrupole interaction, C , illustrates how configurations that are spread over ~ 90 MeV in a spherical mean-field, i.e., $8\hbar\omega$, can appear almost degenerate in energy. Indeed, it is worthy of comment that Nature could be said to have “barely realized a spherical ground state for ^{40}Ca ” (as also for ^{16}O). In the spirit of “islands of inversion”, there is a veritable archipelago of islands of inversion, multiple inversions, within one-oscillator shell of excitation energy in ^{40}Ca . Unfortunately, detailed spectroscopy of multiparticle-multihole states in nuclei is confined to this local mass region. A few more details are given before closing this Section.

Let us make some further comments on Figure 40. Just as one arrives at a shell model basis using an oscillator potential with spin-orbit coupling (and further, by deforming the oscillator potential, as a Nilsson model basis), so in Figure 40 one arrives at a multi-shell basis. The justification of invoking this basis is the observation of the 4p-4h and 8p-8h states in ^{40}Ca at 3.5 and 5.2 MeV, respectively. The excitations of the 2p-2h and 6p-6h states in ^{40}Ca are not characterized, but there are many 0^+ excited states known above 7 MeV, as presented in Figure 37. Note that a 5% change in the interaction strength corresponds to a 5 MeV shift in energy at $C = 0.025$ for the 8p-8h configuration. From this perspective, the very existence of a shell model description of nuclei is a “just-so” story, i.e., for a small change in this $su(3)$ -model interaction, spherical states in nuclei would have only been encountered as rare, exotic excitations. An example of this is realized in ^{44}Ti , as depicted in Figure 43. Details behind these schematic estimates are given in [150–152] (see also [153,154]).

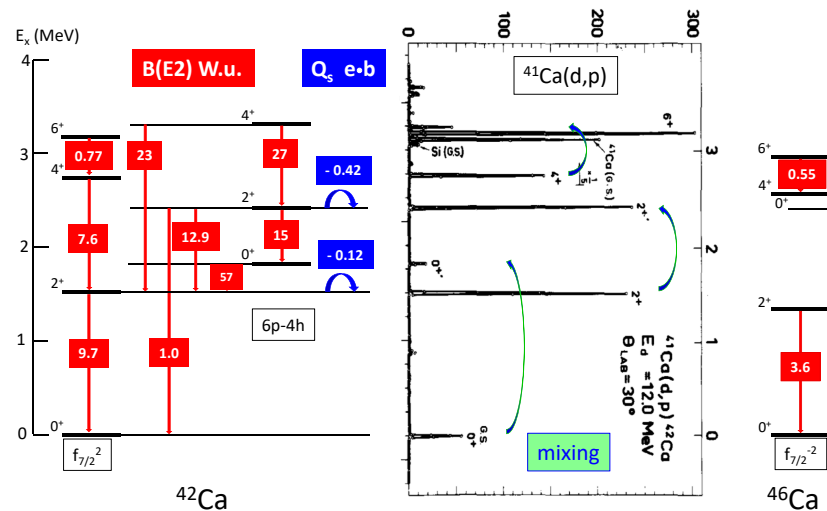
A useful spectroscopic view of the persistence of multiparticle-multihole excitations in this mass region is provided by ^{42}Ca . This nuclide is accessible to transfer reaction spectroscopy and to Coulomb excitation. A view which combines such spectroscopic data is presented in Figure 41. Figure 42 shows a simple view of the structure using “two-state mixing”, applied to the lowest states with spins 0, 2, and 4; this description should be compared with shell model and collective model views summarized in Table 6. An important point to note is that, while these coexisting configurations mix, the mixing is sufficiently weak that the underlying dominant structures can be identified: they are a spherical (valence) neutron particle pair and a “6p-4h” structure resulting from the ^{40}Ca core 4p-4h structure, cf. Figure 37.

The description presented in Figure 42 correctly reproduces the largest $E2$ transition strength, that between the 2_1^+ and 0_2^+ states, i.e., this strength is entirely due to mixing with zero contribution from intrinsic strength. The description fails for the $E2$ transition strength between the 2_2^+ and 0_1^+ states, and there is a serious failure for the diagonal matrix elements of the 2_1^+ and 2_2^+ states. The conclusion is that two-state mixing for spin 2 is inadequate: three (four)-state mixing is necessary. Experimentally, third and fourth 2^+ states are known at 3392 and 3654 keV (cf. ENSDF [22]); both are populated in the one-neutron addition reaction: spectroscopic characterization of these states is lacking.

Table 6. Comparison of $E2$ matrix elements in ^{42}Ca with shell model (SM) and beyond mean-field (BMF) calculations. The differences between theory (th) and experiment (ex) are shown as $[(\langle E2 \rangle_{\text{ex}} - \langle E2 \rangle_{\text{th}}) / \langle E2 \rangle_{\text{ex}}] \times 100\%$. Details of these calculations are given in [155]: the shell model calculations follow details similar to those employed in [156]. Comparison of the two-state mixing results, shown in Figure 42, suggests serious deficiencies in these two models, which are state of the art. Note that all three calculations obtain an incorrect sign for the $2_2^+ \rightarrow 0_1^+$ $E2$ matrix element, and they all seriously fail for the diagonal matrix elements. Adapted from [155].

$I_i \rightarrow I_f$	$\langle I_i E2 I_f \rangle e \text{ fm}^2$			% Difference	
	Experiment	SM	BMF	SM	BMF
$2_1^+ \rightarrow 0_1^+$	20.5 ± 0.6	11.5	9.14	78	124
$4_1^+ \rightarrow 2_1^+$	24.3 ± 1.2	11.3	12.2	115	99
$6_1^+ \rightarrow 4_1^+$	9.3 ± 0.2	8.2	14.3		
$0_2^+ \rightarrow 2_1^+$	22.2 ± 1.1	11.9	6.1	87	264
$2_2^+ \rightarrow 0_1^+$	-6.4 ± 0.3	9.4	4.4	32 ^a	45 ^a
$2_2^+ \rightarrow 2_1^+$	$-23.7^{+2.3}_{-2.7}$	-13.6	-7.7	74	208
$4_2^+ \rightarrow 2_1^+$	42^{+3}_{-4}	21.9	10.1	92	316
$2_2^+ \rightarrow 0_2^+$	26^{+5}_{-3}	32	42	19	38
$4_2^+ \rightarrow 2_2^+$	46^{+3}_{-6}	52	70	12	34
$2_1^+ \rightarrow 2_1^+$	-16^{+9}_{-3}	-4.3	0.1		
$2_2^+ \rightarrow 2_2^+$	-55 ± 15	-31	-42		

^a Wrong sign.



C. Ellegaard et al. PL B40 641 1972

Figure 41. Two key spectroscopic views of ^{42}Ca and a comparison with ^{46}Ca . On the left, the lowest positive-parity states are shown together with the $E2$ transition strengths in W.u. between these states and diagonal values for the $E2$ matrix elements in eb of the 2_1^+ and 2_2^+ states, as determined by Coulomb excitation [155]. In the centre of the figure, the population of these states by the $^{41}\text{Ca}(d,p)^{42}\text{Ca}$ reaction is shown (the spectrum is reproduced from [157], Copyright (1972), with permission from Elsevier.). This reaction should only populate the 0^+ ground state and one each for states of spin-parity 2^+ , 4^+ , and 6^+ corresponding to a seniority $v = 2$ multiplet in association with the expected $1f_{7/2}$ orbital, which is the only shell model subshell for $20 < N < 28$: these data provide evidence that there is mixing between these seniority configurations and other structure which is intruding to low energy. On the right, for comparison, the lowest positive-parity states in ^{46}Ca together with known $E2$ transition strengths are shown. In addition to cited sources, data are taken from ENSDF [22].

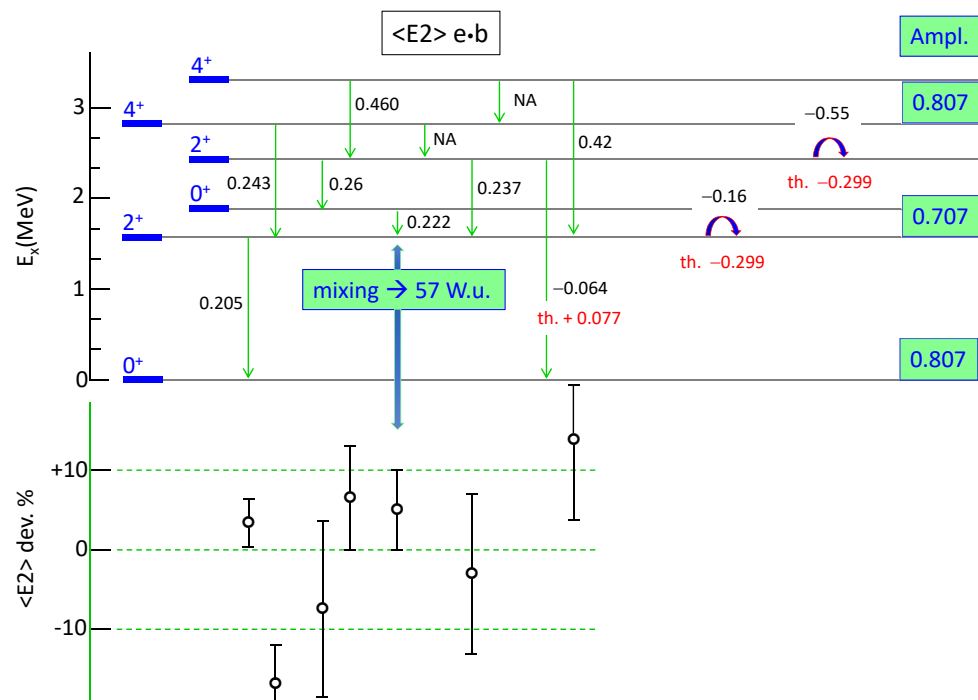


Figure 42. Two-state mixing for the lowest pairs of states with spin–parity 0^+ , 2^+ , and 4^+ in ^{42}Ca . The $E2$ matrix elements are shown for transitions and level quadrupole moments. The mixing amplitudes are fixed from the fragmentation of the one-neutron addition spectroscopy shown in Figure 41, viz. 0.807 in the ground state, 0.707 in the 2_1^+ state and 0.807 in the 4_1^+ for the $1f_{7/2}$ components of these states. There are two fitted parameters: $Q_0 = 10 e \text{ fm}^2$ for the $1f_{7/2}$ configurations and $Q_0 = 40 e \text{ fm}^2$ for the intruder configurations. The Q_0 value for intruder configurations is multiplied by a rotor model Clebsch–Gordan coefficient for the respective spin values, i.e., $-1.195Q_0$ for $\langle 2_1 || E2 || 2_1 \rangle$ and $1.604Q_0$ for $\langle 4_1 || E2 || 2_1 \rangle$. Differences between theory (th) and experiment (ex) are shown in the lower part of the figure as $[(\langle E2 \rangle_{\text{ex}} - \langle E2 \rangle_{\text{th}}) / \langle E2 \rangle_{\text{ex}}] \times 100\%$. Other theoretical views are tabulated in Table 6.

This conclusion that two-state mixing is inadequate is in line with recent experimental observations of $E0$ decays from the normal-deformed and superdeformed 0^+ states to the nominally spherical ground state in ^{40}Ca where it is found that two-state mixing cannot explain the observed monopole decay strengths. Rather, three-state mixing is needed [158]. In this case large basis shell model calculations, which include multinucleon excitations of both protons and neutrons across the $Z = N = 20$ shell gap, are able to describe the $E0$ data. Of relevance for the present discussion is that these data confirm that the naïve spherical ground-state configuration of ^{40}Ca is mixed with deformed intruder structures. This mixing contributes to the shortfall in single-particle strength displayed for valence proton knockout in Figure 15.

A rare view of a deformed nucleus, where a non-intruder spherical excited state has been identified, is ^{44}Ti as depicted in Figure 43. The double-charge exchange reaction identifies the double-isobaric analog state of the ^{44}Ca ground state, which is manifestly a spherical state as characterized by its seniority-dominated low-energy structure. This highlights the role of the many-body symmetrization in dictating deformation. Recall, the nucleon–nucleon interaction is short-ranged and attractive, and the total “space \otimes spin \otimes isospin” wave function is antisymmetric: thus, for maximum binding of nucleons in a nucleus, the space-part of the wave function must be as symmetric as possible (a spatially antisymmetric wave function results in “cancellations” in the many-body energy correlations). It also reveals, via the excitation energy of 9.3 MeV, why the identification of spherical states in nuclei with deformed ground states is extremely difficult and therefore essentially never discussed, but such states are present. Identification of deformed states in

nuclei with spherical ground states is usually achieved via the distinctive rotational bands associated with deformed structures in nuclei; spherical states do not exhibit such easily identified patterns.

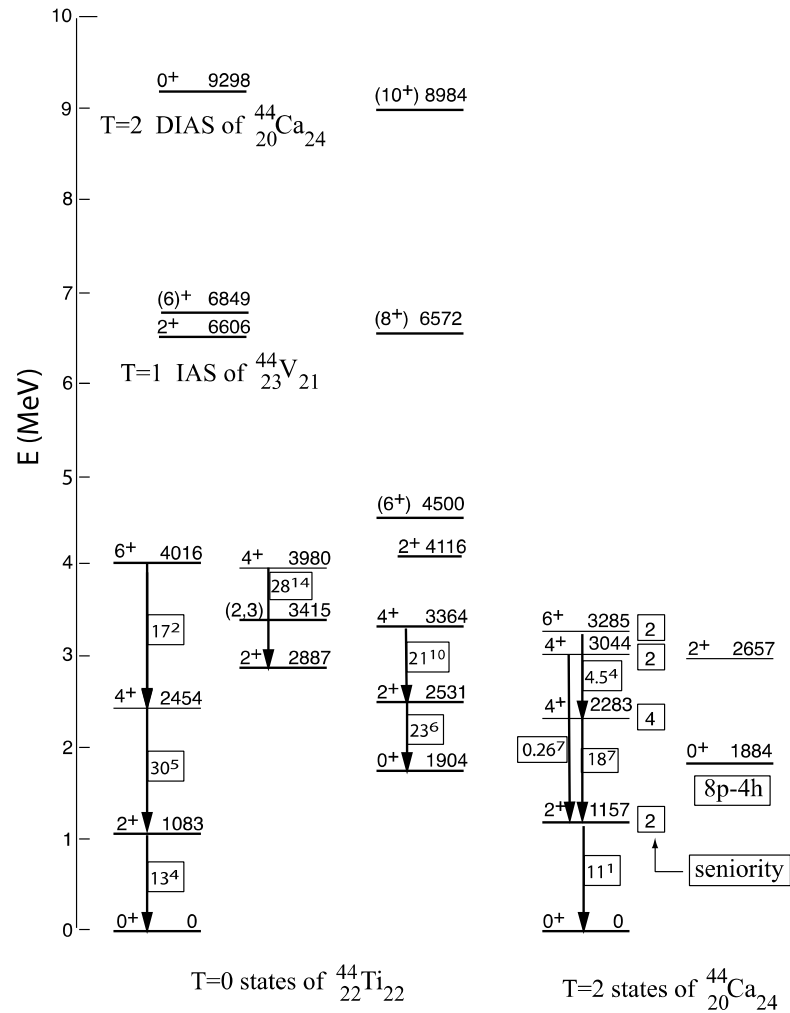


Figure 43. Low-energy $T = 0, 1$ and 2 states of ^{44}Ti and lowest-energy states of ^{44}Ca which are states of isospin $T = 2$. $E2$ transition rates between states are given by $B(E2)$ values (in W.u.). The key feature of the figure is the state at 9298 keV in ^{44}Ti . This state is the double-isobaric analog state of the ^{44}Ca ground state and so, manifestly, it is a “spherical” state. See text for details. Reproduced from [42]. Note: the 1884 keV state in ^{44}Ca is incorrectly identified. As per Table 5 and Figures 35 and 36, it should be labelled as a $\pi(2p - 2h)$ configuration.

The region of ^{40}Ca could be regarded as the confrontational meeting point between shell model descriptions of nuclei and the true nature of the structure of nuclei. Multi-shell configurations manifestly dominate the low-energy structure. This is a proven spectroscopically based interpretation, i.e., it is not a model-inspired interpretation. Beyond this mass region, spectroscopic data that reveal the role of multiparticle-multihole configurations become sparse. Indeed, this region is a key meeting point, not only for shell-model based and multi-shell descriptions of nuclear structure, but also for incorporation of configurations from the continuum, as pointed out in [159].

7. Intruder States, the Shell Model, and Nuclei Adjacent to Closed Shells

7.1. Intruder States

In the lexicon of nuclear structure study, the term “intruder states” has become established. “Intruder” means a state that is observed where it is not expected or “does

not belong". These are states that appear to be shell model states which are observed at low energy on the "wrong side" of a shell model energy gap. Examples are presented in Figures 16 ($^{47,49}\text{Ca}$) and 17 (Tl isotopes), and implicitly for the $9/2^-$ intruder structure in ^{187}Ir in Figure 22. However, intruder states are not simple shell model states because they have underlying correlations in their structure. Indeed, the reason they intrude is because of these correlations. Thus, in Figure 16, an example with important pairing correlations is shown, namely that a simple addition, deduced from one-neutron separation energies, "restores" the low energies of the intruder states to their uncorrelated energies, which reflect the 5 MeV shell gap. In Figure 17, an example with important pairing and deformation correlations is shown, notably that, in addition to the appearance at low energy (pairing correlations), there is a systematic "parabolic" trend in the excitation energies as a function of neutron number, with a minimum near the mid-shell point ($N = 104$), which is where the greatest number of neutrons are active. Much confusion exists in the literature regarding intruder state structures: it appears that they are often viewed as part of a shell model picture. Let us emphasize that the shell model is an independent-particle model based on a spherical mean field. Intruder states are usually strongly deformed and so they are of completely different character to "shell model" structures. For example, they can exhibit rotational bands which can expose their distinctly different character. In effect, the normal and deformed states largely exist in different basis spaces.

It is not implied that rotational bands cannot emerge from shell model calculations. If one could conduct shell model calculations in a sufficiently large space, intruders and their deformation should emerge, but, at present, such calculations are not generally feasible. Consequently, operationally, we have the "coexistence" of shell model descriptions and the Nilsson model plus rotations where nuclei with intruder states are concerned; and we observe actual structures characterized by different $E2$ properties, i.e., quadrupole moments and $B(E2)$ values.

Having noted that rotational structures can begin to emerge in current shell model calculations, we also draw attention to the on-going challenge: the emergence of rotational bands in a finite many-nucleon system calculation is arguably the most profound challenge in a nuclear structure. From everything we understand by the term "a shell model calculation", it is fair to say that this must be a future reality. We look beyond the use of model interactions, such as employed in the Elliott model [160] (where the emergence of rotational bands is guaranteed), and we look to this question using the best effective interactions available. Note that the Elliott model is a single-shell description of states; intruder states demand a multi-shell view. The Elliott model bands are not the generally observed rotational bands in nuclei. It is noteworthy, however, that the Elliott model re-emerges as a submodel of the symplectic shell model, which is discussed in Section 10. By way of shape coexistence, especially in nuclei such as ^{40}Ca , a convergence on a multi-shell view appears most promising (see, e.g., [158]). However, let us note that the key observables that characterize nuclear rotations are specific $E2$ properties: transition and diagonal $E2$ matrix elements with ratios given by rotor-model Clebsch–Gordan coefficients—these are observed to high precision in some nuclei. To be convincing, such a calculation must use the bare charges of the proton and neutron, $e_p = 1e$ and $e_n = 0$ and match the precision of these observed properties.

The most dramatic examples of intruder states are where they appear as the ground-state structures of nuclei. This only occurs in a few local mass regions (such as the ^{32}Mg region, the ^{42}Si region, and perhaps near ^{68}Ni): the term "island of inversion" has become popular for the description of such an occurrence. There is a tendency to place an unphysical emphasis on this terminology: one reads about mapping the borders (or shores) of islands of inversion. However, the structures are not islands; they persist across the entire mass surface, albeit mostly as excited states. A leading example is shown in Figure 44, which depicts systematics in the even-mass $N = 20$ isotones. This is a celebrated historical example. The first clues came from mass measurements [161] and isotope shift measurements [162] in the sodium isotopes. This was shortly followed by a measurement

of $E(2_1^+)$ in ^{32}Mg [163]. A suggested unified view of these observations, from earlier times, is reproduced in Figure 45. However, it took thirty years to establish the lowest spherical state in ^{32}Mg [164], and to explore the structure as an excited state in the neighboring ^{34}Si [165]. It appears that nobody has yet shown an interest in looking at the underlying structure in ^{36}S , but it has been known for a long time in ^{38}Ar . Note that the deformed band in ^{38}Ar is nearly identical in energy spacing to the ground-state band in ^{32}Mg . Our message is that: to refer to the ground-state structure of ^{32}Mg as being part of an “island” is obscuring the discovery frontier of such structures, which must extend to higher excitation energies and broadly encompass nuclides in the region. This is a severe criticism of the misuse of language in science. A schematic view of the energies that contribute to intruder states is shown in Figure 46. A global view that recognizes the dominance of deformation in nuclear ground states is shown in Figure 47.

The challenge of the exploration of intruder states in nuclei is to arrive at the ability to predict their occurrence. With reference to Figure 46, there is a current interest in the so-called monopole energy contribution to the total energy that dictates the appearance of intruder states at low energy in various mass regions. This has received attention already a long time ago [166,167]; more recently, there has been attention from Heyde and collaborators [168], Zuker and collaborators [169], and a review by Otsuka et al. [91]. The theoretical formalism is not a critical concern; but identifying an empirical basis for fixing the relative magnitudes of the energy contributions shown in Figure 46 needs in-depth consideration. The problem is identifying manifestations of monopole energy effects that are free of correlations from pairing and from deformation. These correlations already feature in our chosen subject: they lie at the heart of emergent structures in nuclei, whether involving intruder states or not. Some mass regions of critical concern are addressed below in this Section and in Section 9.

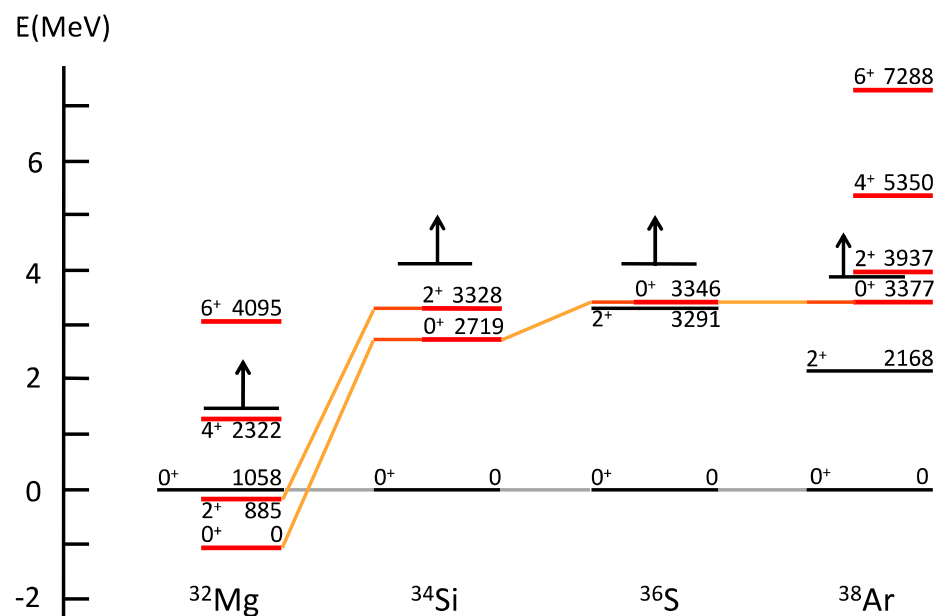


Figure 44. Shape coexistence and intruder states in the $N = 20$ isotones. The 0_2^+ state identifications are made in: ^{32}Mg [164] and ^{34}Si [165]. The intruder states can be understood in an exactly parallel manner to the situation in the Sn isotopes. Thus, here, the 2p-2h configurations involve neutron pairs interacting with protons. The excitation pattern reflects proton subshell structure ($2s_{1/2}$, $1d_{3/2}$) as these orbitals are filled: this is beyond the present level of discussion. Note that the deformed bands in ^{32}Mg and ^{38}Ar possess nearly identical energy spacing. Taken from [8].

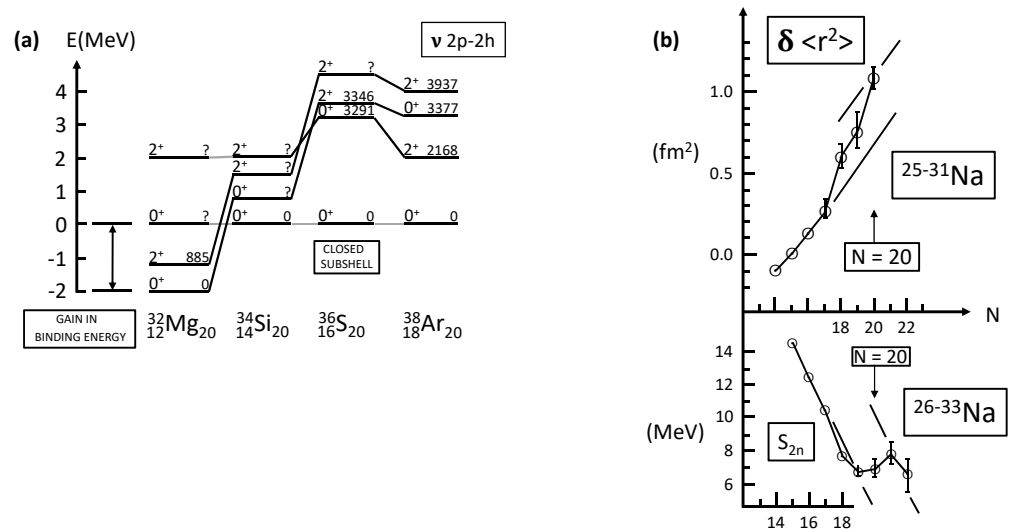


Figure 45. (a) Excited state systematics in the even-mass $N = 20$ isotones. The low-lying 2_1^+ state in ^{32}Mg is interpreted as resulting from a ground state intruder configuration. The ground state of ^{32}Mg should have an anomalously larger mean-square radius. The ground-state binding energy of ^{32}Mg has been reported variously as anomalous and normal. (b) Two-neutron separation energy, S_{2n} , and isotope shift, $\delta\langle r^2 \rangle$, systematics for the neutron-rich Na isotopes [161,162]. The discontinuity at $N = 20$ indicates an increased ground-state mean-square charge radius and increased binding energy. Reproduced from [170].

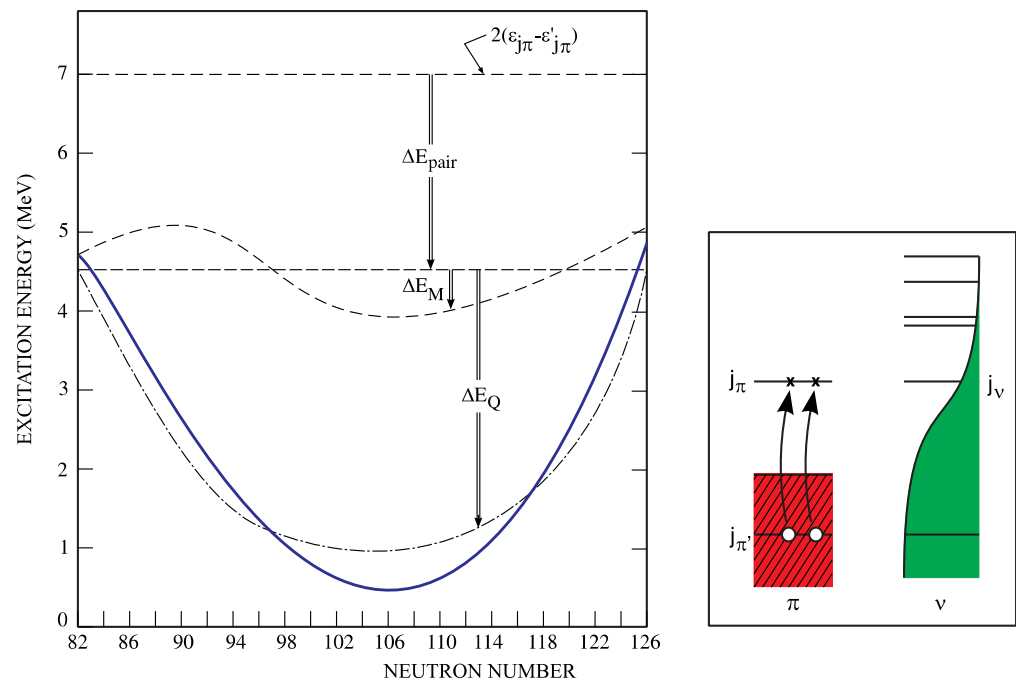


Figure 46. The different energy terms contributing to the energy of the lowest proton 2p-2h 0^+ intruder state for heavy nuclei. On the right-hand side, a schematic view of the excitation is given. On the left-hand side, the unperturbed energy, the pairing energy, the monopole energy shift, and the quadrupole energy gain are presented, albeit in a schematic way. Reprinted with permission from [41]. Copyright (2011) by the American Physical Society.

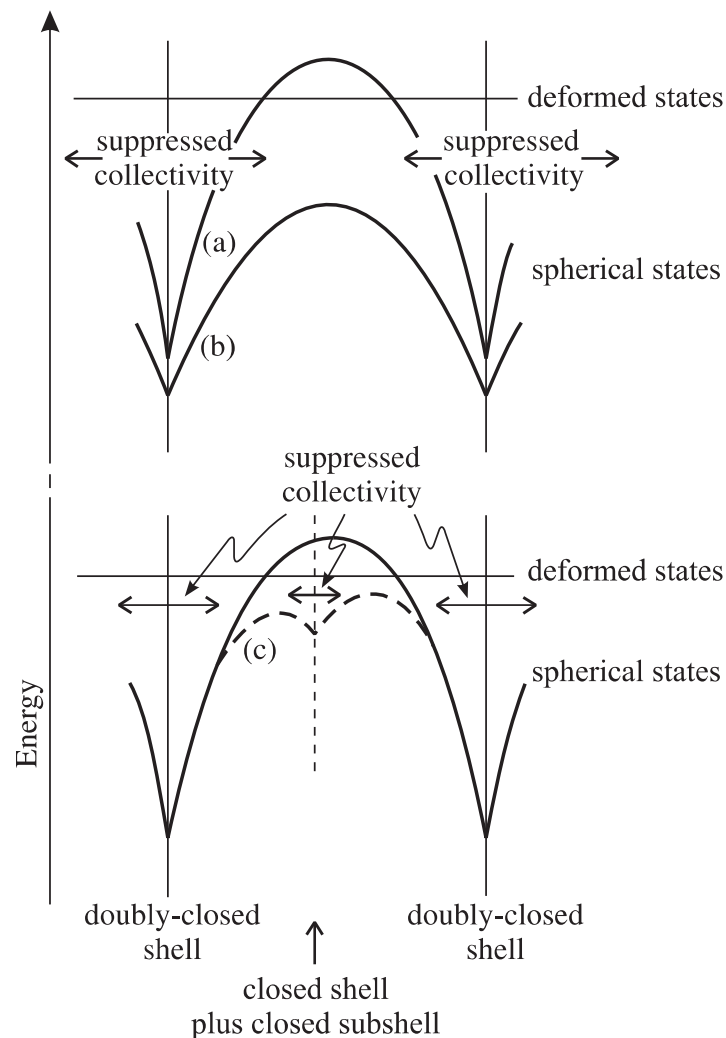


Figure 47. A schematic view of the intruder-state “parabolas”, shown to dramatize the way that shells and subshells suppress the emergence of low-energy collectivity in nuclei. (a) The situation where deformed structures intrude to become the ground state at the middle of a singly closed shell, e.g., ^{32}Mg . (b) The situation where the ground states for a sequence of singly closed shell nuclei remain spherical, but deformed structures form excited intruder bands, e.g., the Sn and Pb isotopes. (c) The situation where a subshell may suppress intrusion of a deformed structure from becoming the ground state or a low-lying excited band, e.g., $N = 50, 82$, cf. Figures 52–54. Reprinted with permission from [41]. Copyright (2011) by the American Physical Society.

The perspective that is presented in Figure 47 appears useful. This view “inverts” the parabolic energy perspective that can be applied to intruder states and, recognizing that most nuclei are deformed, and that shape coexistence probably occurs in all nuclei, expresses the occurrence of spherical shapes in nuclei as intruding to low energies only at and near closed shells. The competition between the controlling energies that lie behind this view devolve onto the configuration interaction problem that is foundational to the nuclear many-body problem.

7.2. Shell Model States

The best view that one possesses of shell model states is of excited states in isotopic and isotonic sequences adjacent to closed shells. Examples are shown in Figures 17, 28 and 29, namely, the low-energy systematics of the odd-mass Tl, In and Sb isotopes, respectively. These views are the best because they are not dominated by pairing correlations with respect

to the unpaired nucleon: it is a single nucleon outside of a singly closed shell. Furthermore, the singly closed shell cores are dominated by spherical, seniority type excitations (when intruder states do not appear at low energy). Thus, one expects that the degrees of freedom of these closed-shell plus or minus one nucleon nuclei are dominated by independent-particle degrees of freedom. If there are any monopole energy shifts, i.e., changes in energy of shell model states across an isotopic sequence, they will be easy to see and easy to interpret. This was the universally held view until the observations on Coulomb excitation of ^{129}Sb summarized in Figure 27, and the implications of these data when compared to the normal weak-coupling model case represented by ^{115}In in Figure 26. The message from the data in Figures 27 and 26 is that, while a nucleon in a unique-parity configuration exhibits weak-coupling $E2$ strength, i.e., the summed strength in the odd-mass nucleus equals the singly closed-shell core strength, manifested in $B(E2; 0_1^+ \rightarrow 2_1^+)$, cf. Figure 26; when j mixing occurs, the $E2$ strength may exceed the weak-coupling value, cf. Figure 27. Thus, $B(E2)$ data such as those in Figures 26 and 27 become a key focal point for exploring the emergence of collectivity in nuclei— j mixing must be quantified. In turn, the issue of j mixing is critical for assessing monopole energy shifts in nuclei: any use of data in nuclei must first be assessed for j mixing before single- j energy shifts can be extracted.

The focus here on the role of j -mixing differs from the emphasis of the discussion of the increased $E2$ strength in ^{129}Sb by Gray et al. [64], where the discussion in terms of shell model calculations identified that the collectivity of the neutron core was not increased by the addition of the extra proton, but rather the increased $E2$ strength arose primarily from the proton–neutron term, thus pointing to overall coherent contributions to the $E2$ strength. The role of j mixing is not immediately evident in this approach.

To explore the role of j -mixing explicitly, schematic particle–vibration model calculations were performed for ^{115}In and ^{129}Sb . A code developed by one of the authors (AES) was employed (see Refs. [171–173]). With ^{115}In modeled as a $1g_{7/2}$ proton hole coupled to the ground and first-excited state of ^{116}Sn , the sum rule was confirmed for the weak-coupling case; however, it was observed that a shortfall in the summed $E2$ strength occurs when the particle–vibration coupling becomes finite. Turning to ^{129}Sb , the low excitation states were described by allowing the odd proton to occupy the $\pi 1g_{7/2}$ and $\pi 2d_{5/2}$ orbits, coupled to the ^{128}Sn core. This is a minimal model to describe the low-excitation positive-parity states shown in Figure 27. The sum rule was confirmed for the weak-coupling limit, and a short-fall in $E2$ excitation strength from the ground state was again observed when the particle–vibration coupling became finite. However, when the proton was also allowed to occupy the $\pi 2d_{3/2}$ orbit as well as $\pi 1g_{7/2}$ and $\pi 2d_{5/2}$, the summed $E2$ strength in ^{129}Sb exceeded that of the ^{128}Sn core.

The above calculations demonstrate the role of j -mixing in the enhanced $E2$ strength observed in ^{129}Sb compared to ^{128}Sn , perhaps in a more transparent way than the large-basis shell model calculations. No tension between the shell model and these schematic particle-vibration model calculations is seen. The important concept is that j mixing means that the sphericity of the mean field has been broken. This is a fundamental point, based on symmetry, behind the emergence of nuclear collectivity. Some additional observations are made on j mixing in the discussion that follows in this Section.

Let us take the above points and consider the systematic features of the odd-mass copper isotopes, shown in Figure 48. A natural first look at j mixing is to assemble information for single-nucleon transfer reactions. As already noted, spectroscopic factors must be handled with caution. However, far more directly, fragmentation of j strength is often observed, as shown in Figure 49 for the copper isotopes. One makes the following observation: j is a quantum number characteristic of a spherical mean-field with spin–orbit coupling; if j strength is fragmented, the mean field is not spherical.

A particular feature of note in the odd-mass copper isotopes is the sudden change in the relative energies of the lowest states with spin–parity $1/2^-$, $3/2^-$, and $5/2^-$ above $N = 40$, cf. Figure 48. These abrupt changes have been interpreted as a major illustration of monopole energy shifts [91], based on the assumption that the observed states are the

$2p_{1/2}$, $2p_{3/2}$, and $1f_{5/2}$ shell model states. However, $E2$ transition strengths in $^{69,71,73}\text{Cu}$, compared to the closed shell cores, $^{68,70,72}\text{Ni}$, cf. Figure 33 reveal that $E2$ transition strength exceeds that in the cores, as seen also in ^{129}Sb , cf. ^{128}Sn (Figure 27). This collectivity is independent of intruder state structures, which are identified in Figure 48. However, the current status of monopole energy shifts requires detailed spectroscopy before it can be discussed quantitatively. Indeed, a recent paper [174] appears to give it dominant status in its role behind the appearance of intruder states at low energy. We would counsel greater caution, and consideration of the structures, interactions and energy dependencies of multiparticle-multihole intruder configurations as shown in Figure 40, in the pursuit of interpretations of the energies of intruder states.

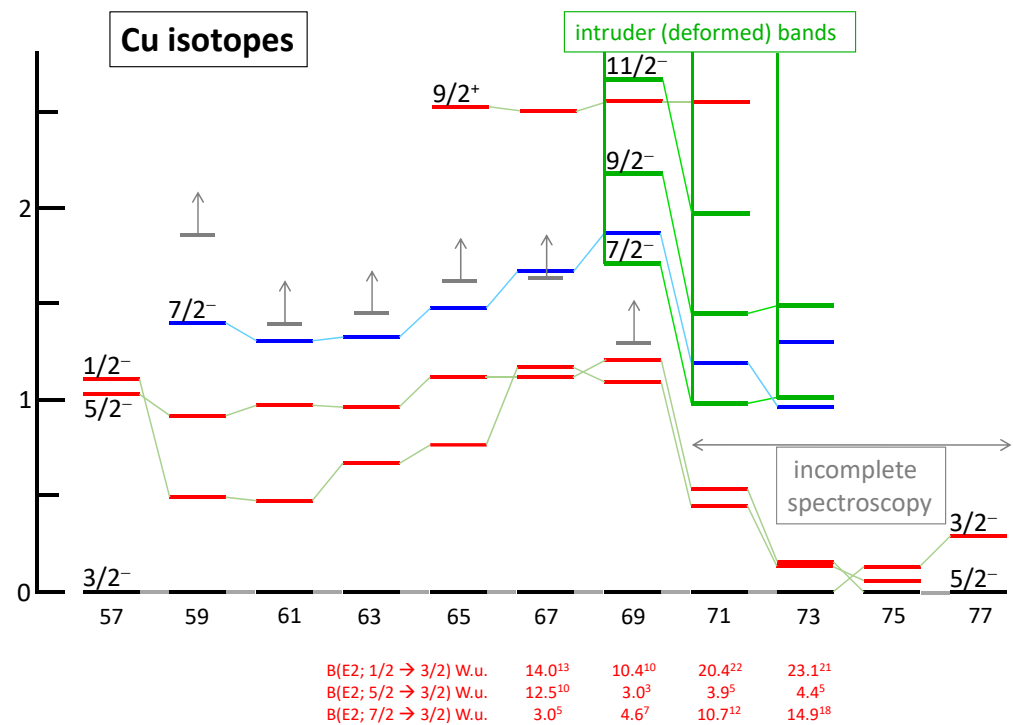


Figure 48. The lowest energy states in the odd-mass Cu isotopes. The naïve interpretation is that these states are simply the manifestation of the expected fp shell model states: $2p_{3/2}$, $2p_{1/2}$, $1f_{5/2}$, $1f_{7/2}$ and $1g_{9/2}$. The existence of rotational band patterns in $^{69,71,73}\text{Cu}$ supports the $7/2^-$ states as the Nilsson state $7/2^-$ [303]. The situation with respect to the other states remains confused: transfer reaction data (shown in Figure 49) reveal fragmentation of single-particle j strength. The experimental situation in $^{71-77}\text{Cu}$ is very incomplete and any interpretation is premature, except—see comments in the text. Horizontal bars with vertical arrows indicate excitation energies above which states are omitted. The $B(E2)$ data of Stefanescu et al. [175] for $^{67,69,71,73}\text{Cu}$ can be compared with the Ni cores, cf. Figure 33: an investigation into collective enhancement in the odd-Cu isotopes relative to the corresponding Ni core nuclei appears to be in order.

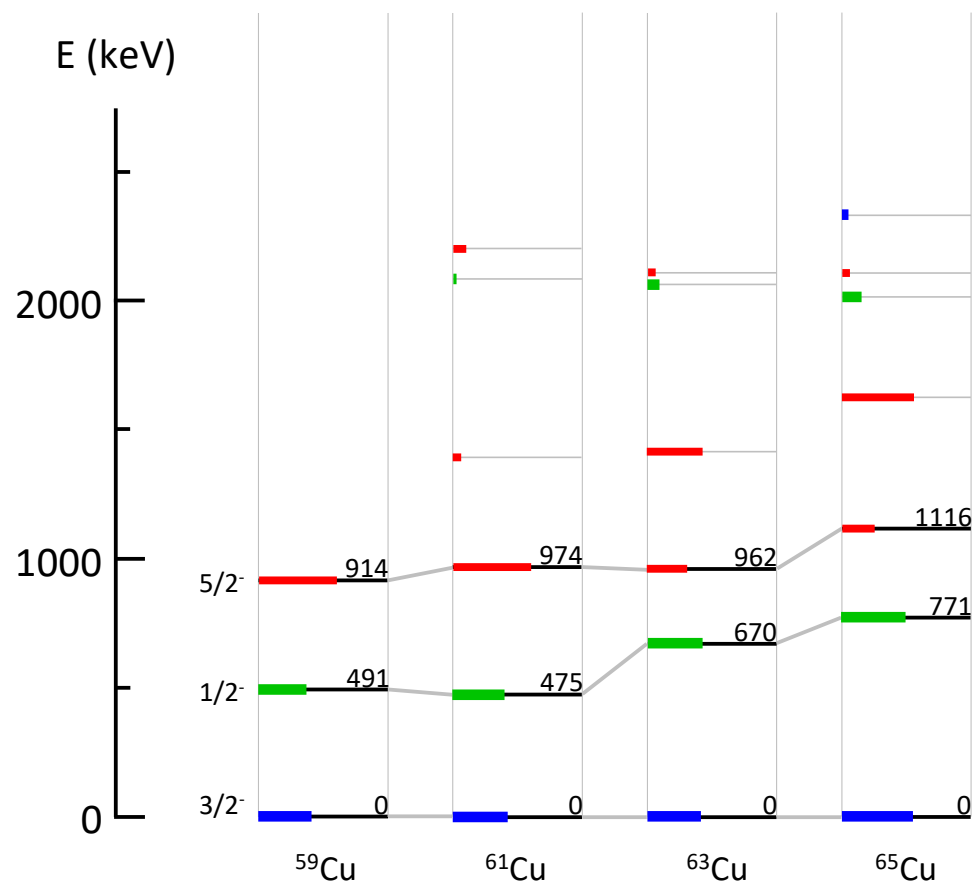


Figure 49. The three lowest states in $^{59-65}\text{Cu}$ and states for which there is significant population in the one-proton transfer reaction ($^3\text{He,d}$). The lengths of the coloured bars are directly proportional to the strength of population of the states in the transfer reaction. The ground-states can be naively interpreted as the shell model configuration $2p_{3/2}$; similarly, the first excited states would appear to be the configuration $2p_{1/2}$. However, the assumption that these are spherical shell model states breaks down for the second excited state where the one-proton transfer strength is severely fragmented. The colour coding indicates the ℓ values of the transferred nucleon — blue ($\ell = 1$ with $j = \ell + 1/2$), green ($\ell = 1$ with $j = \ell - 1/2$), red ($\ell = 3$ with $j = \ell - 1/2$). The direct interpretation is that the ℓ quantum number is not a good quantum number in these nuclei, i.e., they are deformed. Further discussion of such issues must await a more advanced level of treatment. The data are taken from [176]. Reproduced from [8].

Whereas the issue of monopole shifts in subshell energies remains open, no systematic study has been made; the idea has only been applied selectively where there is unfortunately a lack of detailed spectroscopic information [91]. However, detailed information exists, for example in the odd-mass Sc ($Z = 21$) isotopes, as shown in Figures 50 and 51. The parabolic pattern in these figures points to a dominance of deformation-producing forces controlling intruder state energies. Intruder states are strongly deformed structures with both large correlations that originate in their multi-shell structure and in their pairing structure. It would be interesting to make a thorough study of such structures across all nuclei to clarify the role of monopole energy shifts as a factor underlying intruder states and shape coexistence.

Deformation in nuclei immediately adjacent to closed shells has become a recent focus in the odd-mass F ($Z = 9$) isotopes [177]. The data are consistent with deformed ground states. This appears to lie outside of any shell model expectations. Indeed, the surprise that the double-closed shell nucleus ^{28}O does not have a bound ground state, but its neighbour, ^{29}F does, may be because the double-closed shell of ^{28}O does not favour ground-state

deformation, but ^{29}F can deform in its ground state. This would appear to be a simple explanation of the surprise that ^{28}O is unbound (but, to our knowledge, has never been pointed out).

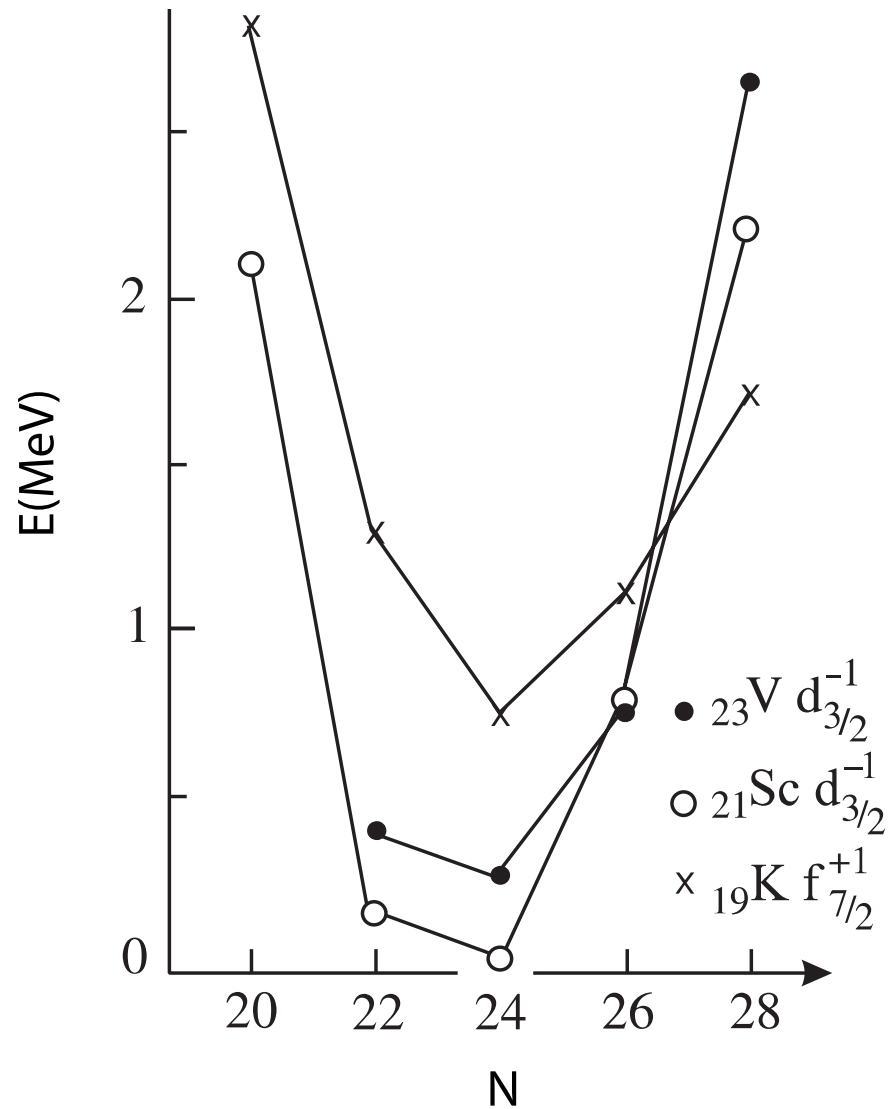


Figure 50. Intruder states in K, Sc, V isotopes. These states are the heads of bands, which are consistent with K quantum numbers equal to the band head spins. $B(E2)$ data for ^{45}Sc are shown in Figure 51. The pattern matches the parabolic trend shown schematically in Figure 46 and supports the dominant role of a quadrupole interaction between protons and neutrons. Note that ^{45}Sc is almost an “island of inversion”, if one ignores the complete range of occurrence of the structure across the entire shell. The figure is adapted from [41].

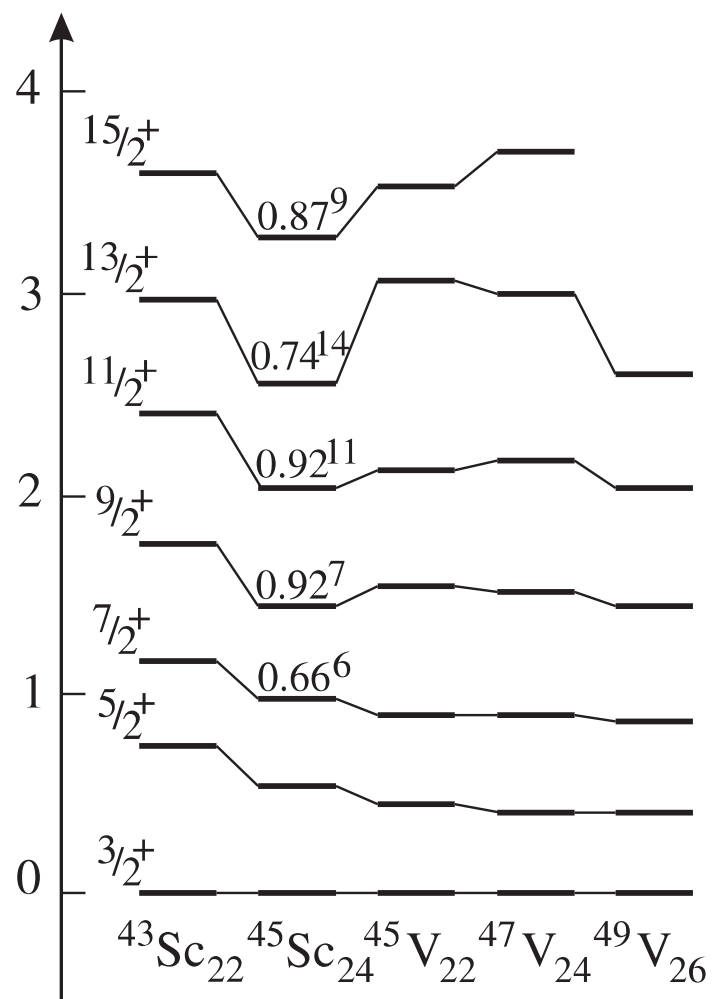


Figure 51. Bands built on the intruder states (cf. Figure 50) in the odd-mass Sc and V isotopes. The numbers given for ^{45}Sc are magnitudes of the intrinsic quadrupole moments, Q_0 ($e \cdot b$) deduced from $B(E2)$ measurements [178]. Adapted from [41].

At present, information on odd-mass nuclei adjacent to $N = 50$ and $N = 82$ remains very limited. Intruder states are observed in the $N = 49$ and $N = 81$ isotones as shown in Figures 52 and 53, respectively. These manifestations are not at the mid-shell points. Possibly, the proton structures, i.e., a subshell gap and/or proximity to a $j = 1/2$ subshell, at $Z = 40$ and $Z = 64$ have something to do with this. Excited 0^+ states for the $N = 50$ and $N = 82$ isotones are shown in Figure 54. At present, the reason for the dissimilarity between $N = 50, 82$ and $Z = 50, 82$ remains an open question. Whether or not there are low-lying excited 0^+ states in, e.g., ^{82}Ge and ^{150}Er , would be worth exploring. The situation at $N = 48$, i.e., in ^{80}Ge , is of two contradicting reports [179,180] and a very recent result that casts further doubt on the existence of a low-energy excited 0^+ state in ^{80}Ge [181]; unlike at $Z = 48$ (the Cd isotopes) where low energy deformed excited 0^+ states are well established (see, e.g., [41,116]).

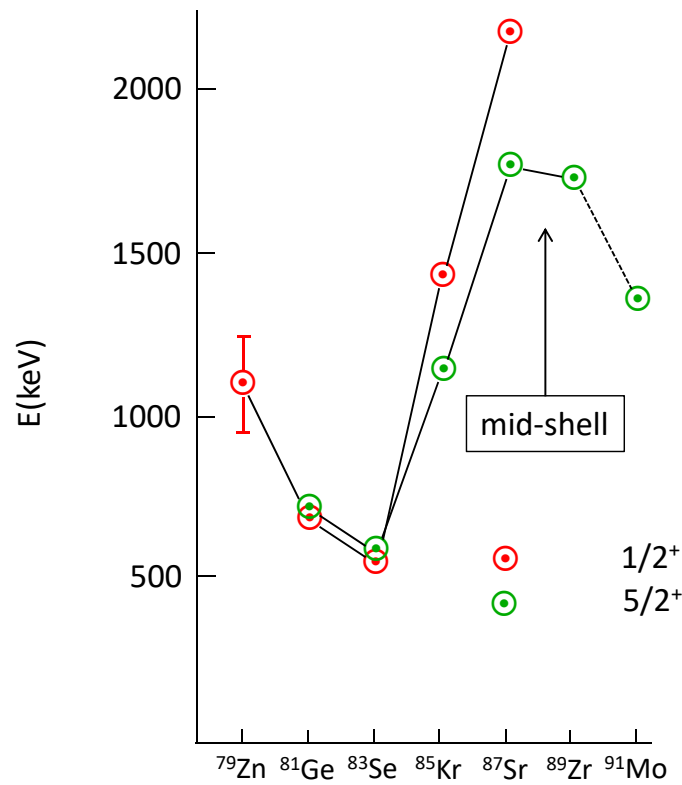


Figure 52. Intruder states in the $N = 49$ isotones. The state in ^{79}Zn is from Orlandi et al. [182] and Yang et al. [183]. The configuration involved may be a prolate deformed structure built on the $1/2^+$ [431] Nilsson state. Note that these structures are nearly identical to the intruder state structures in the odd-In ($Z = 49$) isotopes, some details of which are noted in Section 4. Other data are taken from ENSDF [22]. For comments on the energy maximum at the mid-shell point, see Figure 54 caption.

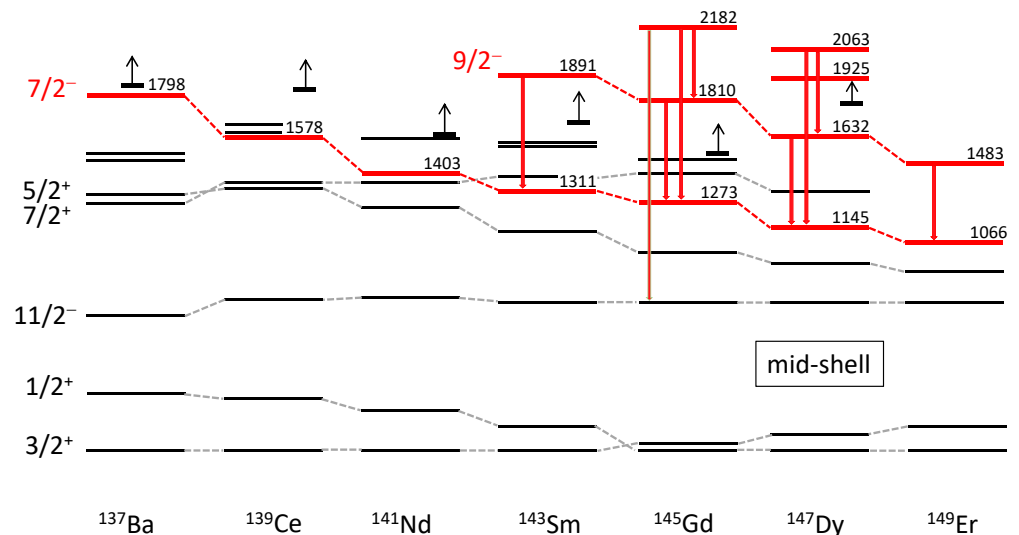


Figure 53. Intruder states in the $N = 81$ isotones (shown in red with all observed decay branches). Horizontal bars with vertical arrows indicate excitation energies above which states are omitted. The mid-shell point is indicated. The configuration involved may be an oblate deformed structure built on the $7/2^-$ [503] Nilsson state. The data are taken from ENSDF [22].

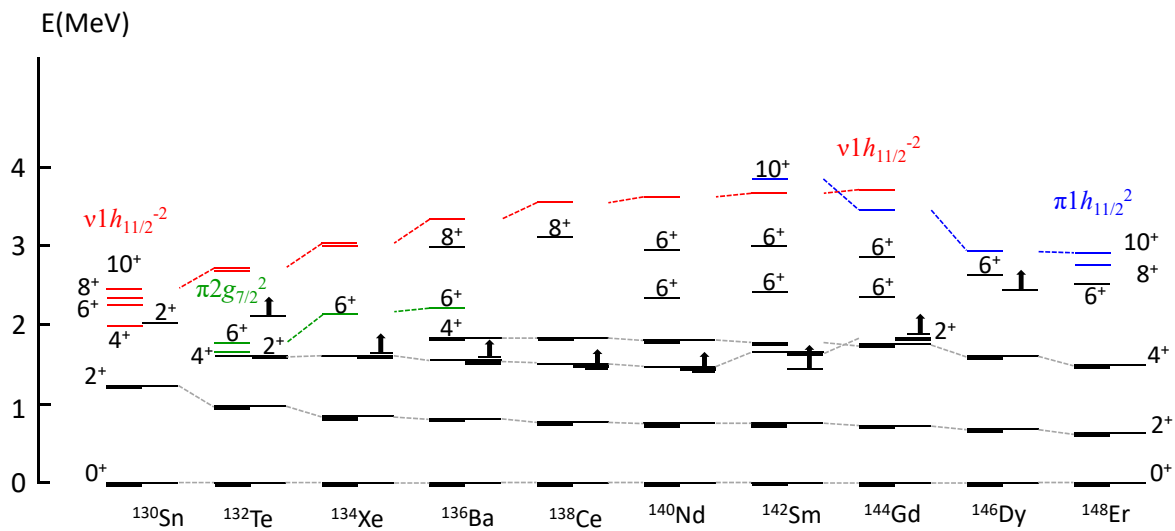


Figure 55. Low-energy systematics of the positive-parity states in the $N = 80$ isotones. The high-spin states are discussed in the text. Vertical arrows indicate energies above which other positive-parity states are observed. First-excited 0^+ states are observed at (keV): ^{134}Xe (1636), ^{136}Ba (1579), ^{138}Ce (1466), ^{140}Nd (1413), ^{142}Sm (1451), ^{144}Gd (1887). The data are taken from ENSDF [22].

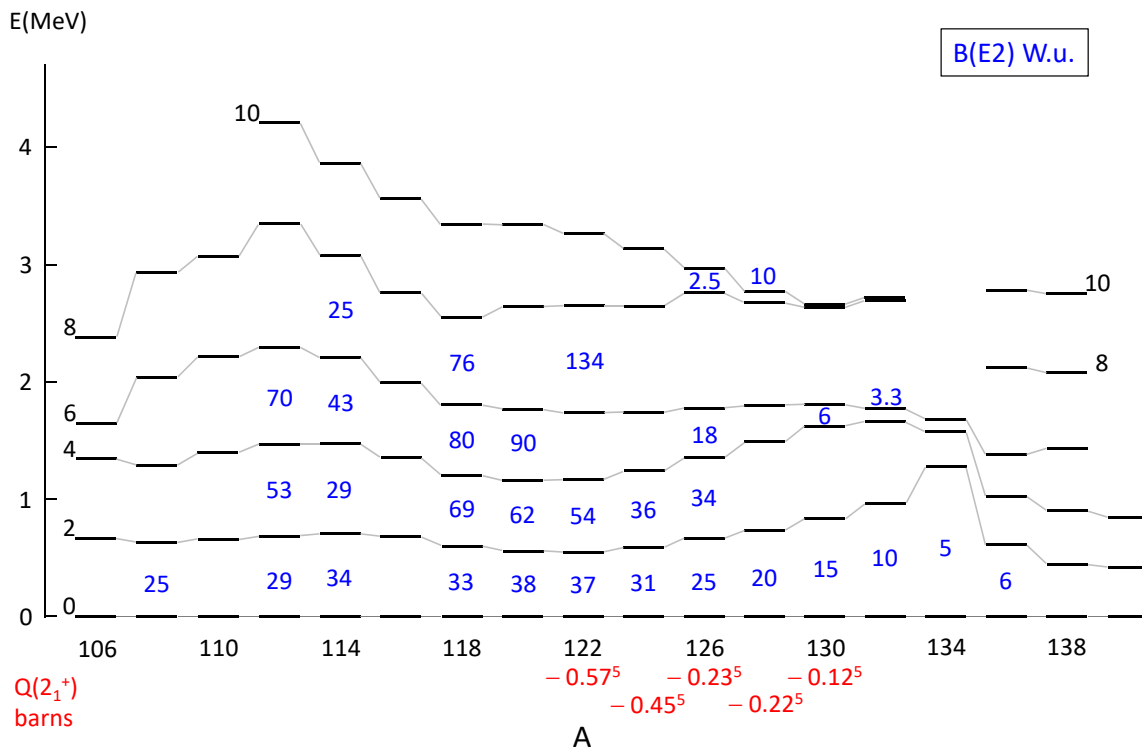


Figure 56. Yrast systematics in the even-mass Te ($Z = 52$) isotopes. Transition $B(E2)$ values in W.u., where measured, are shown in blue between levels. Quadrupole moments of 2_1^+ states, where measured, are shown below the isotope mass numbers. Additional details are given in the text. Data from [195–199] and ENSDF [22]. Figure is from [8].

High- J broken-pair states appear in localized regions across the entire mass surface. In spherical nuclei, they are manifested as seniority isomers; in deformed nuclei, they are manifested as K isomers. The topic of K isomerism is a time-honoured branch of nuclear structure study with comprehensive reviews [200–203]. The situation for transitional nuclei is poorly characterized. Two factors determine the excitation energies of high-

spin broken-pair states: pairing energy and rotational energy. Pairing contributions to broken-pair excitation energies are well understood and are well characterized. Rotational energy contributions to broken-pair excitation energies are epitomized by Figure 25. This aspect of nuclear structure is generally described as “rotational-alignment” effects: there is an enormous literature addressing this topic using the so-called cranked shell model. This model approximates the effects depicted in Figure 25 by “cranking” a deformed mean-field about a fixed axis at right angles to the symmetry axis of the deformed mean field. It has been extended to “tilting” the axis about which cranking occurs [204]. The cranked shell model has completely dominated the study of high-spin states in nuclei. Our concern here is with low-medium spin states in nuclei. Note that, at high spin, an axis of directional quantization approaches a semi-classical description in that the cone of uncertainty becomes narrow; thus, cranking about a fixed axis improves asymptotically with increasing total spin.

To move forward on the topic of the breaking of pairs away from closed shells, it is important to recognize that the prototype signature is properties of the 2_1^+ states in nuclei, which manifestly involve breaking pairs. The leading question is: Which broken-pair configurations underlie a given 2_1^+ state? While important insights can be gained through large-basis shell model calculations in the valence shell, the full answer must extend far beyond the valence shell, as manifested in the need for effective charges to describe $B(E2; 2_1^+ \rightarrow 0_1^+)$ values (see Table 2). By looking at systematics of $B(E2)$ values near closed shells, one expects to learn something about this fundamental aspect of the emergence of collectivity in nuclei. A natural first step is to look at even-even nuclei with one valence proton pair and one valence neutron pair, particles or holes, as will now be discussed.

It turns out that ^{132}Te is one of the more accessible nuclei for a detailed study of what might be termed “prototype emergence of quadrupole collectivity in nuclei”. The region around ^{132}Sn is attractive for this purpose because ^{132}Sn is an $N > Z$ doubly magic core without low-excitation intruder states, and because detailed spectroscopic studies (including transfer reactions, $B(E2)$, and g -factor measurements) show it to be a “good” doubly magic core. However the challenge, which makes performing detailed spectroscopy difficult, is that ^{132}Te is accessible to radioactive beams, by beta-minus decay and as a fission fragment—but not at stable-beam accelerators.

The current knowledge of excitations in ^{132}Te is shown in Figure 57. The extent of detailed information is best described as “inadequate”. For example, a naïve broken-pair view would predict two low-lying 2^+ states, one due to a broken neutron (hole) pair, cf. ^{130}Sn ($E(2_1^+) = 1221$ keV), the other due to a broken proton (particle) pair, cf. ^{134}Te ($E(2_1^+) = 1279$ keV). Thus, (naïvely) there should be two excited 2^+ states in ^{132}Te at 1221 and 1279 keV. The lowest-lying 2^+ states in ^{132}Te are 2_1^+ (974 keV), (2^+) (1665 keV), (2^+) (1778 keV), and then (2^+) states at 2249 and 2364 keV, where the parentheses indicate that the spin–parity assignment is tentative. To pursue the naïve view, the broken-pair configurations can be viewed as mixing and repelling, so that one resulting state appears pushed down by $1221 - 974 = 247$ keV and the other state is at $1270 + 247 = 1517$ keV, cf. (above) 1665 keV. This raises many questions, such as: What is the structure of the states at 1778, 2249 and 2364 keV? What are the detailed properties of these states? Are they 2^+ states? What are their lifetimes, magnetic moments, and quadrupole moments? At present, all unanswered experimentally, except for some information on Coulomb excitation of the 1665 keV state. Note that the $J = 0$ -coupled neutron-hole pair and the $J = 0$ -coupled proton-particle pair also interact and cause an energy shift in the 0^+ configuration that dominates the ground-state of ^{132}Te ; but $[(\pi^2)_J \otimes (v^{-2})_J]_0$ configurations can also be expected to contribute to the ground-state structure. Allowing for pair occupancies across the many shell-model subshells, there are many possibilities. In addition, note that there is an extensive literature that discusses the shell model configurations underlying the structure of ^{132}Te [33,62,205–215].

To begin to answer some of the questions raised concerning the lowest few 2^+ states in ^{132}Te , one can note that there is a single low-excitation proton configuration that forms

a 2^+ state, namely $\pi(1g_{7/2})_{2^+}^2$, with g factor $g = 0.82$. In contrast, the neutron orbits $2d_{3/2}$, $3s_{1/2}$, and $1h_{11/2}$ are “almost degenerate”, which means that low-excitation 2^+ states can be formed by the two-neutron-hole configurations $\nu(2d_{3/2})_{2^+}^{-2}$, $\nu(1h_{11/2})_{2^+}^{-2}$, and $\nu(2d_{3/2}^{-1}3s_{1/2}^{-1})_{2^+}$, with g factors 0.54, -0.24 , and -0.27 , respectively.

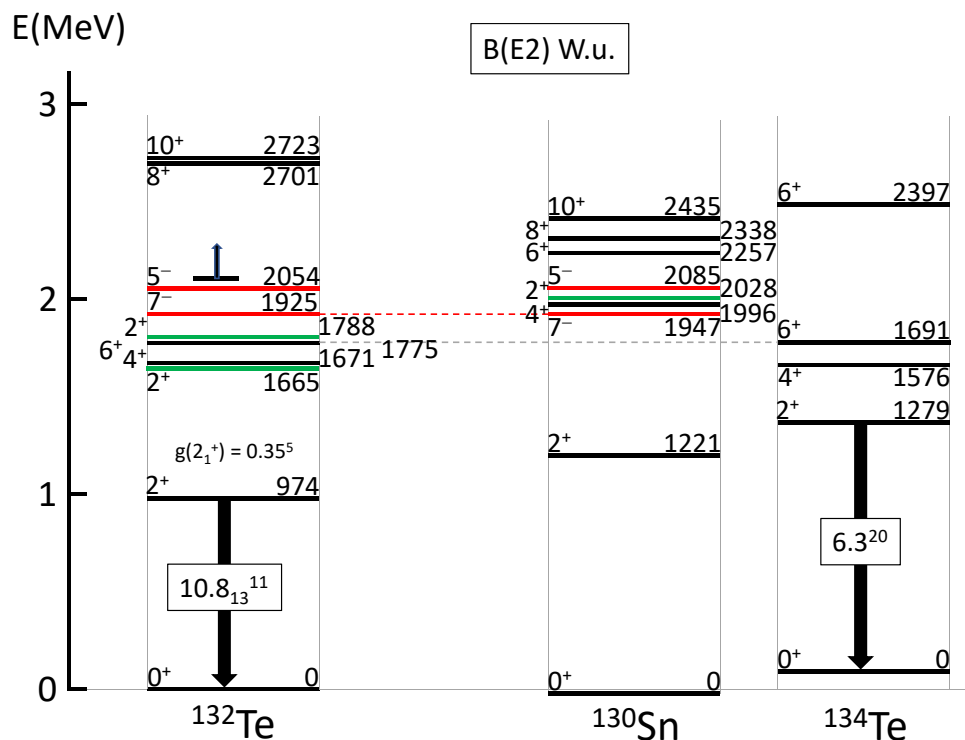


Figure 57. Excited states in ^{132}Te cf. ^{130}Sn and ^{134}Te excited states. Naïvely there should be an appearance of both sets of states, corresponding to the independent “breaking” of the proton particle pair or the neutron hole pair. However, these broken-pair configurations can be expected to interact; thus, the 2_1^+ in ^{132}Te is lower in energy than that in ^{130}Sn and ^{134}Te . See the text for details. The data are taken from ENSDF [22].

Table 7 shows the results of shell model calculations for the lowest five 2^+ states in ^{132}Te . The calculations were performed with NUSHELLX [44] in the $jj55$ basis space and with the $sn100$ interactions; see Table 2 and [31,48,64,68] for additional details including the parameters of the effective $M1$ operator. Along with a comparison of the experimental and theoretical level energies, Table 7 lists the g factors and the decomposition of the wavefunctions into the dominant proton and neutron components coupled to 0^+ and 2^+ . Note that there is no relative phase information available in these structures. The mixing of the lowest two 2^+ states discussed above in relation to Figure 57 is qualitatively consistent with the shell model calculations. The considerable variation in the calculated g factors is an indication of the marked differences in the structures of these 2^+ states. As collectivity emerges, the g factors of all of the low-excitation states would be expected to approach the collective value, typically $g_{\text{coll}} \approx 0.7Z/A$. Such measurements are extremely challenging even for stable nuclides.

Given the complexity of the low-excitation states in ^{132}Te due to the small energy spacing of the $2d_{3/2}$, $3s_{1/2}$, and $1h_{11/2}$ neutron hole orbits, one might consider nuclei like ^{136}Te (approximately $\pi 1g_{7/2} \otimes \nu 2f_{7/2}$) and ^{212}Po (approximately $\pi 1h_{9/2} \otimes \nu 2g_{9/2}$) as alternative “prototypes” to study the emergence of collectivity. Shell model calculations for these nuclei (see Table 2 for details of basis spaces and interactions) show that the configuration mixing in the lowest 2^+ states of these nuclei is already considerable.

Table 7. Shell model calculations for the five lowest 2^+ states in ^{132}Te . The excitation energies and g factors are shown, along with the structure of the state. The structure indicates how the angular momentum is apportioned between protons and neutrons. It is not the wavefunction. The weights indicated sum to unity when all contributions are included.

I_i^π	E_x		g	Structure
	Exp	Theory		
2_1^+	974	954	0.48	$0.38\pi(0^+)\nu(2^+) + 0.51\pi(2^+)\nu(0^+) + 0.07\pi(2^+)\nu(2^+) + \dots$
2_2^+	1665	1645	0.37	$0.49\pi(0^+)\nu(2^+) + 0.32\pi(2^+)\nu(0^+) + 0.02\pi(2^+)\nu(2^+) + \dots$
2_3^+	1788	1931	0.03	$0.71\pi(0^+)\nu(2^+) + 0.11\pi(2^+)\nu(0^+) + 0.13\pi(2^+)\nu(2^+) + \dots$
2_4^+	2249	2258	0.30	$0.83\pi(0^+)\nu(2^+) + 0.03\pi(2^+)\nu(0^+) + 0.07\pi(2^+)\nu(2^+) + \dots$
2_5^+	2364	2468	0.98	$0.06\pi(0^+)\nu(2^+) + 0.77\pi(2^+)\nu(0^+) + 0.01\pi(2^+)\nu(2^+) + \dots$

There are limited simple and accessible cases to study in detail the proton plus neutron broken-pair structures of 2^+ states adjacent to a closed shell. Extending beyond this simplest case, the stable Te isotopes below ^{132}Te provide the opportunity for detailed spectroscopy, including $(n, n' \gamma)$ studies [216], Coulomb excitation, and g -factor measurements [115], to track the emergence of collectivity as increasing numbers of neutron holes are added to the two protons outside the $Z = 50$ shell closure. The stable Xe isotopes, with four protons, are likewise accessible to detailed measurements [30,32,217–223]. In these isotopes, the cancellation of $E2$ strength for four protons in the $1g_{7/2}$ orbit (see Equation (1)) makes the observed $E2$ strengths in the Xe isotopes below ^{136}Xe sensitive to the breakdown of the seniority structure and emerging collectivity.

Returning to the high-spin broken-pair states in this region, specifically the $J = 10$ broken-neutron-pair configurations and the $J = 10$ broken-proton-pair configurations, these do not mix strongly, as manifested in Figure 55, cf. ^{142}Sm and ^{144}Gd . This suggests that broken-pair high- j , high-spin configurations do not play a role in the emergence of collectivity. Figure 56 suggests survival of both the proton-broken-pair and the neutron-broken-pair structures, respectively for $J = 6$ and $J = 10$ in $^{126-132}\text{Te}$. The g factor data, where available, support this suggestion. In the $N = 82$ case of ^{134}Te , $g(6_1^+) = +0.847(25)$ [224], as expected for the $\pi 1g_{7/2}^2$ configuration. The g factors of the 2_1^+ [48] and 4_1^+ [225] states in ^{134}Te are consistent with $g(6_1^+)$, and hence the same configuration. In ^{132}Te , with two neutron holes, $g(2_1^+) = +0.46(5)$ [206,210,226,227] is closer to the collective $g \approx Z/A \approx 0.39$, whereas $g(6_1^+) = +0.78(8)$ [228] remains consistent with that of the pure $\pi 1g_{7/2}^2$ configuration. Recent work at the Australian National University (ANU) tracks the persistence and eventual weakening of the proton-broken-pair structure in the 4^+ states of $^{124,126,128,130}\text{Te}$ [115].

Indeed, discontinuities in yrast state energies persist throughout the open-shell, $Z > 50$, $N < 82$ region and as an example yrast γ -ray energies, E_γ , versus the spins of the initial states, I_i , are shown for the Ba isotopes in Figure 58. It is important to note that K isomerism can emerge in this region, as manifested in Figure 59, which shows the yrast sequences for the even-even $N = 74$ isotones. The band structures show that the deformation increases from ^{128}Xe to ^{140}Dy . An important issue in the emergence of collectivity in nuclei is: where and how is the validity of the K quantum number established?

In principle, measurements of the magnetic dipole and electric quadrupole moments along the sequence of isotones could help answer this question. Unfortunately, the data are limited. The g factors of the 8^- isomers in ^{128}Xe and ^{130}Ba have been measured to be $-0.036(9)$ [229] and $-0.0054(35)$ [230], respectively. The quadrupole moment of the isomer in ^{130}Ba has also been measured to be $Q = +2.77(30)\text{b}$ [230], which corresponds to a deformation of $\epsilon_2 \simeq 0.2$.

In ^{128}Xe , the configuration of the isomer is assigned as $\nu(h_{11/2} \otimes g_{7/2})_{8^-}$. Evaluating the g factor of this configuration with the spin g factor, g_s , quenched from the free-neutron value by the standard factor of 0.7 gives $g(8^-) = -0.046$, consistent with

experiments. Empirical values for $g(1g_{7/2})$ and $g(1h_{11/2})$ from neighboring nuclei give $g(8^-) \approx -0.07$, somewhat larger than the experiment. For ^{130}Ba , the isomer is assigned as $9/2^- [514] \otimes 7/2^- [404]$. The parentage of these Nilsson orbits is $\nu h_{11/2}$ and $\nu g_{7/2}$, i.e., as assigned to the isomer in ^{128}Xe . Evaluating the g factor of the K -isomer with standard Nilsson wavefunctions at $\epsilon_2 = 0.2$ and again quenching g_s by the standard 0.7 factor, gives $g(8^-) = -0.003$, in excellent agreement with the experiment. This result is not sensitive to the deformation. Thus, the moment data suggest that the validity of the K quantum number is established in ^{130}Ba . It appears not to be established in ^{128}Xe . Further insights could be gained from observation and characterization of bands built on the isomers.

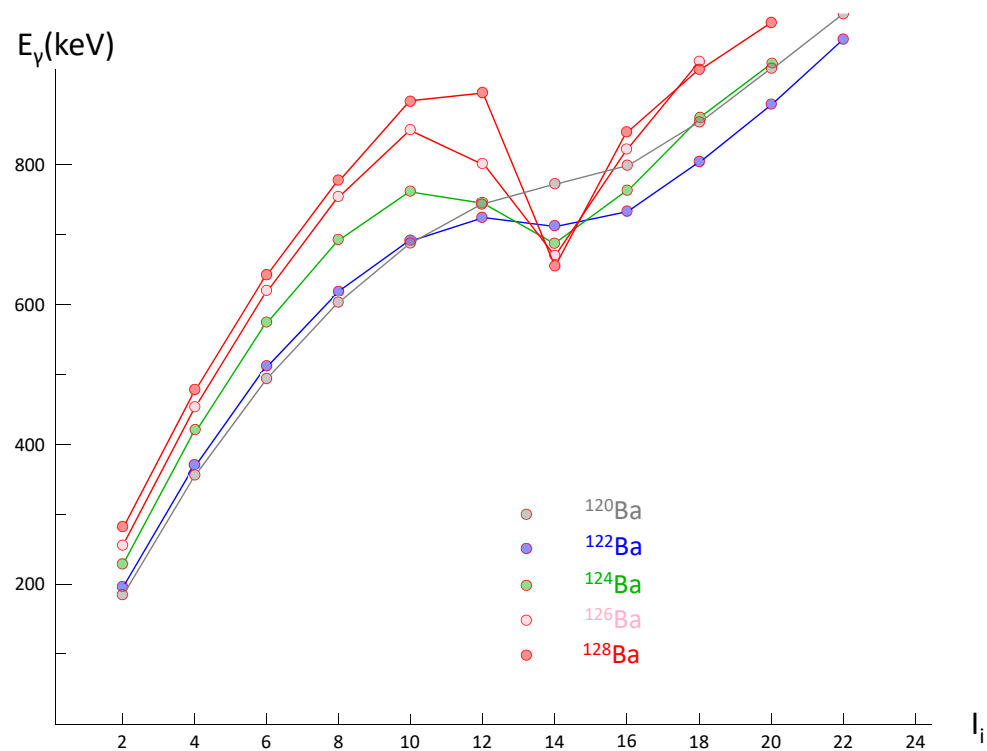


Figure 58. Yrast E_γ vs. I_i for $^{120-128}\text{Ba}$ ($Z = 56$). Note the discontinuity above spin 10. The interpretation is that this is due to dominance of a broken neutron pair, $1h_{11/2}^2$. See discussion in the text. The data are taken from ENSDF [22].

Finally, with respect to the data shown in Figure 59, note that hindrance of the $E1$ isomeric transitions appears to increase with decreasing deformation: this appears counterintuitive. $E1$ transitions are an observable for which systematic features often remain elusive. In the normal valence space, they are forbidden. When looking at $E1$ strength, probably this involves the net result of many small contributions to the matrix element. Nevertheless, there is a visible systematic trend in Figure 59, which lacks an explanation.

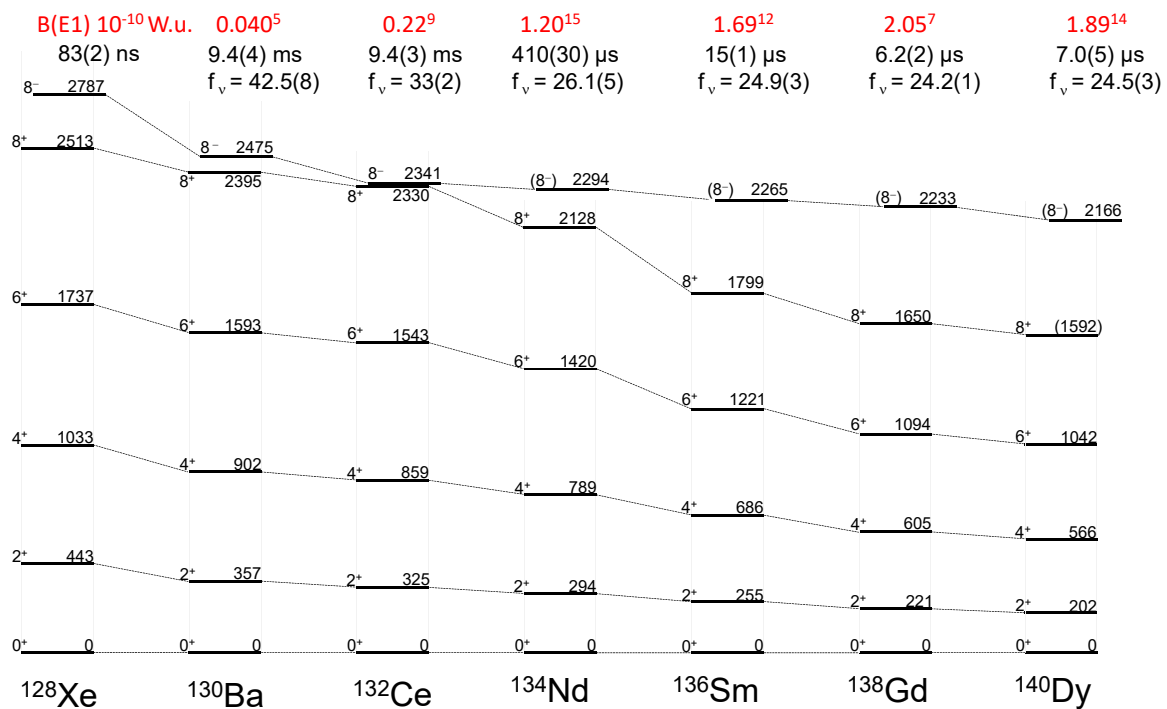


Figure 59. *K* isomers in $N = 74$ isotones. The figure is based on a more limited view presented in Królas et al. [231]. Hindrance factors are $f_v^{-7} = B(E1)$ (in W.u.); the exponent is given by $\Delta K - \lambda$ where $\Delta K = 8$ and $\lambda = 1$, i.e., decay between the $K^\pi = 8^-$ isomer and 8^+ state of the $K = 0$ ground-state band occurs by $E1$ multipole radiation. See text for details. The data are taken from ENSDF [22].

9. $A \sim 56$ and $N \sim 28$: New Regions of Shape Coexistence at Closed Shells

The observation of a deformed band in the double-closed shell nucleus ^{56}Ni [232] suggested that an extension of shape coexistence from the ^{40}Ca region to the $A \sim 56$ region seemed promising. This has not yet materialized. A leading factor is lack of stable targets for multi-nucleon transfer reactions. However, an initiative is underway, with a high-resolution internal-pair spectrometer, the *Super-e*, at the ANU to explore the occurrence of $E0$ transitions in this mass region [128,129,233–236]. However, there is evidence that shape coexistence is present in the $N = 28$ isotones ^{54}Fe and ^{52}Cr from transfer reactions: this is placed in a broad framework in Figure 60. Consistent with the transfer data, the ANU group observes $E0$ transitions in these $N = 28$ isotones.

The program of $E0$ decay studies at ANU has some surprises: while one expects a pattern of shape coexistence adjacent to ^{56}Ni , associated with excited 0^+ states, similar to that observed in nuclei adjacent to ^{40}Ca , this is not apparent in the studies done so far. Evidence of $E0$ transitions other than for $Z = 28$ isotopes and $N = 28$ isotones is limited. However, note that the use of $E0$ transition strength as a spectroscopic fingerprint for shape coexistence depends on a combination of two factors: coexistence of two configurations with very different mean-square charge radii and strong mixing of these configurations [40].

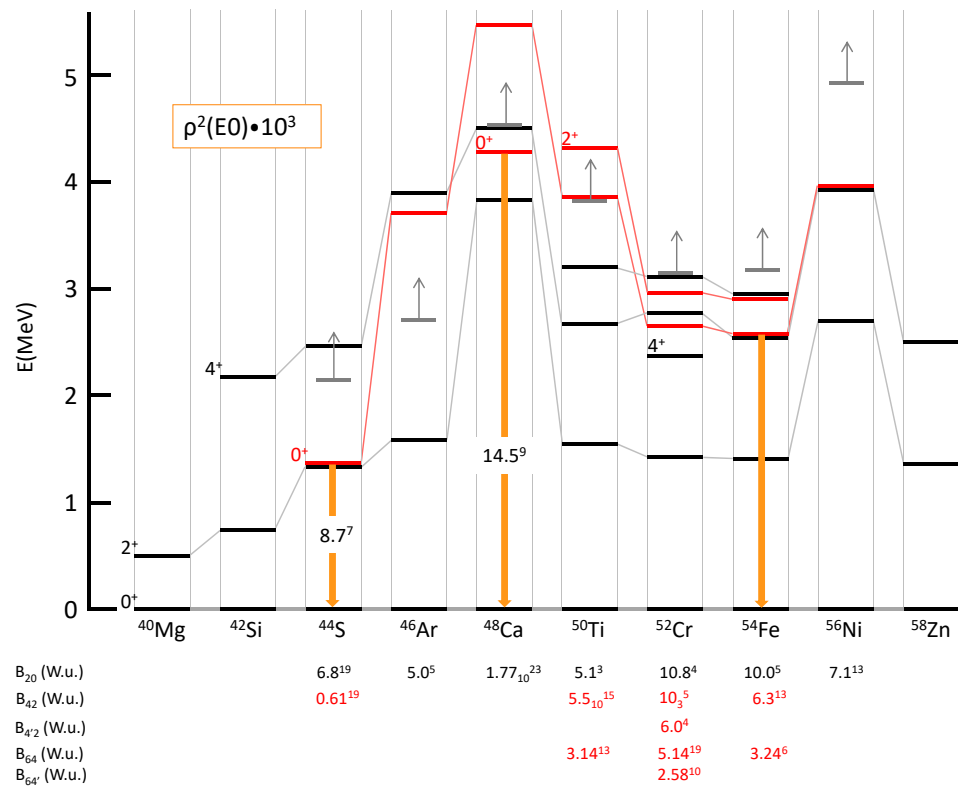


Figure 60. Systematics of the lowest positive-parity states in the $N = 28$ isotones. Candidate ν 2p-2h states are depicted in red. Electric monopole transitions from these states, where observed, are depicted as bold (orange) downwards-pointing arrows, the strengths are indicated where known. The 4282 keV 0^+ state in ^{48}Ca , a π 2p - 2h state is also depicted in red. These assignments are based on two-neutron transfer reaction data [145,237–240]. The $^{58}\text{Ni}(p,t)^{56}\text{Ni}$ reaction does not strongly populate 0^+ states below 6.5 MeV [241]. Data for ^{46}Ar are taken from [45,59,242]. The $B(E2; 2_1^+ \rightarrow 0_1^+)$ data are taken from [199]. Other data are taken from ENSDF [22], except the $B(E2)$ value for the decay of the first 4^+ state in ^{52}Cr , as quoted in ENSDF is in error; the value presented here is calculated from the half life quoted in ENSDF.

With reference to Figure 60, a search for deformed bands built on 0^+ and 2^+ states in ^{52}Cr and ^{54}Fe would be of great interest. Based on the energies of the first excited 2^+ states, deformation appears to dominate the ground-state structure of ^{40}Mg and ^{42}Si (lifetime data would help to support this suggestion). Strengths of $E2$ transitions are shown for the transitions depopulating the 2_1^+ , 4_1^+ , and 6_1^+ states where lifetime data are available. In ^{52}Cr , two 4^+ states are observed: the lowest is dominated by a seniority $v = 4 \pi 1f_{7/2}^4$ configuration and the upper is dominated by a seniority $v = 2 \pi 1f_{7/2}^4$ configuration. The weak B_{42} value in ^{44}S has been interpreted as due to K isomerism, but band structure is not observed [243]; a seniority isomer resulting from a $\pi 1d_{5/2}$ broken pair is equally plausible.

The evidence for shape coexistence in nuclei with $N \sim 28$ and $Z < 20$ is highlighted in Figure 61, which summarizes the connection between intruder states in odd-mass nuclei and low-energy excited 0^+ states in neighbouring even-even nuclei. The accumulation of the necessary data to establish shape coexistence in such neutron-rich nuclei is very demanding with respect to technique and accelerator running times.

0^+ 1884 200ns 2^+ 1157 $\frac{7/2^- \blacktriangle 738}{1/2^+}$ $3/2^+$ 0^+ 0^+ 0 $^{43}_{19}\text{K}_{24}$ $^{44}_{20}\text{Ca}_{24}$	0^+ 1758 53.6 ns 2^+ 1230 $\frac{3/2^+ \blacktriangle 660}{3/2^-}$ $9/2^+$ 0 0^+ 0 $^{117}_{49}\text{In}_{68}$ $^{118}_{50}\text{Sn}_{68}$	2^+ 774 0^+ 658 1.4 min $9/2^- \blacktriangle 281$ $1/2^+$ 0 0^+ 0 $^{189}_{81}\text{Tl}_{108}$ $^{190}_{82}\text{Pb}_{108}$
0^+ 2251 2^+ 2102 115fs $\frac{1/2^- \blacktriangle 320}{1/2^+}$ 0^+ 0 $^{11}_4\text{Be}_7$ $^{12}_4\text{Be}_8$	0^+ 3346 2^+ 3291 1.02 ns $\frac{7/2^- \blacktriangle 1991}{1/2^+}$ $3/2^+$ 0 0^+ 0 $^{35}_{16}\text{S}_{19}$ $^{36}_{16}\text{S}_{20}$	0^+ 1365 2^+ 1330 415 ns $\frac{7/2^- \blacktriangle 321}{3/2^-}$ 0^+ 0 $^{43}_{16}\text{S}_{27}$ $^{44}_{16}\text{S}_{28}$

321 keV state in ^{43}S :
 $B(E2; 7/2^- \rightarrow 3/2^-)$ 0.040^+ W.u.
 $g(7/2^-)$ -0.317^4
 $Q(7/2^-)$ 0.23^3

Figure 61. Selected pairs of nuclei showing a possible relationship between lp-2h intruder states (marked with solid triangles) and low lying excited 0^+ states. The data are from [244–249] and ENSDF [22]. The figure is adapted from [41].

10. A Quantum Mechanical Perspective on Emergent Structures in the Nuclear Many-Body Problem

Nuclei are finite many-body quantum systems that self-organize to yield well-defined sizes and moments. The size of the nucleus determines the energy scale of quantization by virtue of the confinement (specific length) of nucleons (specific mass), scaled by \hbar . Defining the nucleon position and momentum observables, x_j and p_j , with $j = 1, 2, 3$, and the nucleon mass m , this leads to the stationary states of any given nucleus via the definition of a Hamiltonian and the fundamental relationships

$$[x_j, p_j] = i\hbar, \tag{9}$$

and

$$p_j = m\dot{x}_j. \tag{10}$$

The consideration herein is limited to a discussion of model forms of independent-particle potentials and residual two-body interactions between the nucleons. At this point of inception, a representation of the problem for determining the eigenstates of the Hamiltonian must be chosen. This involves the use of symmetries of the Hamiltonian. If the nucleus has spherical symmetry, the handling of the independent-particle part of the Hamiltonian is greatly simplified by using the familiar representation that is a factorization into angular momentum and radial degrees of freedom. This extends to labeling states with angular momentum quantum numbers. The familiar radial confining potentials—the infinite square well and the harmonic oscillator—are solvable in closed form.

The factorization into radial and angular degrees of freedom equips us with the powerful algebra of angular momentum,

$$L_k \equiv x_i p_j - x_j p_i, \tag{11}$$

and

$$[L_i, L_j] = i\hbar \epsilon_{ijk} L_k, \tag{12}$$

where ϵ_{ijk} is the permutation symbol. The power of this algebra, the $so(3)$ Lie algebra, is that it permits an enormous reduction of computational labor via the classification of states and operators as $so(3)$ tensors, with their associated irreducible representations, Kronecker

products, and Wigner–Eckart theorem. Spins of nucleons are simply accommodated by extension of $so(3)$ to its isomorphic algebra, $su(2)$. The Hamiltonian becomes block diagonal in $su(2)$ irreps, reducing computational labor; selection rules emerge; many transitions of interest appear in ratios that depend only on Clebsch–Gordan coefficients.

But, when one factorizes the shell model problem into angular and radial parts, and arrives at the $so(3)$ algebra of angular momentum, one does not look any further for algebraic structures in the problem. However, there is another algebra “right under our noses”: the radial degree of freedom possess an $su(1, 1)$ algebra. This is a so-called dual algebra for the shell model. Details are presented in pedagogical form in [250] and in a more advanced form in [6]. This is not found in any quantum mechanics textbook. It can be used to evaluate radial matrix elements in shell model computations, and this has recently been explored [251]. The algebra is defined by

$$T_1 \equiv \mathbf{r} \cdot \mathbf{r}, \quad T_2 \equiv \frac{1}{2}(\mathbf{r} \cdot \mathbf{p} + \mathbf{p} \cdot \mathbf{r}), \quad T_3 \equiv \mathbf{p} \cdot \mathbf{p}, \quad (13)$$

which, via linear combinations of the $\{T_i\}$ and scale factors, leads to the commutator brackets recognizable as $su(1, 1)$ (see [250]). Indeed, radial matrix elements possess simple relationships including “cancellations”, which reflect properties of $su(1, 1)$ irreps and a $su(1, 1)$ Wigner–Eckart theorem.

Thus, what other algebraic structures can one expect in nuclei that emerge from functions of x_i, p_i and Equation (9)? The clue comes from the dominance of quadrupole deformation in nuclei. One can define “quadrupole” coordinates, $x_i x_j$: these are rank-2 symmetric Cartesian tensors and there are six of them—using $x_i = x, x_j = y, x_k = z$, they are xx, xy, xz, yy, yz, zz . From these, in a straightforward manner, combinations such as xp_x , etc., and $p_x p_x$, etc., are obtained, yielding a Lie algebra with 21 generators, called $sp(3, \mathbb{R})$. Details are presented in pedagogical form in [5] and full details are presented in [6]. The Lie algebra possesses many useful subalgebras: $so(3)$, $su(3)$, and others which need not concern us here; however, note that the $su(3)$ subalgebra is that of the historical Elliott model [160]. A characteristic of the majority of nuclei is that they possess a very large value for the leading $sp(3, \mathbb{R})$ quantum number, \mathcal{N} —the total number of shell model oscillator quanta carried by the sum of all the nucleons—counting the number of oscillator quanta for each nucleon partitioned across the entire occupancy of the oscillator shells of the given nucleus. For example, for ^{168}Er , $\mathcal{N} = 814$ [252]. This leads to contraction in nuclei dominated by the $su(3)$ subalgebra, yielding a (near) rigid rotor with properties that closely match observations [253] with the use of effective charges $e_p = +e, e_n = 0$ [254]. Contraction is a process where a Lie product, e.g., Equation (12), approaches zero asymptotically as quantum numbers become very large: for a state with angular momentum $L = 100$ and projection $m_L = +100$, the cone of indeterminacy appears almost identical to a classical angular momentum vector with three sharp Cartesian components. The origin of the concept of contraction is in a paper by Inonu and Wigner [255]; and the process is often called Inonu–Wigner contraction.

Thus, how does the shell model stand in relationship to the foregoing categorization? The shell model utilizes the $su(2)$ spin-angular momentum algebra and adopts a central potential, but one does not find use of the $su(1, 1)$ algebra. This leaves open the functional form of the central potential: an $su(1, 1)$ algebraic structure is only realized for four central potentials—the Coulomb potential, the harmonic oscillator potential and their less well-known modifications—through augmentation with a $1/r^2$ term—the Kratzer potential and the Davidson potential [256]. Furthermore, the shell model does not make use of the $sp(3, \mathbb{R})$ algebra because of spin–orbit coupling. Such an interaction lies “outside” of the symplectic model and must be treated as a perturbation. While the shell structure of nuclei and the dependence of magic numbers on spin–orbit coupling appear to invalidate the symplectic model, $Q \cdot Q$ interactions shift shell structures by up to 100 MeV, as manifested in observed shape coexisting structure; thus, $L \cdot S$ and $Q \cdot Q$ interactions have their respective domains of influence in nuclear structure. Indeed, the dividing line of their influence epitomizes the primary focus of this contribution. Notably, where the $L \cdot S$ interaction

dominates, J emerges as a good quantum number and pairing interactions result in the emergence of seniority structure and its underlying quasispin $su(2)$ algebra. These few mathematical structures appear to cover all the structures manifested in nuclei, observed so far, and as summarized in this contribution.

The foregoing leaves open the answer to the question posed by the title of this paper. The shell model versus the symplectic model approaches, with their respective dominance by spin–orbit coupling versus quadrupole–quadrupole coupling, each go some way to describing the structure of transitional nuclei. A shell model description can be achieved by using effective interactions. However, it should be noted that it is beginning to emerge that the effective interactions used in ab initio shell model calculations appear to be dominated by just those components that are compatible with symplectic model structures [257–259].

11. Conclusions

The present exploration of the interface between shell model and collective nuclear structure, which we term “emergence of nuclear collectivity”, raises many questions. From a summary of systematic features in data, this paper has focused on the effective charge problem, which reveals itself already in the reduced transition strengths between the first-excited state and the ground state, $B(E2; 2_1^+ \rightarrow 0_1^+)$, in nuclei possessing two valence nucleons coupled to a doubly closed shell. A notable puzzle is the neutron effective charge needed for ^{18}O compared to the well-known value of $e_n \sim +0.5e$ in ^{17}O . It would appear that applying state-of-the-art shell model calculations beyond these simple structures needs great caution; and claims of successful descriptions in such nuclei deserve skepticism. Let us note the issue of spectroscopic factors as deduced from proton knockout by quasiselastic electron scattering [81] (see also [260,261]). The occupancies of particle configurations above the shell closures in doubly closed shell nuclei, shown in Figure 62, indicate that one is likely never dealing with simple shell model configurations when confronting data.

We have suggested directions in which shell model states should be explored as one moves away from closed shells, in the guise of seniority isomers (which involve pairing correlations). We have suggested criteria for exploring the validity of the language of deformation (proton–neutron correlations) in describing weakly deformed nuclei. Notably, nuclei that are termed “transitional” are severely neglected in the spectroscopic data base: we have outlined focal points for experimental study. We concluded with a sketch of details that leads shell model philosophy into the symplectic shell model: in the framework of this model, specific multi-shell configurations are emerging as a major clue to what is going on in low-energy nuclear excitations, and towards which state-of-the-art shell model activity needs to move.

We close with the view: “Data will have the last word in this Shakespearian drama” and “All the [nuclear] World’s a [data] stage, and all the protons and neutrons merely players.” (Adapted from *As You Like It* by W. Shakespeare). The message is that *one needs precision spectroscopy across the mass surface*, as well as pushing to exotic nuclei towards the limits of nuclear stability.

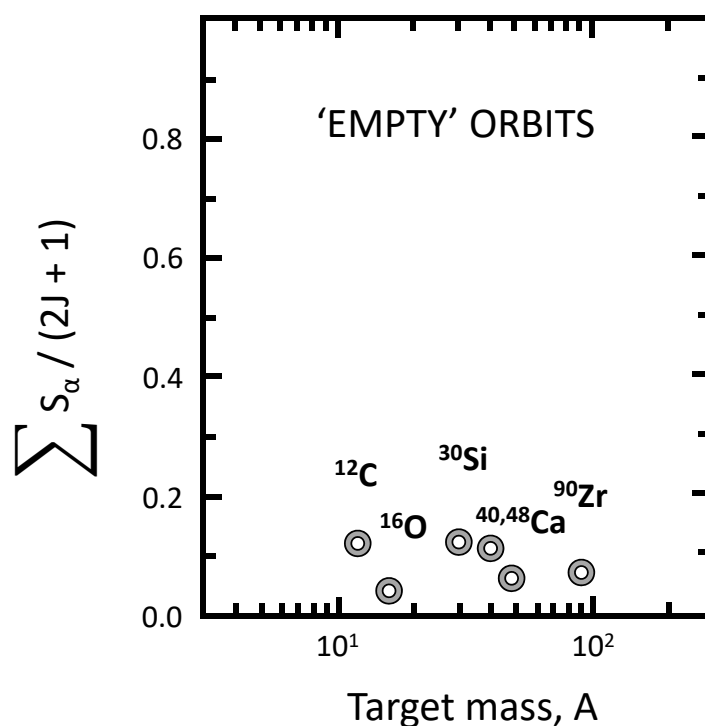


Figure 62. Quasiparticle strength for states just above the Fermi surface, observed in the reaction $(e, e'p)$ as a function of the target mass. All strengths are integrated to an excitation energy of about 20 MeV. Reprinted from [81], Copyright (1993), with permission from Elsevier. The language used in the original paper, from which this figure is taken, needs some clarification. ‘Empty’ orbits refers to shell model configurations above the shell closure, which are conventionally regarded as empty in doubly closed shell nuclei. However, in the $(e, e'p)$ studies, these configurations must have proton occupancy in the doubly closed shell target nuclei to explain the pattern of protons that are knocked out. Thus, one must conclude that the shells are not “closed”.

An underlying theme that emerges in this look at nuclear structure is the role of algebraic structures in the quantum mechanics of the nuclear many-body problem. Two structures are widely manifested where many nucleon configurations are involved. In singly closed shell nuclei, the seniority coupling scheme dominates. This coupling scheme is explained by an $su(2)$ algebra for correlated pairs in j -shell configurations. This stems from dominance of spin–orbit coupling imposed on a spherical mean-field independent-particle description. In open-shell nuclei, the Bohr unified model coupling scheme dominates. This can be traced to an $sp(3, R)$ algebra with contraction on the very large quantum number values involved. Thus, we suggest that a way forward is to explore algebraic structures based on the shell model. This is being pursued, as noted, in the symmetry-adapted and symmetry-guided approaches [257–259], wherein effective charges are not needed.

Author Contributions: Conceptualization, J.L.W. and A.E.S.; methodology, J.L.W. and A.E.S.; validation, J.L.W. and A.E.S.; formal analysis, J.L.W. and A.E.S.; investigation, J.L.W. and A.E.S.; writing—original draft preparation, J.L.W.; writing—review and editing, J.L.W. and A.E.S.; visualization, J.L.W. and A.E.S.; funding acquisition, A.E.S. All authors have read and agreed to the published version of the manuscript.

Funding: This research was funded in part by the Australian Research Council Grant No. DP170101673.

Data Availability Statement: Data available in the references given.

Conflicts of Interest: The authors declare no conflict of interest. The funders had no role in the design of the study; in the collection, analyses, or interpretation of data; in the writing of the manuscript, or in the decision to publish the results.

Abbreviations

The following abbreviations are used in this paper:

ANU	The Australian National University
BCS	Bardeen–Cooper–Schrieffer theory of superconductivity
BMF	Beyond Mean Field
ENSDF	Evaluated Nuclear Structure Data File [22]
PTRM	Particle Triaxial Rotor Model [102]
RPA	Random Phase Approximation [72]
SM	Shell Model

References

- Mayer, M.G. On Closed Shells in Nuclei. II. *Phys. Rev.* **1949**, *75*, 1969–1970. [CrossRef]
- Haxel, O.; Jensen, J.H.D.; Suess, H.E. On the “magic numbers” in nuclear structure. *Phys. Rev.* **1949**, *75*, 1766–1766. [CrossRef]
- Heyde, K.L. *The Nuclear Shell Model*; Springer: Berlin/Heidelberg, Germany, 1990. [CrossRef]
- Bohr, A.; Mottelson, B.R. *Nuclear Structure*; World Scientific Publishing Company: Singapore, 1998. [CrossRef]
- Heyde, K.; Wood, J.L. *Quantum Mechanics for Nuclear Structure*; IOP Publishing: Bristol, UK, 2020; Volume 2, pp. 2053–2563. [CrossRef]
- Rowe, D.J.; Wood, J.L. *Fundamentals of Nuclear Models*; World Scientific: Singapore, 2010. [CrossRef]
- Rosiak, D.; Seidlitz, M.; Reiter, P.; Naidja, H.; Tsunoda, Y.; Togashi, T.; Nowacki, F.; Otsuka, T.; Colò, G.; Arnsward, K.; et al. Enhanced quadrupole and octupole strength in doubly magic ^{132}Sn . *Phys. Rev. Lett.* **2018**, *121*, 252501. [CrossRef] [PubMed]
- Jenkins, D.G.; Wood, J.L. *Nuclear Data. A Primer*; IOP Publishing: Bristol, UK, 2021. [CrossRef]
- Mayer, M.G. Nuclear configurations in the spin–orbit coupling model. I. Empirical evidence. *Phys. Rev.* **1950**, *78*, 16–21. [CrossRef]
- Mayer, M.G. Nuclear configurations in the spin–orbit coupling model. II. Theoretical considerations. *Phys. Rev.* **1950**, *78*, 22–23. [CrossRef]
- Kerman, A. Pairing forces and nuclear collective motion. *Ann. Phys.* **1961**, *12*, 300–329. [CrossRef]
- Racah, G. Theory of complex spectra. I. *Phys. Rev.* **1942**, *61*, 186–197. [CrossRef]
- Racah, G. Theory of complex spectra. II. *Phys. Rev.* **1942**, *62*, 438–462. [CrossRef]
- Racah, G. Theory of complex spectra. III. *Phys. Rev.* **1943**, *63*, 367–382. [CrossRef]
- Flowers, B.H.; Peierls, R.E. Studies in *jj*-coupling. I. Classification of nuclear and atomic states. *Proc. R. Soc. Lond. Ser. Math. Phys. Sci.* **1952**, *212*, 248–263. [CrossRef]
- Helmers, K. Symplectic invariants and Flowers’ classification of shell model states. *Nucl. Phys.* **1961**, *23*, 594–611. [CrossRef]
- Lawson, R.; Macfarlane, M. The quasi-spin formalism and the dependence of nuclear matrix elements on particle number. *Nucl. Phys.* **1965**, *66*, 80–96. [CrossRef]
- Rowe, D.J.; Carvalho, M.J.; Repka, J. Dual pairing of symmetry and dynamical groups in physics. *Rev. Mod. Phys.* **2012**, *84*, 711–757. [CrossRef]
- Anderson, P.W. Random-phase approximation in the theory of superconductivity. *Phys. Rev.* **1958**, *112*, 1900–1916. [CrossRef]
- Cooper, L.N. Bound electron pairs in a degenerate Fermi gas. *Phys. Rev.* **1956**, *104*, 1189–1190. [CrossRef]
- Jungclaus, A.; Cáceres, L.; Górska, M.; Pfützner, M.; Pietri, S.; Werner-Malento, E.; Grawe, H.; Langanke, K.; Martínez-Pinedo, G.; Nowacki, F.; et al. Observation of isomeric decays in the *r*-process waiting-point nucleus $^{130}\text{Cd}_{82}$. *Phys. Rev. Lett.* **2007**, *99*, 132501. [CrossRef]
- Evaluated Nuclear Structure Data File. Available online: <https://www.nndc.bnl.gov/ensdf/> (accessed on 5 March 2022).
- Kameda, D.; Kubo, T.; Ohnishi, T.; Kusaka, K.; Yoshida, A.; Yoshida, K.; Ohtake, M.; Fukuda, N.; Takeda, H.; Tanaka, K.; et al. Observation of new microsecond isomers among fission products from in-flight fission of 345 MeV/nucleon ^{238}U . *Phys. Rev. C* **2012**, *86*, 014319. [CrossRef]
- Palacz, M.; Nyberg, J.; Grawe, H.; Sieja, K.; de Angelis, G.; Bednarczyk, P.; Blazhev, A.; Curien, D.; Dombradi, Z.; Dorvaux, O.; et al. *N* = 50 core excited states studied in the $^{96}\text{Pd}_{50}$ nucleus. *Phys. Rev. C* **2012**, *86*, 014318. [CrossRef]
- Watanabe, H.; Lorusso, G.; Nishimura, S.; Xu, Z.Y.; Sumikama, T.; Söderström, P.A.; Doornenbal, P.; Browne, F.; Gey, G.; Jung, H.S.; et al. Isomers in ^{128}Pd and ^{126}Pd : Evidence for a robust shell closure at the neutron magic number 82 in exotic palladium isotopes. *Phys. Rev. Lett.* **2013**, *111*, 152501. [CrossRef]
- Garnsworthy, A.B.; Regan, P.H.; Pietri, S.; Sun, Y.; Xu, F.R.; Rudolph, D.; Górska, M.; Cáceres, L.; Podolyák, Z.; Steer, S.J.; et al. Isomeric states in neutron-deficient *A* 80–90 nuclei populated in the fragmentation of ^{107}Ag . *Phys. Rev. C* **2009**, *80*, 064303. [CrossRef]
- Park, J.; Krücken, R.; Lubos, D.; Gernhäuser, R.; Lewitowicz, M.; Nishimura, S.; Ahn, D.S.; Baba, H.; Blank, B.; Blazhev, A.; et al. Properties of γ -decaying isomers and isomeric ratios in the ^{100}Sn region. *Phys. Rev. C* **2017**, *96*, 044311. [CrossRef]
- McNeill, J.H.; Blomqvist, J.; Chishti, A.A.; Daly, P.J.; Gelletly, W.; Hotchkis, M.A.C.; Piiparinen, M.; Varley, B.J.; Woods, P.J. Exotic *N*=82 nuclei ^{153}Lu and ^{154}Hf and filling of the $\pi h_{11/2}$ subshell. *Phys. Rev. Lett.* **1989**, *63*, 860–863. [CrossRef] [PubMed]

29. Lozeva, R.L.; Simpson, G.S.; Grawe, H.; Neyens, G.; Atanasova, L.A.; Balabanski, D.L.; Bazzacco, D.; Becker, F.; Bednarczyk, P.; Benzoni, G.; et al. New sub- μ s isomers in $^{125,127,129}\text{Sn}$ and isomer systematics of $^{124-130}\text{Sn}$. *Phys. Rev. C* **2008**, *77*, 064313. [[CrossRef](#)]
30. Peters, E.E.; Van Isacker, P.; Chakraborty, A.; Crider, B.P.; Kumar, A.; Liu, S.H.; McEllistrem, M.T.; Mehl, C.V.; Prados-Estévez, F.M.; Ross, T.J.; et al. Seniority structure of $^{136}\text{Xe}_{82}$. *Phys. Rev. C* **2018**, *98*, 034302. [[CrossRef](#)]
31. Stuchbery, A.E. Gyromagnetic ratios of excited states and nuclear structure near ^{132}Sn . *Aip Conf. Proc.* **2014**, *1625*, 52–58. [[CrossRef](#)]
32. Peters, E.E.; Stuchbery, A.E.; Chakraborty, A.; Crider, B.P.; Ashley, S.F.; Kumar, A.; McEllistrem, M.T.; Prados-Estévez, F.M.; Yates, S.W. Emerging collectivity from the nuclear structure of ^{132}Xe : Inelastic neutron scattering studies and shell-model calculations. *Phys. Rev. C* **2019**, *99*, 064321. [[CrossRef](#)]
33. Brown, B.A.; Stone, N.J.; Stone, J.R.; Towner, I.S.; Hjorth-Jensen, M. Magnetic moments of the 2_1^+ states around ^{132}Sn . *Phys. Rev. C* **2005**, *71*, 044317. [[CrossRef](#)]
34. Teruya, E.; Yoshinaga, N.; Higashiyama, K.; Odahara, A. Shell-model calculations of nuclei around mass 130. *Phys. Rev. C* **2015**, *92*, 034320. [[CrossRef](#)]
35. Sonzogni, A. Nuclear data sheets for $A = 136$. *Nucl. Data Sheets* **2002**, *95*, 837–994. [[CrossRef](#)]
36. Bazzacco, D.; Brandolini, F.; Löwenich, K.; Pavan, P.; Rossi-Alvarez, C.; Maglione, E.; de Poli, M.; Haque, A. Transient-field g-factor measurement of the first 2^+ states in the $N = 82$ nuclei ^{140}Ce , ^{142}Nd and ^{144}Sm . *Nucl. Phys. A* **1991**, *533*, 541–552. [[CrossRef](#)]
37. Lawson, R.D. $(\pi h^{11/2})^n$ States expected in $^{150}_{68}\text{Er}_{82}$, $^{151}_{69}\text{Tm}_{82}$ and $^{152}_{70}\text{Yb}_{82}$. *Z. für Phys. Atoms Nucl.* **1981**, *303*, 51–61. [[CrossRef](#)]
38. Schiffer, J.P.; True, W.W. The effective interaction between nucleons deduced from nuclear spectra. *Rev. Mod. Phys.* **1976**, *48*, 191–217. [[CrossRef](#)]
39. Bron, J.; Hesselink, W.; Van Poelgeest, A.; Zalmstra, J.; Uitzinger, M.; Verheul, H.; Heyde, K.; Waroquier, M.; Vincx, H.; Van Isacker, P. Collective bands in even mass Sn isotopes. *Nucl. Phys. A* **1979**, *318*, 335–351. [[CrossRef](#)]
40. Wood, J.; Heyde, K.; Nazarewicz, W.; Huyse, M.; van Duppen, P. Coexistence in even-mass nuclei. *Phys. Rep.* **1992**, *215*, 101–201. [[CrossRef](#)]
41. Heyde, K.; Wood, J.L. Shape coexistence in atomic nuclei. *Rev. Mod. Phys.* **2011**, *83*, 1467–1521. [[CrossRef](#)]
42. Rowe, D.J.; Wood, J.L. A relationship between isobaric analog states and shape coexistence in nuclei. *J. Phys. Nucl. Part. Phys.* **2018**, *45*, 06LT01. [[CrossRef](#)]
43. Dove, J.; Kerns, B.; McClellan, R.E.; Miyasaka, S.; Morton, D.H.; Nagai, K.; Prasad, S.; Sanftl, F.; Scott, M.B.C.; Tadepalli, A.S.; et al. The asymmetry of antimatter in the proton. *Nature* **2021**, *590*, 561–565. [[CrossRef](#)]
44. The Shell-Model Code NuShellX@MSU. *Nucl. Data Sheets* **2014**, *120*, 115–118. [[CrossRef](#)]
45. Calinescu, S.; Cáceres, L.; Grévy, S.; Sorlin, O.; Dombrádi, Z.; Stanoiu, M.; Astabatyán, R.; Borcea, C.; Borcea, R.; Bowry, M.; et al. Coulomb excitation of ^{44}Ca and ^{46}Ar . *Phys. Rev. C* **2016**, *93*, 044333. [[CrossRef](#)]
46. Radford, D.; Baktash, C.; Barton, C.; Batchelder, J.; Beene, J.; Bingham, C.; Caprio, M.; Danchev, M.; Fuentes, B.; Galindo-Uribarri, A.; et al. Coulomb excitation and transfer reactions with rare neutron-rich isotopes. *Nucl. Phys. A* **2005**, *752*, 264–272. [[CrossRef](#)]
47. Radford, D.C.; Baktash, C.; Barton, C.J.; Batchelder, J.; Beene, J.R.; Bingham, C.R.; Caprio, M.A.; Danchev, M.; Fuentes, B.; Galindo-Uribarri, A.; et al. Coulomb excitation and transfer reactions with neutron-rich radioactive beams. *Eur. Phys. J. A* **2005**, *25*, 383–387. [[CrossRef](#)]
48. Stuchbery, A.E.; Allmond, J.M.; Galindo-Uribarri, A.; Padilla-Rodal, E.; Radford, D.C.; Stone, N.J.; Batchelder, J.C.; Beene, J.R.; Benczer-Koller, N.; Bingham, C.R.; et al. Electromagnetic properties of the 2_1^+ state in ^{134}Te : Influence of core excitation on single-particle orbits beyond ^{132}Sn . *Phys. Rev. C* **2013**, *88*, 051304. [[CrossRef](#)]
49. Kocheva, D.; Rainovski, G.; Jolie, J.; Pietralla, N.; Blazhev, A.; Astier, A.; Altenkirch, R.; Ansari, S.; Braunroth, T.; Cortés, M.L.; et al. A revised $B(E2; 2_1^+ \rightarrow 0_1^+)$ value in the semi-magic nucleus ^{210}Po . *Eur. Phys. J. A* **2017**, *53*, 175. [[CrossRef](#)]
50. Warburton, E.K.; Brown, B.A. Effective interactions for the $0p1s0d$ nuclear shell-model space. *Phys. Rev. C* **1992**, *46*, 923–944. [[CrossRef](#)]
51. Warburton, E.K. Second-forbidden unique β decays of ^{10}Be , ^{22}Na , and ^{26}Al . *Phys. Rev. C* **1992**, *45*, 463–466. [[CrossRef](#)]
52. Brown, B.A.; Richter, W.A. New “USD” Hamiltonians for the sd shell. *Phys. Rev. C* **2006**, *74*, 034315. [[CrossRef](#)]
53. Brown, B.; Sherr, R. Charge-dependent two-body interactions deduced from displacement energies in the $1f_{7/2}$ shell. *Nucl. Phys. A* **1979**, *322*, 61–91. [[CrossRef](#)]
54. Honma, M.; Otsuka, T.; Brown, B.A.; Mizusaki, T. New effective interaction for pf -shell nuclei and its implications for the stability of the $N = Z = 28$ closed core. *Phys. Rev. C* **2004**, *69*, 034335. [[CrossRef](#)]
55. Honma, M.; Otsuka, T.; Brown, B.A.; Mizusaki, T. Shell-model description of neutron-rich pf -shell nuclei with a new effective interaction GXPf 1. *Eur. Phys. J. A* **2005**, *25*, 499–502. [[CrossRef](#)]
56. Utsuno, Y.; Otsuka, T.; Brown, B.A.; Honma, M.; Mizusaki, T.; Shimizu, N. Shape transitions in exotic Si and S isotopes and tensor-force-driven Jahn-Teller effect. *Phys. Rev. C* **2012**, *86*, 051301. [[CrossRef](#)]

57. Horie, H.; Ogawa, K. Effective proton-neutron interaction and spectroscopy of the nuclei with $N=29$. *Prog. Theor. Phys.* **1971**, *46*, 439–461. [CrossRef]
58. Warburton, E.K.; Brown, B.A. Appraisal of the Kuo-Herling shell-model interaction and application to $A = 210 - 212$ nuclei. *Phys. Rev. C* **1991**, *43*, 602–617. [CrossRef] [PubMed]
59. Mengoni, D.; Valiente-Dobón, J.J.; Gadea, A.; Lunardi, S.; Lenzi, S.M.; Broda, R.; Dewald, A.; Pissulla, T.; Angus, L.J.; Aydin, S.; et al. Lifetime measurements of excited states in neutron-rich $^{44,46}\text{Ar}$ populated via a multinucleon transfer reaction. *Phys. Rev. C* **2010**, *82*, 024308. [CrossRef]
60. Scheit, H.; Glasmacher, T.; Brown, B.A.; Brown, J.A.; Cottle, P.D.; Hansen, P.G.; Harkewicz, R.; Hellström, M.; Ibbotson, R.W.; Jewell, J.K.; et al. New Region of Deformation: The Neutron-rich sulfur isotopes. *Phys. Rev. Lett.* **1996**, *77*, 3967–3970. [CrossRef] [PubMed]
61. Gade, A.; Bazin, D.; Campbell, C.M.; Church, J.A.; Dinca, D.C.; Enders, J.; Glasmacher, T.; Hu, Z.; Kemper, K.W.; Mueller, W.F.; et al. Detailed experimental study on intermediate-energy Coulomb excitation of ^{46}Ar . *Phys. Rev. C* **2003**, *68*, 014302. [CrossRef]
62. Wang, H.K.; Ghorui, S.K.; Chen, Z.Q.; Li, Z.H. Analysis of low-lying states, neutron-core excitations, and electromagnetic transitions in tellurium isotopes $^{130-134}\text{Te}$. *Phys. Rev. C* **2020**, *102*, 054316. [CrossRef]
63. Qi, C. Shell-model configuration-interaction description of quadrupole collectivity in Te isotopes. *Phys. Rev. C* **2016**, *94*, 034310. [CrossRef]
64. Gray, T.J.; Allmond, J.M.; Stuchbery, A.E.; Yu, C.H.; Baktash, C.; Gargano, A.; Galindo-Uribarri, A.; Radford, D.C.; Batchelder, J.C.; Beene, J.R.; et al. Early signal of emerging nuclear collectivity in neutron-rich ^{129}Sb . *Phys. Rev. Lett.* **2020**, *124*, 032502. [CrossRef]
65. Allmond, J.M.; Stuchbery, A.E.; Galindo-Uribarri, A.; Padilla-Rodal, E.; Radford, D.C.; Batchelder, J.C.; Bingham, C.R.; Howard, M.E.; Liang, J.F.; Manning, B.; et al. Investigation into the semimagic nature of the tin isotopes through electromagnetic moments. *Phys. Rev. C* **2015**, *92*, 041303. [CrossRef]
66. Ellegaard, C.; Barnes, P.; Eisenstein, R.; Romberg, E.; Bhatia, T.; Canada, T. Inelastic scattering of deuterons, protons and tritons on ^{210}Po . *Nucl. Phys. A* **1973**, *206*, 83–96. [CrossRef]
67. Allmond, J.M.; Stuchbery, A.E.; Baktash, C.; Gargano, A.; Galindo-Uribarri, A.; Radford, D.C.; Bingham, C.R.; Brown, B.A.; Coraggio, L.; Covello, A.; et al. Electromagnetic moments of radioactive ^{136}Te and the emergence of collectivity $2p \oplus 2n$ outside of double-magic ^{132}Sn . *Phys. Rev. Lett.* **2017**, *118*, 092503. [CrossRef] [PubMed]
68. Stuchbery, A.E.; Allmond, J.M.; Danchev, M.; Baktash, C.; Bingham, C.R.; Galindo-Uribarri, A.; Radford, D.C.; Stone, N.J.; Yu, C.H. First-excited state g factor of ^{136}Te by the recoil in vacuum method. *Phys. Rev. C* **2017**, *96*, 014321. [CrossRef]
69. Schielke, S.; Hohn, D.; Speidel, K.H.; Kenn, O.; Leske, J.; Gemein, N.; Offer, M.; Gerber, J.; Maier-Komor, P.; Zell, O.; et al. Evidence for ^{40}Ca core excitation from g factor and $B(E2)$ measurements on the 2_1^+ states of $^{42,44}\text{Ca}$. *Phys. Lett. B* **2003**, *571*, 29–35. [CrossRef]
70. Nuclear Electromagnetic Moments. Available online: <https://www-nds.iaea.org/nuclearmoments/> (accessed on 5 March 2022).
71. East, M.C.; Stuchbery, A.E.; Chamoli, S.K.; Pinter, J.S.; Crawford, H.L.; Wilson, A.N.; Kibédi, T.; Mantica, P.F. Relative g -factor measurements in ^{54}Fe , ^{56}Fe , and ^{58}Fe . *Phys. Rev. C* **2009**, *79*, 024304. [CrossRef]
72. Ring, P.; Schuck, P. *The Nuclear Many-Body Problem*; Springer: Berlin/Heidelberg, Germany, 1980.
73. Hamamoto, I. Giant resonances and polarization effects. *Phys. Scr.* **1972**, *6*, 266–269. [CrossRef]
74. Horikawa, Y.; Hoshino, T.; Arima, A. Polarization effects for higher multipoles. *Phys. Lett. B* **1976**, *63*, 134–138. [CrossRef]
75. Brown, B.A.; Arima, A.; McGrory, J.B. $E2$ core-polarization charge for nuclei near ^{16}O and ^{40}Ca . *Nucl. Phys. A* **1977**, *277*, 77–108. [CrossRef]
76. Sagawa, H. Core polarization charge for $E6$ transition. *Phys. Rev. C* **1979**, *19*, 506–510. [CrossRef]
77. Duguet, T.; Hagen, G. Ab initio approach to effective single-particle energies in doubly closed shell nuclei. *Phys. Rev. C* **2012**, *85*, 034330. [CrossRef]
78. Duguet, T.; Hergert, H.; Holt, J.D.; Somà, V. Nonobservable nature of the nuclear shell structure: Meaning, illustrations, and consequences. *Phys. Rev. C* **2015**, *92*, 034313. [CrossRef]
79. Pandharipande, V.R.; Sick, I.; Huberts, P.K.D. Independent particle motion and correlations in fermion systems. *Rev. Mod. Phys.* **1997**, *69*, 981–991. [CrossRef]
80. Paschalis, S.; Petri, M.; Macchiavelli, A.; Hen, O.; Piasetzky, E. Nucleon-nucleon correlations and the single-particle strength in atomic nuclei. *Phys. Lett. B* **2020**, *800*, 135110. [CrossRef]
81. Lapidás, L. Quasi-elastic electron scattering off nuclei. *Nucl. Phys. A* **1993**, *553*, 297–308. [CrossRef]
82. Vanhalst, M. Quantifying Short-Range Correlations in Nuclei. Ph.D. Thesis, Ghent University, Ghent, Belgium, 2014. Available online: <https://biblio.ugent.be/publication/5713663> (accessed on 5 March 2022).
83. Launey, K.D.; Dytrych, T.; Draayer, J.P. Symmetry-guided large-scale shell-model theory. *Prog. Part. Nucl. Phys.* **2016**, *89*, 101–136. [CrossRef]
84. Kay, B.P.; Schiffer, J.P.; Freeman, S.J. Quenching of cross sections in nucleon transfer reactions. *Phys. Rev. Lett.* **2013**, *111*, 042502. [CrossRef]
85. Mütter, H.; Polls, A.; Dickhoff, W.H. Momentum and energy distributions of nucleons in finite nuclei due to short-range correlations. *Phys. Rev. C* **1995**, *51*, 3040–3051. [CrossRef]
86. Dickhoff, W.H. Determining and calculating spectroscopic factors from stable nuclei to the drip lines. *J. Phys. Nucl. Part. Phys.* **2010**, *37*, 064007. [CrossRef]

87. Baranger, M. A definition of the single-nucleon potential. *Nucl. Phys. A* **1970**, *149*, 225–240. [[CrossRef](#)]
88. Macfarlane, M.H.; French, J.B. Stripping reactions and the structure of light and intermediate nuclei. *Rev. Mod. Phys.* **1960**, *32*, 567–691. [[CrossRef](#)]
89. Kay, B.P.; Schiffer, J.P.; Freeman, S.J.; Tang, T.L.; Cropper, B.D.; Faestermann, T.; Hertenberger, R.; Keatings, J.M.; MacGregor, P.T.; Smith, J.F.; et al. Consistency of nucleon-transfer sum rules in well-deformed nuclei. *Phys. Rev. C* **2021**, *103*, 024319. [[CrossRef](#)]
90. Crawford, H.L.; Macchiavelli, A.O.; Fallon, P.; Albers, M.; Bader, V.M.; Bazin, D.; Campbell, C.M.; Clark, R.M.; Cromaz, M.; Dilling, J.; et al. Unexpected distribution of $\nu 1f_{7/2}$ strength in ^{49}Ca . *Phys. Rev. C* **2017**, *95*, 064317. [[CrossRef](#)]
91. Otsuka, T.; Gade, A.; Sorlin, O.; Suzuki, T.; Utsuno, Y. Evolution of shell structure in exotic nuclei. *Rev. Mod. Phys.* **2020**, *92*, 015002. [[CrossRef](#)]
92. Atomic Mass Evaluation—AME2020, Atomic Mass Data Center. Available online: <https://www-nds.iaea.org/amdc/> (accessed on 5 March 2022).
93. Newton, J.; Cirilov, S.; Stephens, F.; Diamond, R. Possible oblate shape of $9/2^-$ isomer in ^{199}Tl . *Nucl. Phys. A* **1970**, *148*, 593–614. [[CrossRef](#)]
94. Heyde, K.; Van Isacker, P.; Waroquier, M.; Wood, J.; Meyer, R. Coexistence in odd-mass nuclei. *Phys. Rep.* **1983**, *102*, 291–393. [[CrossRef](#)]
95. Meyer-Ter-Vehn, J. Collective model description of transitional odd-A nuclei: (I). The triaxial-rotor-plus-particle model. *Nucl. Phys. A* **1975**, *249*, 111–140. [[CrossRef](#)]
96. Meyer-Ter-Vehn, J. Collective model description of transitional odd-A nuclei: (II). Comparison with unique parity states of nuclei in the $A = 135$ and $A = 190$ mass regions. *Nucl. Phys. A* **1975**, *249*, 141–165. [[CrossRef](#)]
97. Wiebicke, H.; Münchow, L. A weak coupling model for high-spin states. *Phys. Lett. B* **1974**, *50*, 429–432. [[CrossRef](#)]
98. Gizon, J.; Gizon, A.; Meyer-Ter-Vehn, J. Triaxial shape and onset of high-spin bands in ^{129}Ba . *Nucl. Phys. A* **1977**, *277*, 464–476. [[CrossRef](#)]
99. Wiedenhöver, I.; Yan, J.; Neuneyer, U.; Wirowski, R.; von Brentano, P.; Gelberg, A.; Yoshida, N.; Otsuka, T. Non-yrast states in ^{125}Xe . *Nucl. Phys. A* **1995**, *582*, 77–108. [[CrossRef](#)]
100. Modamio, V.; Jungclaus, A.; Algora, A.; Bazzacco, D.; Escrig, D.; Fraile, L.M.; Lenzi, S.; Marginean, N.; Martinez, T.; Napoli, D.R.; et al. New high-spin isomer and quasiparticle-vibration coupling in ^{187}Ir . *Phys. Rev. C* **2010**, *81*, 054304. [[CrossRef](#)]
101. Guo, S.; Zhou, X.H.; Petrache, C.M.; Lawrie, E.A.; Mthembu, S.H.; Fang, Y.D.; Wu, H.Y.; Wang, H.L.; Meng, H.Y.; Li, G.S.; et al. Probing the nature of the conjectured low-spin wobbling bands in atomic nuclei. *Phys. Lett. B* **2022**, *828*, 137010. [[CrossRef](#)]
102. Ragnarsson, I.; Semmes, P.B. Description of nuclear moments and nuclear spectra in the particle-rotor model. *Hyperfine Interact.* **1988**, *43*, 423–440. [[CrossRef](#)]
103. Lieberz, D.; Gelberg, A.; Grandérath, A.; von Brentano, P.; Ragnarsson, I.; Semmes, P. Triaxial rotor plus particle description of negative-parity states in ^{125}Xe . *Nucl. Phys. A* **1991**, *529*, 1–19. [[CrossRef](#)]
104. Lieberz, D.; Gelberg, A.; von Brentano, P.; Ragnarsson, I.; Semmes, P. Signatures of γ deformation in nuclei and an application to ^{125}Xe . *Phys. Lett. B* **1992**, *282*, 7–12. [[CrossRef](#)]
105. Stephens, F.S.; Diamond, R.M.; Leigh, J.R.; Kammuri, T.; Nakai, K. Decoupled yrast states in odd-mass nuclei. *Phys. Rev. Lett.* **1972**, *29*, 438–441. [[CrossRef](#)]
106. Bäcklin, A.; Fogelberg, B.; Malmkog, S. Possible deformed states in ^{115}In and ^{117}In . *Nucl. Phys. A* **1967**, *96*, 539–560. [[CrossRef](#)]
107. Tuttle, W.K.; Stelson, P.H.; Robinson, R.L.; Milner, W.T.; McGowan, F.K.; Raman, S.; Dagenhart, W.K. Coulomb excitation of $^{113,115}\text{In}$. *Phys. Rev. C* **1976**, *13*, 1036–1048. [[CrossRef](#)]
108. Gray, T.J.; Stuchbery, A.E.; Fuderer, L.A.; Allmond, J.M. E2 collectivity in shell-model calculations for odd-mass nuclei near ^{132}Sn . *EPJ Web Conf.* **2020**, *232*, 04007. [[CrossRef](#)]
109. Eberz, J.; Dinger, U.; Huber, G.; Lochmann, H.; Menges, R.; Neugart, R.; Kirchner, R.; Klepper, O.; Kühl, T.; Marx, D.; et al. Spins, moments and mean square charge radii of $^{104-127}\text{In}$ determined by laser spectroscopy. *Nucl. Phys. A* **1987**, *464*, 9–28. [[CrossRef](#)]
110. Brown, B.A. New Skyrme interaction for normal and exotic nuclei. *Phys. Rev. C* **1998**, *58*, 220–231. [[CrossRef](#)]
111. DiJulio, D.D.; Cederkall, J.; Fahlander, C.; Ekström, A.; Hjorth-Jensen, M.; Albers, M.; Bildstein, V.; Blazhev, A.; Darby, I.; Davinson, T.; et al. Coulomb excitation of ^{107}In . *Phys. Rev. C* **2013**, *87*, 017301. [[CrossRef](#)]
112. Vaquero, V.; Jungclaus, A.; Aumann, T.; Tscheuschner, J.; Litvinova, E.V.; Tostevin, J.A.; Baba, H.; Ahn, D.S.; Avigo, R.; Boretzky, K.; et al. Fragmentation of single-particle strength around the doubly magic nucleus ^{132}Sn and the position of the $0f_{5/2}$ proton-hole state in ^{131}In . *Phys. Rev. Lett.* **2020**, *124*, 022501. [[CrossRef](#)] [[PubMed](#)]
113. Kumar, K. Intrinsic quadrupole moments and shapes of nuclear ground states and excited states. *Phys. Rev. Lett.* **1972**, *28*, 249–253. [[CrossRef](#)]
114. Cline, D. Nuclear shapes studied by Coulomb excitation. *Annu. Rev. Nucl. Part. Sci.* **1986**, *36*, 683–716. [[CrossRef](#)]
115. Coombes, B.J. Emergence of Nuclear Collectivity in Cd and Te Isotopes from M1 and E2 Observables. Ph.D. Thesis, The Australian National University, Canberra, Australia, 2022.
116. Garrett, P.E.; Wood, J.L.; Yates, S.W. Critical insights into nuclear collectivity from complementary nuclear spectroscopic methods. *Phys. Scr.* **2018**, *93*, 063001. [[CrossRef](#)]

117. Leoni, S.; Fornal, B.; Mărginean, N.; Sferrazza, M.; Tsunoda, Y.; Otsuka, T.; Bocchi, G.; Crespi, F.C.L.; Bracco, A.; Aydin, S.; et al. Multifaceted Quadruplet of Low-Lying Spin-Zero States in ^{66}Ni : Emergence of shape isomerism in light nuclei. *Phys. Rev. Lett.* **2017**, *118*, 162502. [[CrossRef](#)]
118. Flavigny, F.; Pauwels, D.; Radulov, D.; Darby, I.J.; De Witte, H.; Diriken, J.; Fedorov, D.V.; Fedosseev, V.N.; Fraile, L.M.; Huyse, M.; et al. Characterization of the low-lying 0^+ and 2^+ states in ^{68}Ni via β decay of the low-spin ^{68}Co isomer. *Phys. Rev. C* **2015**, *91*, 034310. [[CrossRef](#)]
119. Ishii, T.; Asai, M.; Makishima, A.; Hossain, I.; Ogawa, M.; Hasegawa, J.; Matsuda, M.; Ichikawa, S. Core-excited states in the doubly magic ^{68}Ni and its neighbor ^{69}Cu . *Phys. Rev. Lett.* **2000**, *84*, 39–42. [[CrossRef](#)]
120. Elman, B.; Gade, A.; Janssens, R.V.F.; Ayangeakaa, A.D.; Bazin, D.; Belarge, J.; Bender, P.C.; Brown, B.A.; Campbell, C.M.; Carpenter, M.P.; et al. Probing the role of proton cross-shell excitations in ^{70}Ni using nucleon knockout reactions. *Phys. Rev. C* **2019**, *100*, 034317. [[CrossRef](#)]
121. Prokop, C.J.; Crider, B.P.; Liddick, S.N.; Ayangeakaa, A.D.; Carpenter, M.P.; Carroll, J.J.; Chen, J.; Chiara, C.J.; David, H.M.; Dombos, A.C.; et al. New low-energy 0^+ state and shape coexistence in ^{70}Ni . *Phys. Rev. C* **2015**, *92*, 061302. [[CrossRef](#)]
122. Chiara, C.J.; Weisshaar, D.; Janssens, R.V.F.; Tsunoda, Y.; Otsuka, T.; Harker, J.L.; Walters, W.B.; Recchia, F.; Albers, M.; Alcorta, M.; et al. Identification of deformed intruder states in semi-magic ^{70}Ni . *Phys. Rev. C* **2015**, *91*, 044309. [[CrossRef](#)]
123. Morales, A.I.; Benzoni, G.; Watanabe, H.; Nishimura, S.; Browne, F.; Daido, R.; Doornenbal, P.; Fang, Y.; Lorusso, G.; Patel, Z.; et al. Low-lying excitations in ^{72}Ni . *Phys. Rev. C* **2016**, *93*, 034328. [[CrossRef](#)]
124. Morales, A.; Benzoni, G.; Watanabe, H.; de Angelis, G.; Nishimura, S.; Coraggio, L.; Gargano, A.; Itaco, N.; Otsuka, T.; Tsunoda, Y.; et al. Is seniority a partial dynamic symmetry in the first $\nu g_{9/2}$ shell? *Phys. Lett. B* **2018**, *781*, 706–712. [[CrossRef](#)]
125. Mazzocchi, C.; Grzywacz, R.; Batchelder, J.; Bingham, C.; Fong, D.; Hamilton, J.; Hwang, J.; Karny, M.; Krolas, W.; Liddick, S.; et al. Low energy structure of even–even Ni isotopes close to ^{78}Ni . *Phys. Lett. B* **2005**, *622*, 45–54. [[CrossRef](#)]
126. Kolos, K.; Miller, D.; Grzywacz, R.; Iwasaki, H.; Al-Shudifat, M.; Bazin, D.; Bingham, C.R.; Braunroth, T.; Cerizza, G.; Gade, A.; et al. Direct lifetime measurements of the excited states in ^{72}Ni . *Phys. Rev. Lett.* **2016**, *116*, 122502. [[CrossRef](#)]
127. Gottardo, A.; de Angelis, G.; Doornenbal, P.; Coraggio, L.; Gargano, A.; Itaco, N.; Kaneko, K.; Van Isacker, P.; Furumoto, T.; Benzoni, G.; et al. Transition strengths in the neutron-rich $^{73,74,75}\text{Ni}$ isotopes. *Phys. Rev. C* **2020**, *102*, 014323. [[CrossRef](#)]
128. Evtits, L.; Garnsworthy, A.; Kibédi, T.; Smallcombe, J.; Reed, M.; Brown, B.; Stuchbery, A.; Lane, G.; Eriksen, T.; Akber, A.; et al. Identification of significant $E0$ strength in the $2^+_2 \rightarrow 2^+_1$ transitions of $^{58,60,62}\text{Ni}$. *Phys. Lett. B* **2018**, *779*, 396–401. [[CrossRef](#)]
129. Evtits, L.J.; Garnsworthy, A.B.; Kibédi, T.; Smallcombe, J.; Reed, M.W.; Stuchbery, A.E.; Lane, G.J.; Eriksen, T.K.; Akber, A.; Alshahrani, B.; et al. $E0$ transition strength in stable Ni isotopes. *Phys. Rev. C* **2019**, *99*, 024306. [[CrossRef](#)]
130. Passoja, A.; Julin, R.; Kantele, J.; Luontama, M. High-resolution study of $E0$ internal pair decay of excited 0^+ states in $^{58,60,62}\text{Ni}$. *Nucl. Phys. A* **1981**, *363*, 399–412. [[CrossRef](#)]
131. Evers, D.; Assmann, W.; Rudolph, K.; Skorka, S.; Sperr, P. The (^3He , n) reaction on even (f, p) shell nuclei at 18 and 21 MeV (I). *Nucl. Phys. A* **1972**, *198*, 268–288. [[CrossRef](#)]
132. Stein, N.; Sunier, J.W.; Woods, C.W. Correspondence between α -transfer and two-proton and two-neutron transfer reactions to the nickel isotopes. *Phys. Rev. Lett.* **1977**, *38*, 587–591. [[CrossRef](#)]
133. Hanson, D.; Stein, N.; Sunier, J.; Woods, C.; Hansen, O. High resolution study of the reactions $^{54,56,58}\text{Fe}(^{16}\text{O}, ^{12}\text{C})^{58,60,62}\text{Ni}$ and a comparison with (^6Li , d) α -transfer spectroscopy. *Nucl. Phys. A* **1979**, *321*, 471–489. [[CrossRef](#)]
134. Hanson, D.; Stein, N.; Woods, C.; Sunier, J.; Hansen, O.; Nilsson, B. The $^{58}\text{Fe}(^{16}\text{O}, ^{14}\text{C})^{60}\text{Ni}$ reaction at 50 MeV. *Nucl. Phys. A* **1980**, *336*, 290–298. [[CrossRef](#)]
135. Amusa, A.; Lawson, R.D. High spin states in ^{94}Ru and ^{95}Rh . *Z. Phys. A* **1982**, *307*, 333–337. [[CrossRef](#)]
136. Mach, H.; Korgul, A.; Górska, M.; Grawe, H.; Matea, I.; Stănoiu, M.; Fraile, L.M.; Penionzkevich, Y.E.; Santos, F.D.O.; Verney, D.; et al. Ultrafast-timing lifetime measurements in ^{94}Ru and ^{96}Pd : Breakdown of the seniority scheme in $N = 50$ isotones. *Phys. Rev. C* **2017**, *95*, 014313. [[CrossRef](#)]
137. Tarasov, O.B.; Ahn, D.S.; Bazin, D.; Fukuda, N.; Gade, A.; Hausmann, M.; Inabe, N.; Ishikawa, S.; Iwasa, N.; Kawata, K.; et al. Discovery of ^{60}Ca and implications for the stability of ^{70}Ca . *Phys. Rev. Lett.* **2018**, *121*, 022501. [[CrossRef](#)] [[PubMed](#)]
138. Pore, J.L.; Andreoiu, C.; Smith, J.K.; MacLean, A.D.; Chester, A.; Holt, J.D.; Ball, G.C.; Bender, P.C.; Bildstein, V.; Braid, R.; et al. Detailed spectroscopy of ^{46}Ca : A study of the β^- decay of ^{46}K . *Phys. Rev. C* **2019**, *100*, 054327. [[CrossRef](#)]
139. Ash, J.; Iwasaki, H.; Mijatović, T.; Budner, T.; Elder, R.; Elman, B.; Friedman, M.; Gade, A.; Grinder, M.; Henderson, J.; et al. Cross-shell excitations in ^{46}Ca studied with fusion reactions induced by a reaccelerated rare isotope beam. *Phys. Rev. C* **2021**, *103*, L051302. [[CrossRef](#)]
140. Lach, M.; Styczeń, J.; Meczyński, W.; Bednarczyk, P.; Bracco, A.; Grebosz, J.; Maj, A.; Merdinger, J.C.; Schulz, N.; Smith, M.B.; et al. In-beam γ -ray spectroscopy of ^{42}Ca . *Eur. Phys. J. A* **2003**, *16*, 309–311. [[CrossRef](#)]
141. Bjerregaard, J.H.; Hansen, O. Violation of seniority in the reaction $^{43}\text{Ca}(d, p)^{44}\text{Ca}$. *Phys. Rev.* **1967**, *155*, 1229–1237. [[CrossRef](#)]
142. Lach, M.; Bednarczyk, P.; Bracco, A.; Grebosz, J.; Kadłuczka, M.; Kintz, N.; Maj, A.; Merdinger, J.C.; Meczyński, W.; Pedroza, J.L.; et al. High-spin states in ^{44}Ca . *Eur. Phys. J. A* **2001**, *12*, 381–382. [[CrossRef](#)]
143. Fortune, H.T.; Al-Jadir, M.N.I.; Betts, R.R.; Bishop, J.N.; Middieton, R. α spectroscopic factors in ^{40}Ca . *Phys. Rev. C* **1979**, *19*, 756–764. [[CrossRef](#)]
144. Middleton, R.; Garrett, J.; Fortune, H. Search for multiparticle-multihole states of ^{40}Ca with the $^{32}\text{S}(^{12}\text{C}, \alpha)$ reaction. *Phys. Lett. B* **1972**, *39*, 339–342. [[CrossRef](#)]

145. Bjerregaard, J.; Hansen, O.; Nathan, O.; Chapman, R.; Hinds, S.; Middleton, R. The (t, p) reaction with the even isotopes of Ca. *Nucl. Phys. A* **1967**, *103*, 33–70. [[CrossRef](#)]
146. Petersen, J.; Parkinson, W. The $^{40}\text{Ar}(\tau, n)^{42}\text{Ca}$ reaction. *Phys. Lett. B* **1974**, *49*, 425–427. [[CrossRef](#)]
147. Fortune, H.; Betts, R.; Bishop, J.; AL-Jadir, M.; Middleton, R. Location of 0^+ 4p-2h and 6p-4h configurations in ^{42}Ca . *Nucl. Phys. A* **1978**, *294*, 208–212. [[CrossRef](#)]
148. Fortune, H.; Vermeulen, J.; Saha, A.; Drentje, A.; Put, L.; de Ruyter van Steveninck, R.; van Hienen, J. Configuration of 3.59 MeV 0^+ state in ^{44}Ca . *Phys. Lett. B* **1978**, *79*, 205–208. [[CrossRef](#)]
149. Peng, J.C.; Stein, N.; Sunier, J.W.; Drake, D.M.; Moses, J.D.; Cizewski, J.A.; Tesmer, J.R. Study of the Reactions $^{46,48}\text{Ti}(^{14}\text{C}, ^{16}\text{O})^{44,46}\text{Ca}$ and $^{50,52}\text{Cr}(^{14}\text{C}, ^{16}\text{O})^{48,50}\text{Ti}$ at 51 MeV. *Phys. Rev. Lett.* **1979**, *43*, 675–678. [[CrossRef](#)]
150. Rowe, D.J.; Thiamova, G.; Wood, J.L. Implications of deformation and shape coexistence for the nuclear shell model. *Phys. Rev. Lett.* **2006**, *97*, 202501. [[CrossRef](#)]
151. Thiamova, G.; Rowe, D.; Wood, J. Coupled-SU(3) models of rotational states in nuclei. *Nucl. Phys. A* **2006**, *780*, 112–129. [[CrossRef](#)]
152. Rowe, D.J. The fundamental role of symmetry in nuclear models. *Aip Conf. Proc.* **2013**, *1541*, 104–136. [[CrossRef](#)]
153. Zheng, D.C.; Berdichevsky, D.; Zamick, L. Near degeneracies of the intrinsic state energies of many-particle, many-hole deformed configurations. *Phys. Rev. Lett.* **1988**, *60*, 2262–2265. [[CrossRef](#)] [[PubMed](#)]
154. Zuker, A.P.; Poves, A.; Nowacki, F.; Lenzi, S.M. Nilsson-SU3 self-consistency in heavy $N = Z$ nuclei. *Phys. Rev. C* **2015**, *92*, 024320. [[CrossRef](#)]
155. Hadyńska-Klęk, K.; Napiorkowski, P.J.; Zielińska, M.; Srebrny, J.; Maj, A.; Azaiez, F.; Valiente Dobón, J.J.; Kicińska Habior, M.; Nowacki, F.; Naïdja, H.; et al. Superdeformed and triaxial states in ^{42}Ca . *Phys. Rev. Lett.* **2016**, *117*, 062501. [[CrossRef](#)]
156. Caurier, E.; Menéndez, J.; Nowacki, F.; Poves, A. Coexistence of spherical states with deformed and superdeformed bands in doubly magic ^{40}Ca : A shell-model challenge. *Phys. Rev. C* **2007**, *75*, 054317. [[CrossRef](#)]
157. Ellegaard, C.; Lien, J.; Nathan, O.; Sletten, G.; Ingebretsen, F.; Osnes, E.; Tjøm, P.; Hansen, O.; Stock, R. The $(1f_{7/2})^2$ multiplet in ^{42}Ca . *Phys. Lett. B* **1972**, *40*, 641–644. [[CrossRef](#)]
158. Ideguchi, E.; Kibédi, T.; Dowie, J.T.H.; Hoang, T.H.; Kumar Raju, M.; Aoi, N.; Mitchell, A.J.; Stuchbery, A.E.; Shimizu, N.; Utsuno, Y.; et al. Electric monopole transition from the superdeformed band in ^{40}Ca . *Phys. Rev. Lett.* **2022**, *128*, 252501. [[CrossRef](#)]
159. Mahzoon, M.H.; Charity, R.J.; Dickhoff, W.H.; Dussan, H.; Waldecker, S.J. Forging the link between nuclear reactions and nuclear structure. *Phys. Rev. Lett.* **2014**, *112*, 162503. [[CrossRef](#)]
160. Elliott, J.P. Collective motion in the nuclear shell model. I. Classification schemes for states of mixed configurations. *Proc. R. Soc. Lond. Ser. Math. Phys. Sci.* **1958**, *245*, 128–145. [[CrossRef](#)]
161. Thibault, C.; Klapisch, R.; Rigaud, C.; Poskanzer, A.M.; Prieels, R.; Lessard, L.; Reisdorf, W. Direct measurement of the masses of ^{11}Li and $^{26-32}\text{Na}$ with an online mass spectrometer. *Phys. Rev. C* **1975**, *12*, 644–657. [[CrossRef](#)]
162. Huber, G.; Touchard, F.; Büttgenbach, S.; Thibault, C.; Klapisch, R.; Duong, H.T.; Liberman, S.; Pinard, J.; Vialle, J.L.; Juncar, P.; et al. Spins, magnetic moments, and isotope shifts of $^{21-31}\text{Na}$ by high resolution laser spectroscopy of the atomic D_1 line. *Phys. Rev. C* **1978**, *18*, 2342–2354. [[CrossRef](#)]
163. Détraz, C.; Guillemaud, D.; Huber, G.; Klapisch, R.; Langevin, M.; Naulin, F.; Thibault, C.; Carraz, L.C.; Touchard, F. Beta decay of $^{27-32}\text{Na}$ and their descendants. *Phys. Rev. C* **1979**, *19*, 164–176. [[CrossRef](#)]
164. Wimmer, K.; Kröll, T.; Krücken, R.; Bildstein, V.; Gernhäuser, R.; Bastin, B.; Bree, N.; Diriken, J.; Van Duppen, P.; Huyse, M.; et al. Discovery of the shape coexisting 0^+ state in ^{32}Mg by a two neutron transfer reaction. *Phys. Rev. Lett.* **2010**, *105*, 252501. [[CrossRef](#)] [[PubMed](#)]
165. Rotaru, F.; Negoita, F.; Grévy, S.; Mrazek, J.; Lukyanov, S.; Nowacki, F.; Poves, A.; Sorlin, O.; Borcea, C.; Borcea, R.; et al. Unveiling the Intruder Deformed 0_2^+ State in ^{34}Si . *Phys. Rev. Lett.* **2012**, *109*, 092503. [[CrossRef](#)] [[PubMed](#)]
166. Sorensen, R.A. Shifts of the spherical single-particle levels. *Nucl. Phys. A* **1984**, *420*, 221–236. [[CrossRef](#)]
167. Goodman, A.L. The $h_{9/2}$ “intruder” state in odd mass Au and Tl isotopes. *Nucl. Phys. A* **1977**, *287*, 1–12. [[CrossRef](#)]
168. Smirnova, N.A.; Heyde, K.; Bally, B.; Nowacki, F.; Sieja, K. Nuclear shell evolution and in-medium NN interaction. *Phys. Rev. C* **2012**, *86*, 034314. [[CrossRef](#)]
169. Duflo, J.; Zuker, A.P. The nuclear monopole Hamiltonian. *Phys. Rev. C* **1999**, *59*, R2347–R2350. [[CrossRef](#)]
170. Wood, J. New developments in nuclear shape coexistence. In *Proceedings of the International Conference on Nuclear Structure Through Static and Dynamic*; Moments; Bolotin, H., Ed.; Conference Proceedings Press: Melbourne, Australia, 1987; Volume II, p. 209.
171. Stuchbery, A.E.; Chamoli, S.K.; Kibédi, T. Particle-rotor versus particle-vibration features in g factors of ^{111}Cd and ^{113}Cd . *Phys. Rev. C* **2016**, *93*, 031302. [[CrossRef](#)]
172. Coombes, B.J.; Stuchbery, A.E.; Blazhev, A.; Grawe, H.; Reed, M.W.; Akber, A.; Dowie, J.T.H.; Gerathy, M.S.M.; Gray, T.J.; Kibédi, T.; et al. Spectroscopy and excited-state g factors in weakly collective ^{111}Cd : Confronting collective and microscopic models. *Phys. Rev. C* **2019**, *100*, 024322. [[CrossRef](#)]
173. Tee, B.P.E.; Stuchbery, A.E.; Vos, M.; Dowie, J.T.H.; Lee, B.Q.; Alotiby, M.; Greguric, I.; Kibédi, T. High-resolution conversion electron spectroscopy of the ^{125}I electron-capture decay. *Phys. Rev. C* **2019**, *100*, 034313. [[CrossRef](#)]
174. Märginean, N.; Little, D.; Tsunoda, Y.; Leoni, S.; Janssens, R.V.F.; Fornal, B.; Otsuka, T.; Michelagnoli, C.; Stan, L.; Crespi, F.C.L.; et al. Shape coexistence at zero spin in ^{64}Ni driven by the monopole tensor interaction. *Phys. Rev. Lett.* **2020**, *125*, 102502. [[CrossRef](#)] [[PubMed](#)]

175. Stefanescu, I.; Georgiev, G.; Balabanski, D.L.; Blasi, N.; Blazhev, A.; Bree, N.; Cederkäll, J.; Cocolios, T.E.; Davinson, T.; Diriken, J.; et al. Interplay between single-particle and collective effects in the odd-*A* Cu isotopes beyond *N* = 40. *Phys. Rev. Lett.* **2008**, *100*, 112502. [[CrossRef](#)] [[PubMed](#)]
176. Schiffer, J.P.; Hoffman, C.R.; Kay, B.P.; Clark, J.A.; Deibel, C.M.; Freeman, S.J.; Honma, M.; Howard, A.M.; Mitchell, A.J.; Otsuka, T.; et al. Valence nucleon populations in the Ni isotopes. *Phys. Rev. C* **2013**, *87*, 034306. [[CrossRef](#)]
177. Macchiavelli, A.O.; Clark, R.M.; Crawford, H.L.; Fallon, P.; Lee, I.Y.; Morse, C.; Campbell, C.M.; Cromaz, M.; Santamaria, C. Core of ²⁵F in the rotational model. *Phys. Rev. C* **2020**, *102*, 041301. [[CrossRef](#)]
178. Bednarczyk, P.; Styczeń, J.; Broda, R.; Lach, M.; Męczyński, W.; Bazzacco, D.; Brandolini, F.; de Angelis, G.; Lunardi, S.; Müller, L.; et al. High spin structure study of the light Odd-*A* *f*_{7/2} nuclei: ⁴⁵Sc, ⁴⁵Ti and ⁴³Ca. *Eur. Phys. J. A* **1998**, *2*, 157–171. [[CrossRef](#)]
179. Gottardo, A.; Verney, D.; Delafosse, C.; Ibrahim, F.; Roussière, B.; Sotty, C.; Rocchia, S.; Andreoiu, C.; Costache, C.; Delattre, M.C.; et al. First evidence of shape coexistence in the ⁷⁸Ni region: Intruder 0₂⁺ state in ⁸⁰Ge. *Phys. Rev. Lett.* **2016**, *116*, 182501. [[CrossRef](#)]
180. Garcia, F.H.; Andreoiu, C.; Ball, G.C.; Bell, A.; Garnsworthy, A.B.; Nowacki, F.; Petrache, C.M.; Poves, A.; Whitmore, K.; Ali, F.A.; et al. Absence of Low-Energy Shape Coexistence in ⁸⁰Ge: The nonobservation of a proposed excited 0₂⁺ level at 639 keV. *Phys. Rev. Lett.* **2020**, *125*, 172501. [[CrossRef](#)]
181. Sekal, S.; Fraile, L.M.; Lică, R.; Borge, M.J.G.; Walters, W.B.; Aprahamian, A.; Benchouk, C.; Bernards, C.; Briz, J.A.; Bucher, B.; et al. Low-spin states in ⁸⁰Ge populated in the β decay of the ⁸⁰Ga 3[−] isomer. *Phys. Rev. C* **2021**, *104*, 024317. [[CrossRef](#)]
182. Orlandi, R.; Mücher, D.; Raabe, R.; Jungclauss, A.; Pain, S.; Bildstein, V.; Chapman, R.; de Angelis, G.; Johansen, J.; Van Duppen, P.; et al. Single-neutron orbits near ⁷⁸Ni: Spectroscopy of the *N* = 49 isotope ⁷⁹Zn. *Phys. Lett. B* **2015**, *740*, 298–302. [[CrossRef](#)]
183. Yang, X.F.; Wraith, C.; Xie, L.; Babcock, C.; Billowes, J.; Bissell, M.L.; Blaum, K.; Cheal, B.; Flanagan, K.T.; Garcia Ruiz, R.F.; et al. Isomer Shift and Magnetic Moment of the Long-Lived 1/2⁺ Isomer in ⁷⁹Zn₄₉: Signature of Shape Coexistence near ⁷⁸Ni. *Phys. Rev. Lett.* **2016**, *116*, 182502. [[CrossRef](#)] [[PubMed](#)]
184. Mullins, S.M.; Watson, D.L.; Fortune, H.T. ⁸²Se(*t,p*)⁸⁴Se reaction at 17 MeV. *Phys. Rev. C* **1988**, *37*, 587–594. [[CrossRef](#)] [[PubMed](#)]
185. Flynn, E.R.; Sherman, J.D.; Stein, N.; Olsen, D.K.; Riley, P.J. ⁸⁴Kr(*t,p*)⁸⁶Kr and ⁸⁶Kr(*t,p*)⁸⁸Kr reactions. *Phys. Rev. C* **1976**, *13*, 568–577. [[CrossRef](#)]
186. Ragaini, R.C.; Knight, J.D.; Leland, W.T. Levels of ⁸⁸Sr from the ⁸⁶Sr(*t,p*)⁸⁸Sr reaction. *Phys. Rev. C* **1970**, *2*, 1020–1036. [[CrossRef](#)]
187. Flynn, E.; Cizewski, J.; Brown, R.E.; Sunier, J. 136,138Ba(*t,p*) and the systematics of neutron pairing vibrations at *N* = 82. *Phys. Lett. B* **1981**, *98*, 166–168. [[CrossRef](#)]
188. Mulligan, T.J.; Flynn, E.R.; Hansen, O.; Casten, R.F.; Sheline, R.K. (*t,p*) and (*p,t*) Reactions on even Ce isotopes. *Phys. Rev. C* **1972**, *6*, 1802–1814. [[CrossRef](#)]
189. Ball, J.B.; Auble, R.L.; Roos, P.G. Study of the zirconium isotopes with the (*p,t*) reaction. *Phys. Rev. C* **1971**, *4*, 196–214. [[CrossRef](#)]
190. Ball, J.B.; Larsen, J.S. Systematics of *L* = 0 transitions observed in the (*p,t*) reaction of nuclei near *N* = 50. *Phys. Rev. Lett.* **1972**, *29*, 1014–1017. [[CrossRef](#)]
191. Ball, J.; Fulmer, C.; Larsen, J.; Sletten, G. Energy levels of ⁹⁴Ru observed with the ⁹⁶Ru(*p,t*) reaction. *Nucl. Phys. A* **1973**, *207*, 425–432. [[CrossRef](#)]
192. Ball, J.; Auble, R.; Rapaport, J.; Fulmer, C. Levels in ^{140,142,144}Nd and a search for pairing vibrations at *N* = 82 with the (*p,t*) reaction. *Phys. Lett. B* **1969**, *30*, 533–535. [[CrossRef](#)]
193. Flynn, E.R.; van der Plicht, J.; Wilhelmy, J.B.; Mann, L.G.; Struble, G.L.; Lanier, R.G. ¹⁴⁶Gd and ¹⁴⁴Sm excited by the (*p,t*) reaction on radioactive targets. *Phys. Rev. C* **1983**, *28*, 97–104. [[CrossRef](#)]
194. Häusser, O.; Taras, P.; Trautmann, W.; Ward, D.; Alexander, T.K.; Andrews, H.R.; Haas, B.; Horn, D. *g* factors of high-spin yrast traps in ^{146,147}Gd. *Phys. Rev. Lett.* **1979**, *42*, 1451–1454. [[CrossRef](#)]
195. Möller, O.; Warr, N.; Jolie, J.; Dewald, A.; Fitzler, A.; Linnemann, A.; Zell, K.O.; Garrett, P.E.; Yates, S.W. E2 transition probabilities in ¹¹⁴Te: A conundrum. *Phys. Rev. C* **2005**, *71*, 064324. [[CrossRef](#)]
196. Mihai, C.; Pasternak, A.A.; Filipescu, D.; Ivaşcu, M.; Bucurescu, D.; Căta Danil, G.; Căta Danil, I.; Deleanu, D.; Ghiţă, D.; Glodariu, T.; et al. Side feeding patterns and nuclear lifetime determinations by the Doppler shift attenuation method in (*α,nγ*) reactions. *Phys. Rev. C* **2010**, *81*, 034314. [[CrossRef](#)]
197. Mihai, C.; Pasternak, A.A.; Pascu, S.; Filipescu, D.; Ivaşcu, M.; Bucurescu, D.; Căta Danil, G.; Căta Danil, I.; Deleanu, D.; Ghiţă, D.G.; et al. Lifetime measurements by the Doppler-shift attenuation method in the ¹¹⁵Sn(*α,nγ*)¹¹⁸Te reaction. *Phys. Rev. C* **2011**, *83*, 054310. [[CrossRef](#)]
198. Saxena, M.; Kumar, R.; Jhingan, A.; Mandal, S.; Stolarz, A.; Banerjee, A.; Bhowmik, R.K.; Dutt, S.; Kaur, J.; Kumar, V.; et al. Rotational behavior of ^{120,122,124}Te. *Phys. Rev. C* **2014**, *90*, 024316. [[CrossRef](#)]
199. Pritychenko, B.; Birch, M.; Singh, B.; Horoi, M. Tables of E2 transition probabilities from the first 2⁺ states in even–even nuclei. *At. Data Nucl. Data Tables* **2016**, *107*, 1–139. [[CrossRef](#)]
200. Walker, P.; Dracoulis, G. Energy traps in atomic nuclei. *Nature* **1999**, *399*, 35–40. [[CrossRef](#)]
201. Dracoulis, G.D. Isomers, nuclear structure and spectroscopy. *Phys. Scr.* **2013**, *T152*, 014015. [[CrossRef](#)]
202. Dracoulis, G.D.; Walker, P.M.; Kondev, F.G. Review of metastable states in heavy nuclei. *Rep. Prog. Phys.* **2016**, *79*, 076301. [[CrossRef](#)]
203. Jain, A.K.; Maheshwari, B.; Goel, A. *Nuclear Isomers. A Primer*; Springer International Publishing: Berlin/Heidelberg, Germany, 2021. [[CrossRef](#)]

204. Frauendorf, S. Spontaneous symmetry breaking in rotating nuclei. *Rev. Mod. Phys.* **2001**, *73*, 463–514. [[CrossRef](#)]
205. Radford, D.C.; Baktash, C.; Beene, J.R.; Fuentes, B.; Galindo-Uribarri, A.; Gross, C.J.; Hausladen, P.A.; Lewis, T.A.; Mueller, P.E.; Padilla, E.; et al. Coulomb excitation of radioactive $^{132,134,136}\text{Te}$ beams and the low $B(E2)$ of ^{136}Te . *Phys. Rev. Lett.* **2002**, *88*, 222501. [[CrossRef](#)] [[PubMed](#)]
206. Stone, N.J.; Stuchbery, A.E.; Danchev, M.; Pavan, J.; Timlin, C.L.; Baktash, C.; Barton, C.; Beene, J.; Benczer-Koller, N.; Bingham, C.R.; et al. First nuclear moment measurement with radioactive beams by the recoil-in-vacuum technique: The g factor of the 2_1^+ state in ^{132}Te . *Phys. Rev. Lett.* **2005**, *94*, 192501. [[CrossRef](#)]
207. Biswas, S.; Palit, R.; Navin, A.; Rejmund, M.; Bisoi, A.; Sarkar, M.S.; Sarkar, S.; Bhattacharyya, S.; Biswas, D.C.; Caamaño, M.; et al. Structure of $^{132}\text{Te}_{80}$: The two-particle and two-hole spectrum of $^{132}\text{Sn}_{82}$. *Phys. Rev. C* **2016**, *93*, 034324. [[CrossRef](#)]
208. Hughes, R.O.; Zamfir, N.V.; Radford, D.C.; Gross, C.J.; Barton, C.J.; Baktash, C.; Caprio, M.A.; Casten, R.F.; Galindo-Uribarri, A.; Hausladen, P.A.; et al. γ -ray spectroscopy of ^{132}Te through β decay of a ^{132}Sb radioactive beam. *Phys. Rev. C* **2005**, *71*, 044311. [[CrossRef](#)]
209. Severyukhin, A.P.; Arsenyev, N.N.; Pietralla, N.; Werner, V. Impact of variational space on $M1$ transitions between first and second quadrupole excitations in $^{132,134,136}\text{Te}$. *Phys. Rev. C* **2014**, *90*, 011306. [[CrossRef](#)]
210. Danchev, M.; Rainovski, G.; Pietralla, N.; Gargano, A.; Covello, A.; Baktash, C.; Beene, J.R.; Bingham, C.R.; Galindo-Uribarri, A.; Gladniskhi, K.A.; et al. One-phonon isovector $2_{1,MS}^+$ state in the neutron-rich nucleus ^{132}Te . *Phys. Rev. C* **2011**, *84*, 061306. [[CrossRef](#)]
211. Bao, M.; Jiang, H.; Zhao, Y.M.; Arima, A. Low-lying states of even-even $N = 80$ isotones within the nucleon-pair approximation. *Phys. Rev. C* **2020**, *101*, 014316. [[CrossRef](#)]
212. Terasaki, J.; Engel, J.; Nazarewicz, W.; Stoitsov, M. Anomalous behavior of 2^+ excitations around ^{132}Sn . *Phys. Rev. C* **2002**, *66*, 054313. [[CrossRef](#)]
213. Fleischer, P.; Klüpfel, P.; Reinhard, P.G.; Maruhn, J.A. Skyrme energy functional and low lying 2^+ states in Sn, Cd, and Te isotopes. *Phys. Rev. C* **2004**, *70*, 054321. [[CrossRef](#)]
214. Sau, J.; Heyde, K.; Chéry, R. Shell-model description of the nucleus ^{132}Te . *Phys. Rev. C* **1980**, *21*, 405–418. [[CrossRef](#)]
215. Gargano, A.; Coraggio, L.; Covello, A.; Itaco, N. Realistic shell-model calculations and exotic nuclei. *J. Phys. Conf. Ser.* **2014**, *527*, 012004. [[CrossRef](#)]
216. Hicks, S.F.; Stuchbery, A.E.; Churchill, T.H.; Bandyopadhyay, D.; Champine, B.R.; Coombes, B.J.; Davoren, C.M.; Ellis, J.C.; Faulkner, W.M.; Leshner, S.R.; et al. Nuclear structure of ^{130}Te from inelastic neutron scattering and shell model analysis. *Phys. Rev. C* **2022**, in press.
217. Jakob, G.; Benczer-Koller, N.; Kumbartzki, G.; Holden, J.; Mertzimekis, T.J.; Speidel, K.H.; Ernst, R.; Stuchbery, A.E.; Pakou, A.; Maier-Komor, P.; et al. Evidence for proton excitations in $^{130,132,134,136}\text{Xe}$ isotopes from measurements of g factors of 2_1^+ and 4_1^+ states. *Phys. Rev. C* **2002**, *65*, 024316. [[CrossRef](#)]
218. Coquard, L.; Pietralla, N.; Ahn, T.; Rainovski, G.; Bettermann, L.; Carpenter, M.P.; Janssens, R.V.F.; Leske, J.; Lister, C.J.; Möller, O.; et al. Robust test of $E(5)$ symmetry in ^{128}Xe . *Phys. Rev. C* **2009**, *80*, 061304. [[CrossRef](#)]
219. Coquard, L.; Pietralla, N.; Rainovski, G.; Ahn, T.; Bettermann, L.; Carpenter, M.P.; Janssens, R.V.F.; Leske, J.; Lister, C.J.; Möller, O.; et al. Evolution of the mixed-symmetry $2_{1,ms}^+$ quadrupole-phonon excitation from spherical to γ -soft Xe nuclei. *Phys. Rev. C* **2010**, *82*, 024317. [[CrossRef](#)]
220. Rainovski, G.; Pietralla, N.; Ahn, T.; Coquard, L.; Lister, C.; Janssens, R.; Carpenter, M.; Zhu, S.; Bettermann, L.; Jolie, J.; et al. How close to the $O(6)$ symmetry is the nucleus ^{124}Xe ? *Phys. Lett. B* **2010**, *683*, 11–16. [[CrossRef](#)]
221. Coquard, L.; Rainovski, G.; Pietralla, N.; Ahn, T.; Bettermann, L.; Carpenter, M.P.; Janssens, R.V.F.; Leske, J.; Lister, C.J.; Möller, O.; et al. $O(6)$ -symmetry breaking in the γ -soft nucleus ^{126}Xe and its evolution in the light stable xenon isotopes. *Phys. Rev. C* **2011**, *83*, 044318. [[CrossRef](#)]
222. Radich, A.J.; Garrett, P.E.; Allmond, J.M.; Andreoiu, C.; Ball, G.C.; Bianco, L.; Bildstein, V.; Chagnon-Lessard, S.; Cross, D.S.; Demand, G.A.; et al. Ground-state and pairing-vibrational bands with equal quadrupole collectivity in ^{124}Xe . *Phys. Rev. C* **2015**, *91*, 044320. [[CrossRef](#)]
223. Morrison, L.; Hadyńska-Klęk, K.; Podolyák, Z.; Doherty, D.T.; Gaffney, L.P.; Kaya, L.; Próchniak, L.; Samorajczyk-Pyśk, J.; Srebrny, J.; Berry, T.; et al. Quadrupole deformation of ^{130}Xe measured in a Coulomb-excitation experiment. *Phys. Rev. C* **2020**, *102*, 054304. [[CrossRef](#)]
224. Wolf, A.; Cheifetz, E. Magnetic moment of the 6^+ isomeric state of ^{134}Te . *Phys. Rev. Lett.* **1976**, *36*, 1072–1074. [[CrossRef](#)]
225. Goodin, C.; Stone, N.J.; Ramayya, A.V.; Daniel, A.V.; Stone, J.R.; Hamilton, J.H.; Li, K.; Hwang, J.K.; Luo, Y.X.; Rasmussen, J.O.; et al. g factors, spin-parity assignments, and multipole mixing ratios of excited states in $N = 82$ isotones ^{134}Te , ^{135}I . *Phys. Rev. C* **2008**, *78*, 044331. [[CrossRef](#)]
226. Stuchbery, A.E.; Stone, N.J. Recoil in vacuum for Te ions: Calibration, models, and applications to radioactive-beam g -factor measurements. *Phys. Rev. C* **2007**, *76*, 034307. [[CrossRef](#)]
227. Benczer-Koller, N.; Kumbartzki, G.; Gürdal, G.; Gross, C.; Stuchbery, A.; Krieger, B.; Hatarik, R.; O'Malley, P.; Pain, S.; Segen, L.; et al. Measurement of g factors of excited states in radioactive beams by the transient field technique: ^{132}Te . *Phys. Lett. B* **2008**, *664*, 241–245. [[CrossRef](#)]
228. Fogelberg, B.; Stone, C.; Gill, R.; Mach, H.; Warner, D.; Aprahamian, A.; Rehfield, D. g -Factor of the 6_1^+ state in ^{132}Te . *Nucl. Phys. A* **1986**, *451*, 104–112. [[CrossRef](#)]

229. Lönnroth, T.; Vajda, S.; Kistner, O.C.; Rafailovich, M.H. The g -factors of isomeric states in $^{127,128}\text{Xe}$. *Z. für Phys. Atoms Nucl.* **1984**, *317*, 215–223. [[CrossRef](#)]
230. Moore, R.; Bruce, A.; Dendooven, P.; Billowes, J.; Campbell, P.; Ezwam, A.; Flanagan, K.; Forest, D.; Huikari, J.; Jokinen, A.; et al. Character of an 8^- isomer of ^{130}Ba . *Phys. Lett. B* **2002**, *547*, 200–204. [[CrossRef](#)]
231. Królas, W.; Grzywacz, R.; Rykaczewski, K.P.; Batchelder, J.C.; Bingham, C.R.; Gross, C.J.; Fong, D.; Hamilton, J.H.; Hartley, D.J.; Hwang, J.K.; et al. First observation of the drip line nucleus ^{140}Dy : Identification of a $7\mu\text{s}$ K isomer populating the ground state band. *Phys. Rev. C* **2002**, *65*, 031303. [[CrossRef](#)]
232. Rudolph, D.; Baktash, C.; Brinkman, M.J.; Caurier, E.; Dean, D.J.; Devlin, M.; Dobaczewski, J.; Heenen, P.H.; Jin, H.Q.; LaFosse, D.R.; et al. Rotational bands in the doubly magic nucleus ^{56}Ni . *Phys. Rev. Lett.* **1999**, *82*, 3763–3766. [[CrossRef](#)]
233. Eriksen, T.; Kibedi, T.; Reed, M.W.; deVries, M.; Stuchbery, A.E.; Akber, A.; Dowie, J.; Evitts, L.J.; Garnsworthy, A.B.; Gerathy, M.; et al. Systematic studies of $E0$ transitions in $^{54,56,58}\text{Fe}$. *Proc. Sci.* **2017**, *INPC2016*, 69. [[CrossRef](#)]
234. Dowie, J.T.H.; Kibédi, T.; Stuchbery, A.E.; Akber, A.; Aava, A.; Bignell, L.J.; Chisapi, M.V.; Coombes, B.J.; Eriksen, T.K.; Gerathy, M.S.M.; et al. Evidence for shape coexistence in ^{52}Cr through conversion-electron and pair-conversion spectroscopy. *EPJ Web Conf.* **2020**, *232*, 04004. [[CrossRef](#)]
235. Eriksen, T. Investigation of the Hoyle State in ^{12}C and the Related Triple Alpha Reaction Rate. Ph.D. Thesis, Department of Nuclear Physics, Research School of Physics and Engineering, The Australian National University, Canberra, Australia, 2018. [[CrossRef](#)]
236. Dowie, J.T.H. An Investigation into Nuclear Shape Coexistence Through high Precision Conversion Electron and Electron-Positron Pair Spectroscopy. Ph.D. Thesis, The Australian National University, Canberra, Australia, 2021. [[CrossRef](#)]
237. Nowak, K.; Wimmer, K.; Hellgartner, S.; Mücher, D.; Bildstein, V.; Diriken, J.; Elseviers, J.; Gaffney, L.P.; Gernhäuser, R.; Iwanicki, J.; et al. Spectroscopy of ^{46}Ar by the (t, p) two-neutron transfer reaction. *Phys. Rev. C* **2016**, *93*, 044335. [[CrossRef](#)]
238. Hinds, S.; Middleton, R. A study of the (t, p) reactions leading to ^{48}Ti and ^{50}Ti . *Nucl. Phys. A* **1967**, *92*, 422–432. [[CrossRef](#)]
239. Casten, R.F.; Flynn, E.R.; Hansen, O.; Mulligan, T.J. Strong $L = 0$ (t, p) Transitions in the even isotopes of Ti, Cr, and Fe. *Phys. Rev. C* **1971**, *4*, 130–137. [[CrossRef](#)]
240. Suehiro, T.; Kokame, J.; Ishizaki, Y.; Ogata, H.; Sugiyama, Y.; Saji, Y.; Nonaka, I.; Itonaga, K. Core-excited states of ^{54}Fe from the $^{56}\text{Fe}(p, t)^{54}\text{Fe}$ reaction at 52 MeV. *Nucl. Phys. A* **1974**, *220*, 461–476. [[CrossRef](#)]
241. Nann, H.; Benenson, W. Levels of ^{56}Ni . *Phys. Rev. C* **1974**, *10*, 1880–1888. [[CrossRef](#)]
242. Dombrádi, Z.; Sohler, D.; Sorlin, O.; Azaiez, F.; Nowacki, F.; Stanoiu, M.; Penionzhkevich, Y.E.; Timár, J.; Amorini, F.; Baiborodin, D.; et al. Search for particle-hole excitations across the $N = 28$ shell gap in $^{45,46}\text{Ar}$ nuclei. *Nucl. Phys. A* **2003**, *727*, 195–206. [[CrossRef](#)]
243. Parker, J.J.; Wiedenhöver, I.; Cottle, P.D.; Baker, J.; McPherson, D.; Riley, M.A.; Santiago-Gonzalez, D.; Volya, A.; Bader, V.M.; Baugher, T.; et al. Isomeric character of the lowest observed 4^+ state in ^{44}S . *Phys. Rev. Lett.* **2017**, *118*, 052501. [[CrossRef](#)]
244. Coenen, E.; Deneffe, K.; Huyse, M.; Duppen, P.V.; Wood, J.L. α decay of neutron-deficient odd Bi nuclei: Shell-model intruder states in Tl and Bi isotopes. *Phys. Rev. Lett.* **1985**, *54*, 1783–1786. [[CrossRef](#)]
245. Ajzenberg-Selove, F. Energy levels of light nuclei $A = 11$ –12. *Nucl. Phys. A* **1990**, *506*, 1–158. [[CrossRef](#)]
246. Endt, P. Supplement to energy levels of $A = 21$ –44 nuclei (VII). *Nucl. Phys. A* **1998**, *633*, 1–220. [[CrossRef](#)]
247. Grévy, S.; Negoita, F.; Stefan, I.; Achouri, N.L.; Angélique, J.C.; Bastin, B.; Borcea, R.; Buta, A.; Daugas, J.M.; De Oliveira, F.; et al. Observation of the 0_2^+ state in ^{44}S . *Eur. Phys. J. A* **2005**, *25*, 111–113. [[CrossRef](#)]
248. Shimoura, S.; Ota, S.; Demichi, K.; Aoi, N.; Baba, H.; Elekes, Z.; Fukuchi, T.; Gomi, T.; Hasegawa, K.; Ideguchi, E.; et al. Lifetime of the isomeric 0_2^+ state in ^{12}Be . *Phys. Lett. B* **2007**, *654*, 87–91. [[CrossRef](#)]
249. Gaudefroy, L.; Daugas, J.M.; Hass, M.; Grévy, S.; Stodel, C.; Thomas, J.C.; Perrot, L.; Girod, M.; Rossé, B.; Angélique, J.C.; et al. Shell Erosion and Shape Coexistence in $^{43}\text{S}_{27}$. *Phys. Rev. Lett.* **2009**, *102*, 092501. [[CrossRef](#)]
250. Heyde, K.; Wood, J.L. *Quantum Mechanics for Nuclear Structure*; IOP Publishing: Bristol, UK, 2019; Volume 1, pp. 2053–2563. [[CrossRef](#)]
251. McCoy, A.E.; Caprio, M.A. Algebraic evaluation of matrix elements in the Laguerre function basis. *J. Math. Phys.* **2016**, *57*, 021708. [[CrossRef](#)]
252. Rowe, D.J.; McCoy, A.E.; Caprio, M.A. The many-nucleon theory of nuclear collective structure and its macroscopic limits: An algebraic perspective. *Phys. Scr.* **2016**, *91*, 033003. [[CrossRef](#)]
253. Jarrio, M.; Wood, J.; Rowe, D. The $\text{SU}(3)$ structure of rotational states in heavy deformed nuclei. *Nucl. Phys. A* **1991**, *528*, 409–435. [[CrossRef](#)]
254. Bahri, C.; Rowe, D. $\text{SU}(3)$ quasi-dynamical symmetry as an organizational mechanism for generating nuclear rotational motions. *Nucl. Phys. A* **2000**, *662*, 125–147. [[CrossRef](#)]
255. Inonu, E.; Wigner, E.P. On the contraction of groups and their representations. *Proc. Natl. Acad. Sci. USA* **1953**, *39*, 510–524. [[CrossRef](#)]
256. Cooke, T.H.; Wood, J.L. An algebraic method for solving central force problems. *Am. J. Phys.* **2002**, *70*, 945–950. [[CrossRef](#)]
257. Dytrych, T.; Launey, K.D.; Draayer, J.P.; Rowe, D.J.; Wood, J.L.; Rosensteel, G.; Bahri, C.; Langr, D.; Baker, R.B. Physics of nuclei: Key role of an emergent symmetry. *Phys. Rev. Lett.* **2020**, *124*, 042501. [[CrossRef](#)] [[PubMed](#)]
258. McCoy, A.E.; Caprio, M.A.; Dytrych, T.C.V.; Fasano, P.J. Emergent $\text{Sp}(3, \mathbb{R})$ dynamical symmetry in the nuclear many-body system from an ab initio description. *Phys. Rev. Lett.* **2020**, *125*, 102505. [[CrossRef](#)] [[PubMed](#)]
259. Sargsyan, G.H.; Launey, K.D.; Baker, R.B.; Dytrych, T.; Draayer, J.P. $\text{SU}(3)$ -guided realistic nucleon–nucleon interactions for large-scale calculations. *Phys. Rev. C* **2021**, *103*, 044305. [[CrossRef](#)]

-
260. Kramer, G.; Blok, H.; Van Den Brand, J.; Bulten, H.; Ent, R.; Jans, E.; Lanen, J.; Lapikás, L.; Nann, H.; Quint, E.; et al. Proton ground-state correlations in ^{40}Ca studied with the reaction $^{40}\text{Ca}(e, e'p)^{39}\text{K}$. *Phys. Lett. B* **1989**, *227*, 199–203. [[CrossRef](#)]
261. Crespo, R.; Arriaga, A.; Wiringa, R.; Cravo, E.; Mecca, A.; Deltuva, A. Many-body effects in (p,pN) reactions within a unified approach. *Phys. Lett. B* **2020**, *803*, 135355. [[CrossRef](#)]